Imperial College London

Department of Mechanical Engineering

One-Dimensional Modelling

Of Hydrate Formation in Pipelines

Mohamad Azlin Bin Ali

2014

Supervised by Dr Raad Issa

Submitted in part fulfilment of the requirements for the degree of Doctor

of Philosophy in Mechanical Engineering of Imperial College

London

and the Diploma of Imperial College London

The copyright of this thesis rests with the author and is made available under a Creative Commons Attribution Non-Commercial No Derivatives licence. Researchers are free to copy, distribute or transmit the thesis on the condition that they attribute it, that they do not use it for commercial purposes and that they do not alter, transform or build upon it. For any reuse or redistribution, researchers must make clear to others the licence terms of this work.

I declare that the work contained within this thesis is my own and that it has not been submitted anywhere for any award. I certify that all material in this dissertation, which is not my own work, has been properly acknowledged.

Tuesday, 9th December 2014

Mohamad Azlin Bin Ali

Abstract

Hydrate formation in oil and gas pipelines can be troublesome and often, without a proper remediation, the formation of hydrates can lead to a pipe blockage. As hydrate formation is a non-isothermal process, the modelling of the thermodynamic behaviour of the phases within the flow is proposed. A single energy equation has been formulated and verified with parametric analyses. A new hydrate kinetics routine, based on a two-step hydrate formation mechanism, in an oil-dominated flow is proposed. The first step involves the mass transfer of gas from the free gas phase into the oil (gas dissolution rate) and the second step is the mass transfer of the dissolved gas into the water (gas consumption rate). Suitable models in the form of transport equations for each mechanism, together with appropriate closure relations to account for the agglomeration of hydrate particles and hydrate slurry viscosity, are formulated. Both the energy equation and the hydrate kinetics routine were integrated into an existing in-house research code, TRIOMPH (Transient Implicit One-Dimensional Multiphase). The model was tested and validated against two flow loop experiments, and has shown good agreement. Advancement over the only other existing model in predicting hydrate formation in the heavily slugged hypothetical pipe, has also been shown, giving the current model versatility in simulating both slug and non-slug cases.

Acknowledgements

I would like to express my deepest gratitude to my supervisor Dr. Raad Issa for his remarkable supervision, endless support and invaluable insights towards the realisation of this PhD project. I'm indebted to Prof. Dendy Sloan for providing the theses with experimental data. Special recognition to my lab mates, Mohammad, Fabio, Francesco, Fabian and George, that have assisted me along the way, and making my 4 years here memorable and enjoyable!

I thank the Malaysian Ministry of Higher Education and the University of Malaya for funding my PhD.

My heartfelt thanks go to all my friends, especially Amira, Segolene, Bart, Rodrigo, Marina, Mariana and Hakim for their friendship and laughter throughout this demanding journey and to Jan and Lola for keeping me sane. Lastly, I thank my family especially my parents; both of whom for their devoted support, made this thesis possible.

Table of Contents

Abstract **3**

Acknowledgements **4**

Table of Contents **5**

List of Tables **9**

List of Figures **10**

Nomenclature **14**

1 INTRODUCTION **18**

1.1 Multiphase Flow **18**

1.2 Hydrates **21**

1.2.1 Hydrates in flow assurance 24

1.3 Motivation for Work **25**

1.4 Present Contribution **27**

1.5 Outline of Thesis **29**

2 BACKGROUND **31**

2.1 Preamble **31**

2.2 Two-fluid Model **32**

2.2.1 TRIOMPH (Transient Implicit One-Dimensional Multiphase) 33

2.2.1.1 Two-phase model equations 34

2.2.1.2 Two-phase closure equations 37

2.2.2 Three-phase flow 38

2.2.2.1 Three-phase model equations 39

2.2.2.1.1 Emulsion viscosity *45*

2.2.2.2 Three-phase closure equations 45

2.2.2.2.1 Friction factors *45*

2.2.2.2.2 Gas Entrainment *47*

2.2.2.2.3 Flow pattern transition *48*

2.2.2.2.4 Phase inversion *50*

2.3 Review of Gas Hydrate Formation **51**

2.3.1 Driving forces for hydrate nucleation 51

2.3.2 Hydrate growth rate experiments and modelling 52

2.3.3 Agglomeration and hydrate slurry viscosity 59

3 MODEL FORMULATION **63**

3.1 Preamble **63**

3.2 Transport Equations **64**

3.2.1 Continuity equations 65

3.2.2 Momentum equations 70

3.2.3 Energy equation 72

3.2.3.1 The derivation of energy equation 72

3.3 Gas Dissolution Rate 75

3.4 Hydrate Formation Rate 76

3.5 Agglomeration of Hydrate Globules 78

3.6 Numerical Implementation 80

3.6.1 Boundary conditions 83

3.6.1.1 Flow-loop boundary condition 84

3.6.2 Integration of the hydrate kinetics routine into TRIOMPH 84

4 MODEL VALIDATION 87

4.1 Preamble 87

4.2 Parametric Analyses for the Energy Equation 88

4.3 Parametric Analyses for the Hydrate Kinetics Routine 93

4.4 Validation Against Experimental Data 96

4.4.1 ExxonMobil Flow loop 96

4.4.1.1 ExxonMobil flow loop experimental setup. 96

4.4.1.2 ExxonMobil flow loop modelling setup 99

4.4.1.3 Results and discussion 103

4.4.2 University of Tulsa Flow loop 109

4.4.2.1 Description of the University of Tulsa flow loop 109

4.4.2.2 University of Tulsa flow loop simulation setup 111

4.4.2.3 Results and discussion 112

4.5 Hypothetical Pipe 118

5 CONCLUSIONS AND RECOMMENDATIONS 124

5.1 Conclusions 124

5.2 Recommendations for Future Works 127

5.2.1 Surface area for hydrate formation 127

5.2.2 Hydrate transport model 129

References 130

Appendix A: The Derivation of the Liquid Mixture Momentum Equation 138

Appendix B: The Derivation of Non-Conservative Energy Equation 140

Appendix C: Oils Composition 142

List of Tables

Table 4.1: Input parameters used in the Energy equation analyses..... 89

Table 4.2: The analytical versus numerical solutions for test 5..... 93

Table 4.3: Input parameters for hydrate kinetics rountine analyses..... 94

Table 4.4: ExxonMobil flow loop experiments used for comparison with the current model..... 99

Table 4.5: University of Tulsa flow loop experiments used for comparison with the current model..... 111

Table 4.6: Input parameters for the test case..... 119

List of Figures

Figure 1.1: Flow patterns in horizontal flow (Baker, 1954) 20

Figure 1.2: Slug unit characteristics (Barbeau, 2008) 21

Figure 1.3: A typical structure of a gas hydrate where water molecules form a cage and encapsulate a gas molecule (Maslin et al., 2010) 22

Figure 1.4: The different types of hydrate structures (Sloan, 2003) 23

Figure 1.5: A typical methane hydrate formation curve 23

Figure 1.6: A simplified conceptual picture of the formation of hydrate blockages in a pipeline (reproduced and modified from Turner (2006)) 25

Figure 1.7: A large gas hydrate plug formed in a subsea hydrocarbon pipeline. Picture courtesy from Petrobras® (Brazil) 26

Figure 2.1: Pipe cross section (two-phase) 35

Figure 2.2: Geometrical parameters in gas/liquid/liquid stratified flow (Barbeau, 2008). 41

Figure 2.3: The influence of phase inversion on the pressure gradient (Pan, 1996) 50

Figure 3.1: Model variables and their relations 71

Figure 3.2: Mass transfer coefficient, kDG from Turner's autoclave experiment (Turner, 2006) 76

Figure 3.3: Subcooling temperature (Boxall, 2009). 78

Figure 3.4: Staggered grid arrangement (Issa and Abrishami, 1986) 81

Figure 3.5: Periodic boundary condition to imitate the displacement pump in flow loops. 84

Figure 3.6: Integration of the hydrate kinetics routine into TRIOMPH. 85

Figure 3.7: Flow chart of the solution algorithm in TRIOMPH 86

Figure 4.1: The temperature profile for (a) Analysis 1 (b) Analysis 2 90

Figure 4.2: The pressure and temperature profile for Analysis 3. 91

Figure 4.3: The temperature profile for analysis 4. 92

Figure 4.4: The pressure and temperature profile for Analysis 5. 93

Figure 4.5: The dissolved gas module analysis. 95

Figure 4.6: The hydrate module analysis. 96

Figure 4.7: Schematic diagram of the ExxonMobil flow loop (Boxall, 2009) 96

Figure 4.8: Nucleation point of hydrate formation. 101

Figure 4.9: Example of temperature prediction to match the experimental nucleation period. 102

Figure 4.10: Mesh sensitivity analysis on Run 1(a) of the ExxonMobil experiments ($94m$ long, $9.72cm$ in diameter), coarse mesh (Δxcoarse)=$1.0m$, fine mesh (Δxfine)=$0.0392m$. 102

Figure 4.11: The effect of fitted rate constant, u' on hydrate formation 103

Figure 4.12: The experiment where hydrate formation is well predicted. u' =0.0000216, Pump speed: 300RPM, pressure: 5.068MPa, oil viscosity: 0.0005 $Pa.s$..... 104

Figure 4.13: Experiments where hydrate formation are over predicted. (a) u'=0.0000171, Pump speed: 300RPM, pressure: 6.55MPa, oil viscosity: 0.0005 $Pa.s$ (b) u' =0.0000387, Pump speed: 550RPM, pressure: 6.55MPa, oil viscosity: 0.0005 $Pa.s$..... 105

Figure 4.14: Experiments where hydrate formation are over predicted (a) u'=0.0000091, Pump speed: 300RPM, pressure: 5.068MPa, oil viscosity: 0.1 $Pa.s$ (b) u' =0.0000236, Pump speed: 550RPM, pressure: 5.068MPa, oil viscosity: 0.1 $Pa.s$ 106

Figure 4.15: Schemetic diagram of the University of Tulsa flow loop [Dellecase et al. (2008) as cited by Boxall (2009)]. 109

Figure 4.16: Plot of gas addition. Caratinga oil, pump speed=750RPM, liquid loading=0.5, water cut=0.25. 113

Figure 4.17: Plot of gas addition. Buttermilk oil, pump speed=750RPM, liquid loading=0.5, water cut=0.25. 113

Figure 4.18: Plot of gas addition. Citgo19 oil, pump speed=750RPM, liquid loading=0.5, water cut=0.25. 114

Figure 4.19: Plot of gas addition. Citgo19 oil, pump speed=750RPM, liquid loading=0.5, water cut=0.125..... 114

Figure 4.20: Plot of gas addition. Citgo19 oil, pump speed=1250RPM, liquid loading=0.5, water cut=0.125. 115

Figure 4.21: Plot of gas addition. Citgo19 oil, pump speed=750RPM, liquid loading=0.8, water cut=0.25. 115

Figure 4.22: The plot of various phase fractions for one of the University of Tulsa flow loop experiments. 116

Figure 4.23: A result from an autoclave experiments performed by Turner (2006)..... 118

Figure 4.24: Slug profile generated by the current model for the test case. 120

Figure 4.25: The temperature profile and the water conversion of the hypothetical pipe. 121

Figure 4.26: Hydrate formation in slug flow regime between the current model and the method used in CSMHyK (a) water conversion over the pipe length (b) hydrate cut over the pipe length. 122

Figure 5.1: Phase diagram of different flow regimes shown as two intersecting lines that represent the planes of the inertial and viscous sub-ranges Boxall (2009)..... 128

Figure 5.2: Universal curve to estimate the mean droplet size in water-in-oil dispersions system (Boxall, 2009) 128

Nomenclature

Roman symbols

Symbol	Description
A	Cross-sectional area
A_s	Surface area
A_P	Particle surface area
C', $C_{j,k}$	Coefficients in Section 2.3.2
C_{bulk}	Gas concentration in the liquid bulk
C_{eq}	Gas concentration in the water phase in the presence of hydrate
C_p	Specific heat capacity
c	Volume phase concentration
D	Pipe diameter
D_{G-H}	Gas Diffusivity across hydrate shell
D_L, D_G, D_k	Hydraulic diameter
d	Droplet diameter
E_o	Eötvös number
E_a	Activation energy in Equation (2.72)
F	Frictional force
F_a	Normalized inter-particle adhesion force
f	Friction factor
f'	Fugacity
fr	Fractal dimension that accounts for the porosity of the aggregate
f_{DG}	Volume fraction of dissolved gas within oil
f_{DO}	Volume fraction of dead oil within oil
f_H	Volume fraction of hydrate within water (water conversion)
f_{PW}	Volume fraction of unconverted water within water
g	Acceleration due to gravity
h	Phase depth
h_∞	External convective heat transfer coefficient
h_k	Internal heat transfer coefficient for phase k
K^*	Combined rate parameter in Equation (2.73)
k_B, k_1, k_2	Intrinsic reaction rate constants
k_c	Newton law of cooling constant
k_r	Reaction rate constant

k_d	Mass transfer coefficient around particles
k_{DG}	Mass transfer coefficient for gas dissolution
k_{hyd}	Mass transfer coefficient for hydrate formation
l_U	Slug unit (Figure 1.2)
l_{lf}	Liquid film region in Figure 1.2
l_s	Slug body region in Figure 1.2
$\dot{M}_B$, $\dot{m}_{B,O}$, $\dot{m}_{B,W}$, $\dot{m}_{B,c}$	The rate of gas entrainment
$\dot{m}_{DG}$	Gas dissolution rate
Nu	Nusselt number
n	Mole number
P	Pressure
Pr	Prandtl number
$\mathcal{P}(r,t)$	Particles distribution in Equation (2.75)
Q	Heat transfer term in the energy equation
r	Droplet radius
r_w	Water core radius
r_p	Hydrate particle radius
R	Gas constant
Re	Reynolds number
S	Wetted perimeter
T	Temperature
t	Time
U	Superficial velocity
U_k	U-value in the energy equation for phase k
u	Velocity
u'	Fitted rate constant
W	Molecular weight
We	Weber number
X	Mole fraction of gas
x	Distance
χ_{pipe}	Pipe thickness
z	Gas compressibility factor
Z	Vertical pipe height

Greek symbol

Symbol	**Description**
α	Phase fraction
β	Pipe inclination

γ	Stratification angle
$\dot{\gamma}$	Shear rate
δ	Hydrate shell thickness
ε_1, ε_2, ε_3, ε_4	Empirical constants in Equation (2.72)
θ_{G-H}	Moles of gas per mole of hydrate
λ_W^{inv}	Inlet water fraction at phase inversion
λ_W	Inlet water fraction
λ_{pipe}	Thermal conductivity
μ	Dynamic viscosity
μ_r	Relative viscosity
ρ	Density
σ	Surface tension
τ	Shear stress
$\emptyset$	Volume fraction in equation (2.85)
Ψ, Ω	Parameters in liquid mixture momentum Equation

Subscript

Symbol	**Description**
A	
B	Gas bubbles phase
c	Continuous phase (for liquid-liquid dispersion)
$crit$	Critical
DG	Dissolved gas phase
DO	Dead oil phase
d	Dispersed phase (for liquid-liquid dispersion)
eff	Effective
eq	Equilibrium
H	Hydrate phase
i	Gas-liquid interphase
$inlet$	Inlet plane
j	Oil-water interphase
k	Generic phase
L	Liquid phase
lf	Liquid film
M	Liquid mixture phase
max	Maximum
O	Oil phase
$outlet$	Outlet plane

PW	Unconverted water phase
s	Surface
sub	Subcooling (Driving force)
sys	System
W	Water
w	Wall
∞	Enviroment

Superscript

Symbol	**Description**
eq	Equilibrium
inv	Phase inversion
ref	Reference

1 INTRODUCTION

Flow assurance is one of the most important aspects in the petroleum industry and serves the purpose of assuring crude oil and natural gas are transported economically from the reservoir to the processing facilities. It is common practice to transport the fluids from the reservoir to onshore or offshore facilities via pipelines and often, most of the fluids within those pipelines are multiphase. In addition, hydrates (an ice-like structure where a gas molecule is encapsulated by water molecules) frequently form in pipelines and plug up the pipe, disrupting production and leading to costly repair operations.

1.1 Multiphase Flow

Multiphase flow (the mixture of gasses, liquids and solids) is prevalent in many of the production pipelines in the oil and gas industry. The nature of the flow is very complex due to the existence of different flow regimes and the presence of several phases, often oil, water, gas and sand.

The most basic form in multiphase flow is a two-phase system where a variety of flow patterns can be observed depending on the fluid properties and the

configuration of the pipe. In a horizontal pipe, the flow patterns can be classified into three main categories (Figure 1.1):

1. Separated flow: where the two fluids travel independently at different velocities. Stratified flow is a regime where the lighter phase flows on top while the heavier phase flows at the bottom of the pipe. There are two types of stratified flow, namely stratified smooth and stratified wavy. The difference between the two is due to the gas (lighter phase) velocity. When the gas velocity is high, there will be ripples or large waves at the liquid/gas interface (stratified wavy) while on the other hand, when the gas velocity is low, the interface remains plane, or slightly curved (stratified smooth). Annular flow is another type of separated flow, which occurs when the gas travels at high velocity along with the entrained liquid droplets at the centre of the pipe, with the liquid forming a film layer that coats the pipe wall, generally thicker at the bottom due to the gravitational force.

2. Dispersed flow: where the phases are interspersed with each other in the form of bubbles or droplets dispersed in the second phase. The two fluids usually travel at roughly the same speeds owing to the viscous stress between the two phases. Bubbly flow occurs when gas bubbles flow within a continuous liquid phase at moderate speed. Spray flow occurs at higher gas velocities where fine liquid droplets flow within the continuous gas jet.

3. Intermittent flow: divided into two main regimes, plug flow and slug flow. Slug flow occurs when gas travels faster than the liquid phase and the interface becomes wavier, with some of these waves growing more rapidly to bridge the pipe. Liquid slugs are formed, with large gas bubbles separating them. On the other hand, plug flow occurs when a succession of elongated gas bubbles travel in the upper part of the pipe (above a continuous liquid) at a similar speed to the liquid.

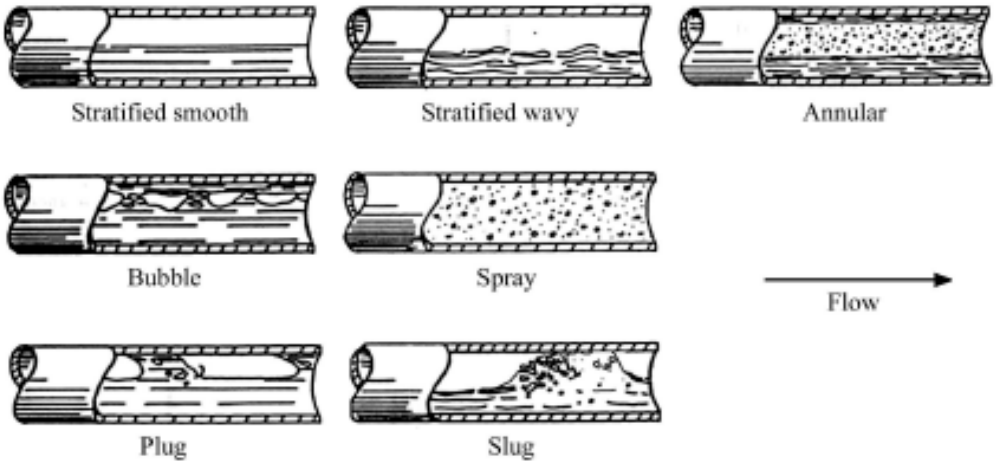


Figure 1.1: Flow patterns in horizontal flow (Baker, 1954)

Among the multiphase flow regimes described above, slug flow is the most frequently encountered flow regime in the oil and gas flowline. It is common practice, in studying the slug flow, to define the slug unit, l_U which comprises of the stratified liquid/gas region (or the liquid film region), l_f and the slug body region, l_s (Figure 1.2):

$$l_U = l_f + l_s \tag{1.1}$$

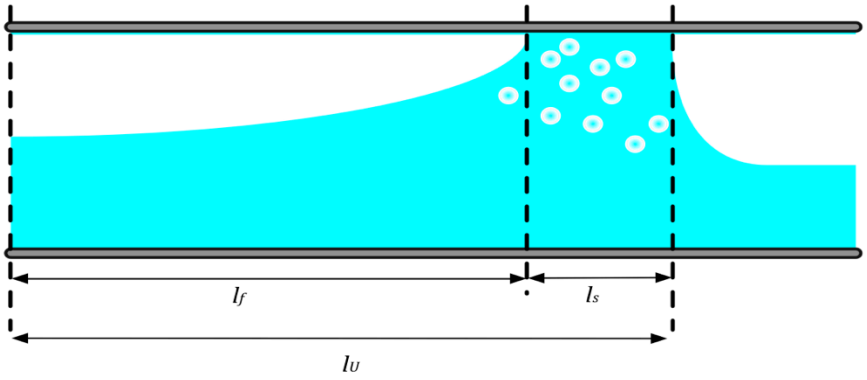


Figure 1.2: Slug unit characteristics (Barbeau, 2008)

1.2 Hydrates

Gas hydrates are clathrate compounds in which water molecules form a cage that encapsulates the gas molecule, also known as guest molecule or hydrate former, under hydrate forming conditions (Figure 1.3). The arrangement of the water molecules determines the structure of the hydrates (Carroll, 2008). There are three types of hydrate structures (Figure 1.4): structure I (sI), structure II (sII) and structure H (sH). The most common hydrate structure to form in nature is structure I while structure II frequently forms from oil and gas production. Structure H crystals are laboratory hydrates and seldom found in nature or oil and gas production.

Each of the hydrate structures has a different cage size, which means each structure encapsulates different types of gas molecules. For example, hydrate structure I generally encloses gas molecules that are small in diameter (4 to 5.5Å) such as methane (CH_4), ethane (C_2H_6) and carbon dioxide (CO_2) while structure

II hydrates can enclose gas molecules which are slightly bigger in diameter (6 to 6.9Å) such as propane (C_3H_8) and iso-butane (iso-C_4H_{10}). For a more detailed description of hydrate structures, refer to Carroll (2008) and Sloan and Koh (2007)

With the right combination of temperature and pressure, hydrates are easily formed; given a hydrate former is present, with a sufficient amount of water. Hydrate formation curves are normally used to determine the conditions at which the hydrate will form or dissociate. These curves vary for different types of hydrate and are usually generated through a series of experiments or known correlations. However, it is common practice for many engineers or researchers to use commercial or opensource software such as Multiflash®, PVTSim®, CSMGem and DWSIM. Figure 1.5 gives an example of a typical methane hydrate (sI) formation curve.

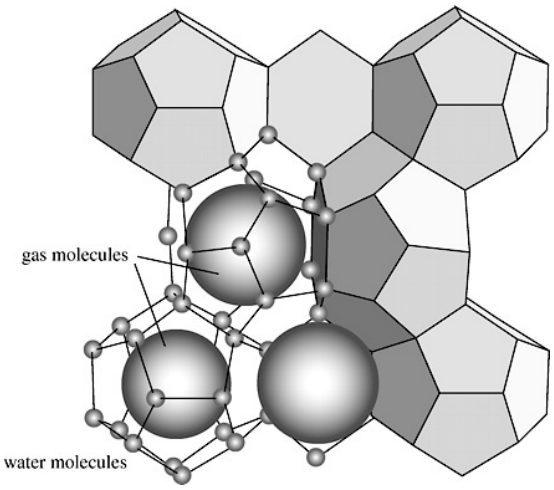


Figure 1.3: A typical structure of a gas hydrate where water molecules form a cage and encapsulate a gas molecule (Maslin et al., 2010)

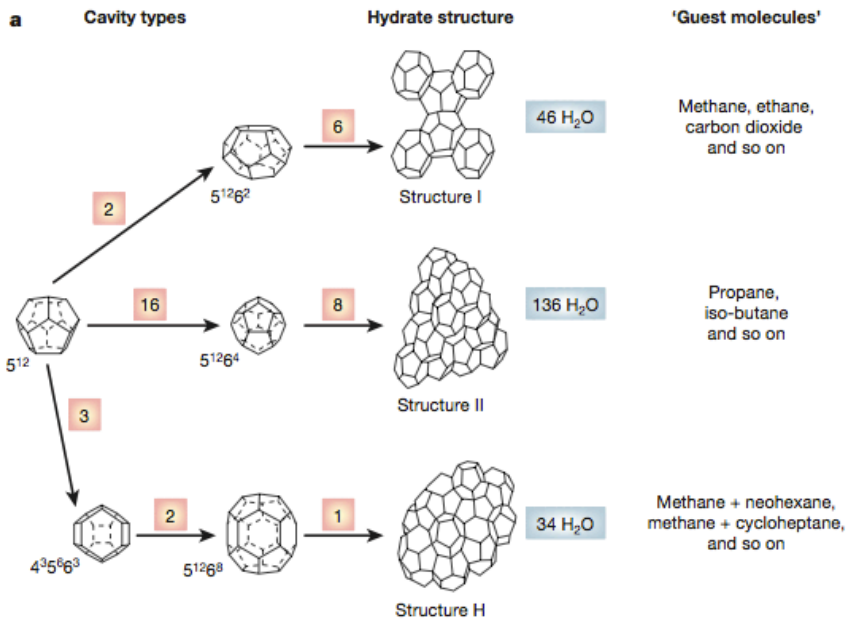


Figure 1.4: The different types of hydrate structures (Sloan, 2003)

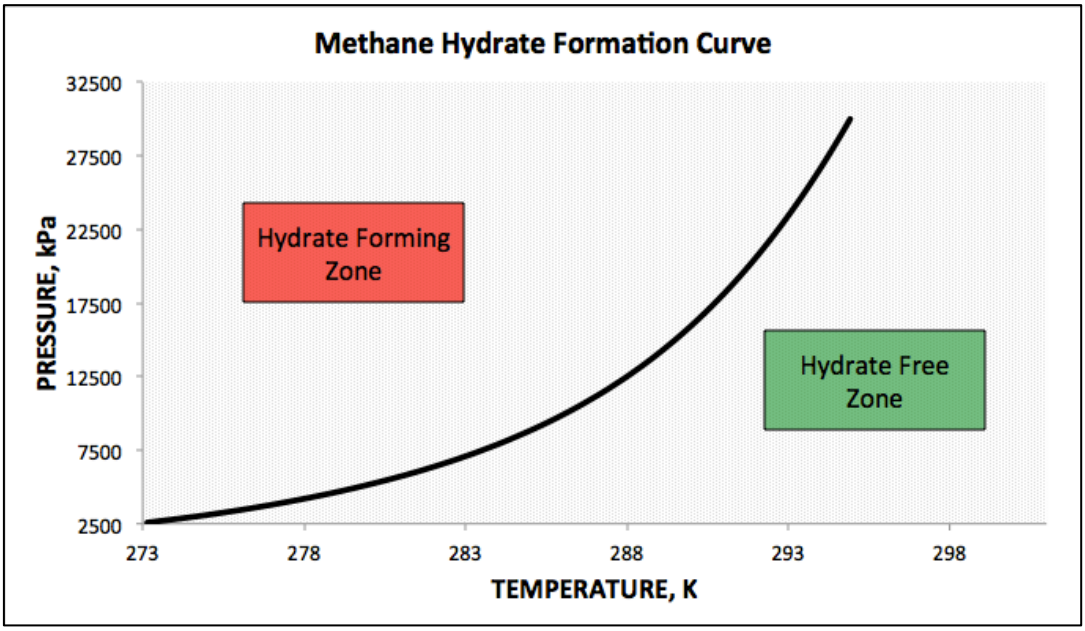


Figure 1.5: A typical methane hydrate formation curve

1.2.1 Hydrates in flow assurance

Hydrates that form in nature, such as methane gas hydrates, are an abundant source of energy and have the potential to be the future source of energy (Lee and Holder, 2001). However, in conventional oil and gas operations, hydrates are undesirable. Hydrate globules often agglomerate with each other forming bigger aggregates, and without a proper remediation technique, may eventually plug up the pipelines. As can be seen from Figure 1.5, hydrates can form at relatively high temperature, well above the freezing point of water, for a system that operates with extremely high pressure. Many pipelines for deep-sea explorations are operating well within the hydrate formation region, which puts them at risk of pipeline blockages, leading to a potential loses of revenue. Therefore an understanding of the mechanism of hydrate formation in pipelines is of the utmost importance to the flow assurance community. In general, the mechanism of hydrate blockage formation in oil-dominated pipelines is divided into four main stages as can be seen from the Figure 1.6 below. The first stage is gas dissolution and water entrainment into the oil phase. The second stage is the hydrate formation. When the right combination of pressure and temperature are met, hydrate nucleation at the water droplet surface occurs and a thin hydrate shell develops over it and thickens over time. The third stage is agglomeration, where the hydrate-encrusted water droplets agglomerate with each other through capillary forces of attraction and form a bigger piece of hydrate mass which then leads to the final stage, plugging. Plugging occurs when the agglomeration of

hydrate globules causes an increase in the slurry viscosity, producing a large pressure drop, which ultimately forms a plug in the pipeline.

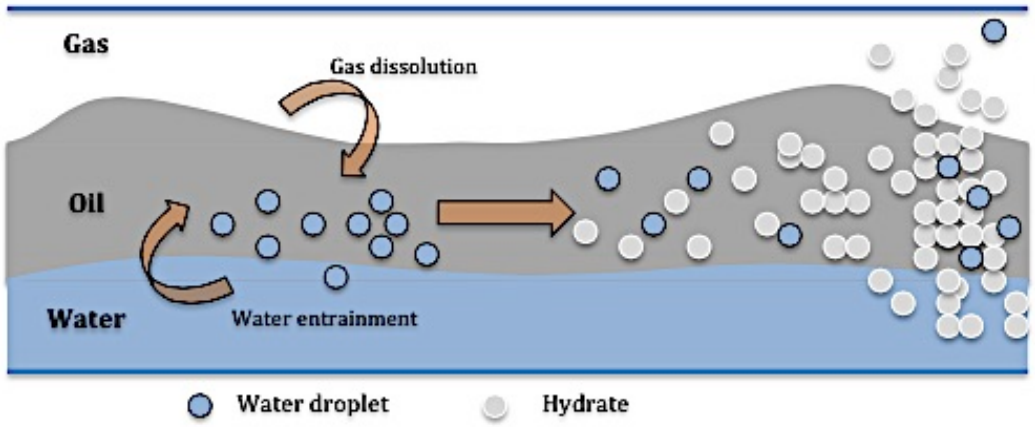


Figure 1.6: A simplified conceptual picture of the formation of hydrate blockages in a pipeline (reproduced and modified from Turner (2006))

1.3 Motivation for Work

Hydrate blockage is one of the major problems in the oil and gas industry as this will lead to costly repair operations and plug remediation. Although the hydrate thermodynamics has been studied for decades (Dharmawardhana et al., 1980; Holder and Hand, 1982; Holder and John, 1983), the study of the transient nature of hydrate formation in pipelines is fairly new and has only recently been investigated (Turner et al., 2005; Davies et al., 2008; Wang et al., 2010). In the past, the flow assurance community opted for methods that avoid hydrate formation such as the insulation of pipelines or thermodynamic inhibitors. As the exploration and subsequent production is becoming more challenging, these prevention techniques become too costly and unappealing. A better understanding

of the kinetics of hydrate formation in pipelines is therefore vital to the flow assurance community in order to prevent plugged up pipelines (Figure 1.7), hence the study of the time evolution of hydrate formation.

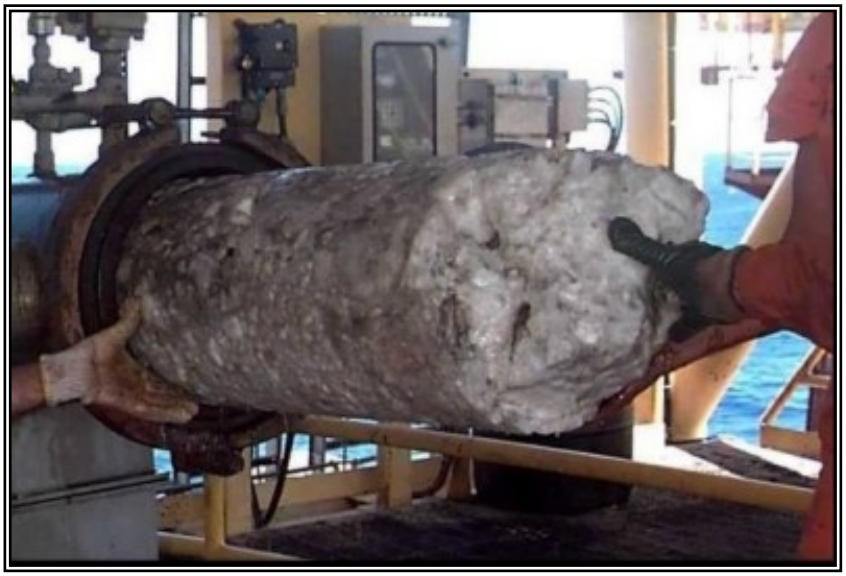


Figure 1.7: A large gas hydrate plug formed in a subsea hydrocarbon pipeline. Picture courtesy from Petrobras® (Brazil)

Pipeline simulations are now a common tool in the oil and gas industries, therefore a tool that predicts where and when hydrate blockages might occur is an added improvement. The most well known model is the CSMHyK (the Colorado School of Mines Hydrate Kinetics) model, a plug-in module incorporated into a transient multiphase simulator, OLGA®, developed by the team in the Centre for Hydrate Research at the Colorado School of Mines. They have conducted numerous researches concerning the kinetics of hydrate plug formation and their model has been successfully applied for subsea tiebacks (Davies et al., 2009b;

Zerpa et al., 2011). However, to the knowledge of the author, CSMHyK is unable to predict hydrate formation in the slug body region (Figure 1.2).

The aim of this research is to extend the modelling capability of the code named TRIOMPH (Transient Implicit One-Dimensional Multiphase), developed by Issa and Abrishami (1986), to the simulation of hydrate formation in pipelines as well as to predict hydrate formation in the slug body region. To tackle this issue, a suitable mathematical model for hydrate formation is formulated and incorporated into the existing TRIOMPH code. The new model is validated against the experimental data from Colorado School of Mines and against CSMHyK. A hypothetical case of hydrate formation in a slug flow regime is investigated.

1.4 Present Contribution

This thesis describes the progress accomplished in one-dimensional modelling of hydrate formation in horizontal pipelines. The starting point for the work was an existing research code, TRIOMPH, which was originally developed to predict two-phase, slug flow in horizontal pipe. Since then it has been extended and gone through extensive research for a number of years. The code has been proven capable to predict slug flow for a range of cases for both horizontal (Bonizzi and Issa, 2003a) and vertical pipe (Di Salvo, 2014), as well as for three-phase flow (Bonizzi and Issa, 2003b; Barbeau, 2008).

The aforementioned model is based on an assumption of isothermal condition, in the absence of hydrates. Since hydrate formation is a non-isothermal process, the first contribution of the author was the implementation of the energy equation into the model. The current model (with energy equation incorporated) has been tested and validated with simple parametric analyses for both two-phase and three-phase flow. Both analyses agree well with the theory.

The main contribution of the thesis was the implementation of a powerful hydrate kinetics model together with appropriate closure relations for the agglomeration of hydrate globules into the existing TRIOMPH. This model comprises of two modules: the dissolved gas module and the hydrate formation module. The current model, with the incorporation of the hydrate kinetics, was tested with parametric analyses and validated with experimental data. It has been found to compare well against two flow-loop (the ExxonMobil and the University of Tulsa flow loops) experiments. The experimental data used for validation in the present thesis are from the Colorado School of Mines, courtesy of Prof. E. Dendy Sloan.

One major advance over the CSMHyK model is the current model's versatility in predicting hydrate formation in both slug and non-slug flow regime. This is due to the dissolved gas module of the model. As previously mentioned, once the combination of temperature and pressure are met, hydrates are easily formed when both a guest molecule and enough water is prevalent in the system. CSMHyK uses the free gas phase as the source for the hydrate former. Therefore, CSMHyK will fail to predict hydrate formation in the slug body region, where no

free gas is present. However, in the current model, guest molecules exist in the liquid (oil) phase in the form of dissolved gas, thus hydrate formation can be predicted in this region. This method closely represents the oil and gas flow in a field, as often, the crude oil being transported from the reservoir contains dissolved gas (plus other contaminants), and only after the processing facilities is the crude oil treated and refined. This is an important finding, particularly for flowline operating in the slug flow regime. This method has been found to predict five times as much hydrate formation in the hypothetical slug flow pipe simulation compared to the method used by CSMHyK.

1.5 Outline of Thesis

The thesis is structured as follows:

Chapter 2 presents an overview of the related literature on the modelling of hydrate formation in pipelines. The one-dimensional two-fluid model, a modelling method embedded within TRIOMPH is presented. The model equations for both the two-phase and the three-phase flow, together with their closure relations are defined. Finally, hydrate formation experiments and modelling done by other researchers are reviewed.

Chapter 3 describes the current model, with the implementation of hydrate kinetics routine. This chapter focuses on the main contributions of the thesis. Firstly, all the transport equations for the current model are presented with particular emphasis on the continuity equations and the energy equation. Next,

the chapter formulates the mathematical model behind the hydrate kinetics routine that is integrated into TRIOMPH. The two modules within the hydrate kinetics routine, the dissolved gas and the hydrate formation are formulated, along with the appropriate closure relations for the agglomeration of hydrate globules and the slurry viscosity. Finally, the chapter presents the numerical implementation within the current model with suitable boundary conditions including for flow-loop modelling.

Chapter 4 gives the results from the present thesis. Firstly, simple parametric analyses to verify the correctness of the model implementation of the energy equation and the hydrate kinetics routine are presented. Next, the chapter focuses on the experimental validation of the current model against two experiments done by the Centre of Hydrate Research, Colorado School of Mines. The model is compared against two flow-loops, the ExxonMobil flow-loop and the University of Tulsa flow-loop. Finally, the chapter illustrates the capability of the current model to simulate hydrate formation in a hypothetical pipeline operating under slug flow regime.

Chapter 5 presents the conclusion drawn from the current research work and provides future work recommendations to extend on the findings of this thesis.

2 BACKGROUND

2.1 Preamble

The present chapter describes an overview of the related literature and the background studies on hydrate formation in pipelines.

Section 2.2 describes the TRIOMPH code, a one-dimensional two-fluid model developed by Issa and Abrishami (1986). Section 2.2.1 focuses on two-phase flow modelling, where the model equations and the closure relations within the framework are defined. Section 2.2.2 focuses on the three-phase flow capability of the code, an extension to the two-fluid model, developed by Bonizzi and Issa (2003b) and Barbeau (2008). The closure relations for the three-phase flow model namely friction factors, gas entrainment, flow pattern transition and phase inversion are outlined in section 2.2.2.2.

Section 2.3 presents the available literature on gas hydrate formation. The different forms of driving forces in hydrate formation are defined in section 2.3.1. Section 2.3.2 presents the previous works on the experiments and modelling of hydrate formation rate, such as from the work of Vysniauskas and Bishnoi (1983), Englezos et al. (1987a), Turner et al. (2005) and few others. Section 2.3.3 deals with the relative viscosity of the hydrate suspension (Sinquin et al., 2004) and two

mechanisms of agglomeration of hydrates globules namely shear-limited agglomeration (Sinquin et al., 2004) and contact induced agglomeration (Palermo et al., 2005).

2.2 Two-fluid Model

The one-dimensional two-fluid model is a general approach for simulating multiphase flows in long pipelines (Ishii and Hibiki, 2006). This model is based on a system of partial differential equations that are used to mathematically describe the properties of the flow. This model treats each phase or component as a separate fluid each having its own velocity, temperature and pressure and each phase is governed by an equation of conservation of mass, momentum and energy.The one-dimensional form of the two-fluid model is obtained by integrating (area averaging) the flow properties over the cross-sectional area of the flow. By introducing closure models, formulated as empirical closure relations, the effects of mass and momentum transfer at the interface between the phases and between the phase and the wall can be included via source terms in the equations. Without these interfacial exchanges in the field equations, the phases would be essentially independent (Ishii and Hibiki, 2006).

The main reason why a one-dimensional model is widely used in the oil and gas industry, is due to its ability to yield results for long pipelines extending over several kilometres within a practical time frame that cannot be achieved by multi-dimensional approaches. This is enabled by the reasonable assumption that most of the variations in the flow occur in the axial direction.

2.2.1 TRIOMPH (Transient Implicit One-Dimensional Multiphase)

The TRIOMPH code originally developed by Issa and Abrishami (1986), was extended with the development of the "slug capturing" technique, where the slug flow regime is predicted as a mechanistic and automatic outcome of the growth of hydrodynamic instabilities in stratified flow by Issa and Kempf (2003). In this technique, the same set of governing and closure laws are used for both stratified and slug flows, and therefore eliminating the need for an empirically-based slug flow model. Slugs develop, grow, merge and collapse naturally depending on the solution of the transport equations for mass and momentum for each phase. The only empirical information required is the closure relations for the wall shear stresses for each phase and the frictional force at the liquid-wall interface.

Numerous studies in the past (Issa and Woodburn, 1998; Rippiner, 1998; Issa and Kempf, 2003) have proved that the "slug capturing" technique gives satisfactory prediction of the transition from stratified to slug flow and is in good agreement with experimental measurements. Furthermore, TRIOMPH has recently also been shown to be capable of predicting the transition from stratified to annular flow (Emamzadeh and Issa, 2013a; Emamzadeh and Issa, 2013b).

2.2.1.1 Two-phase model equations

With the assumption of no mass exchange between the phases, the governing transient one-dimensional two-fluid model equations are reduced to the following:

- The gas continuity equation:

$$\frac{\partial}{\partial t}(\alpha_G \rho_G) + \frac{\partial}{\partial x}(\alpha_G \rho_G u_G) = 0 \tag{2.1}$$

- The liquid phase continuity equation:

$$\frac{\partial}{\partial t}(\alpha_L \rho_L) + \frac{\partial}{\partial x}(\alpha_L \rho_L u_L) = 0 \tag{2.2}$$

- The gas momentum equation:

$$\frac{\partial}{\partial t}(\alpha_G \rho_G u_G) + \frac{\partial}{\partial x}(\alpha_G \rho_G u_G^2) = -\alpha_G \frac{\partial P}{\partial x} - \alpha_G \rho_G g \sin\beta - F_G - F_i \tag{2.3}$$

- The liquid phase momentum equation:

$$\frac{\partial}{\partial t}(\alpha_L \rho_L u_L) + \frac{\partial}{\partial x}(\alpha_L \rho_L u_L^2) = -\alpha_L \frac{\partial P}{\partial x} - \alpha_L \rho_L g \cos\beta \frac{\partial h}{\partial x} - \alpha_L \rho_L g \sin\beta - F_L + F_i \tag{2.4}$$

where the subscript G and L refer respectively to the gas and liquid phases, while i denotes the quantities at the interface between liquid and gas. α is the phase fraction, ρ is the density, u is the velocity and P is the interfacial pressure measured at the interface between the two phases. g represents the acceleration of the gravity, β is the angle of pipe inclination, t is the time and x is the axial

coordinate. The second term on the right hand side of the liquid momentum equation is the hydrostatic term that accounts for the pressure variation in the direction normal to the pipe axis within the liquid phase. This term however, is negligible for the gas phase at atmospheric conditions, and therefore has been dropped from the gas momentum equation. The partial derivative of the liquid height $\frac{\partial h}{\partial x}$, in the hydrostatic term may be formulated in terms of the partial derivative of the liquid phase fraction, α_L as:

$$\frac{\partial h}{\partial x} = \frac{\pi}{4} \frac{D \cos\beta}{\sin\frac{\gamma}{2}} \frac{\partial \alpha_L}{\partial x} \tag{2.5}$$

where h is the liquid height, γ is the wetted angle and D is the pipe internal diameter (Figure 2.1).

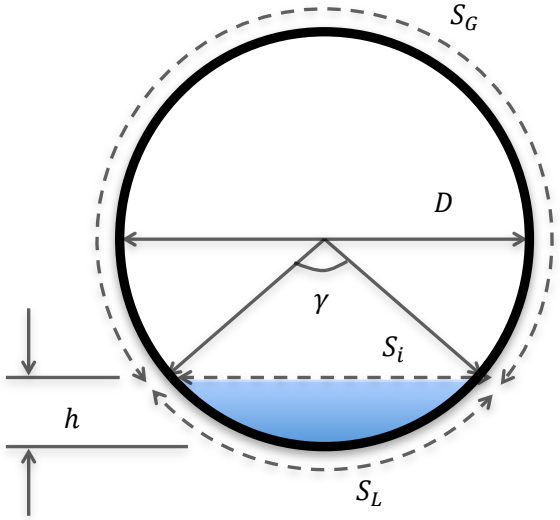


Figure 2.1: Pipe cross section (two-phase)

The term F_L represents the frictional force between the liquid phase and the wall, F_G is the frictional force between the gas phase and the wall while F_i denotes the frictional force at the liquid-gas interface. They are defined as:

$$F_L = \frac{\tau_{wL} S_L}{A} \tag{2.6}$$

$$F_G = \frac{\tau_{wG} S_G}{A} \tag{2.7}$$

$$F_i = \frac{\tau_i S_i}{A} \tag{2.8}$$

where A is the cross sectional area of the pipe, τ_{wL} and τ_{wG} are the wall shear stresses between the liquid phase and the wall and the gas phase and the wall respectively, while τ_i is the shear stress between the two phases. They are modelled by:

$$\tau_{wL} = \frac{1}{2} \rho_L f_L u_L^2 \tag{2.9}$$

$$\tau_{wG} = \frac{1}{2} \rho_G f_G u_G^2 \tag{2.10}$$

$$\tau_i = \frac{1}{2} \rho_L f_i (u_G - u_L)^2 \tag{2.11}$$

in which f_L, f_G and f_i are the friction factors, which are determined empirically as discussed in the next section. S_L, S_G and S_i are the wetted perimeters, and their values vary depending on whether the pipe is horizontal, vertical or inclined. In case of horizontal stratified flow, they are given by:

$$S_L = \frac{D}{2}\gamma \tag{2.12}$$

$$S_G = \frac{D}{2}(2\pi - \gamma) \tag{2.13}$$

$$S_i = D \sin\frac{\gamma}{2} \tag{2.14}$$

2.2.1.2 Two-phase closure equations

Closure relations are needed in one-dimensional models to evaluate the various shear stresses acting on the walls and between the phases. Many formulations can be found in the literature and most of them depend on the experimental data with specific geometries and flow rates. For this research, the closure models for the friction factors f_L, f_G and f_i are based on those recommended by Rippiner (1998) as they have been found to give consistently good agreement with the experimental data.

For the liquid-wall friction factor, that of Hand (1991) is used:

$$f_L = \begin{cases} \dfrac{24}{Re_L}, & \text{for laminar flow} \\ 0.0262(\alpha_L Re_L)^{-0.139}, & \text{for turbulent flow} \end{cases} \tag{2.15}$$

the Reynolds number for the liquid phase is defined as:

$$Re_L = \frac{D_L \rho_L u_L}{\mu_L} \tag{2.16}$$

where D_L is the liquid hydraulic diameter, defined as:

$$D_L = \frac{4A\alpha_L}{S_L} \tag{2.17}$$

The gas-wall friction factor and the interface friction factor use the same correlation, namely Taitel and Dukler (1976):

$$f = \begin{cases} 16Re^{-1}\ , & \text{for laminar flow} \\ 0.046(Re)^{-0.2}\ , & \text{for turbulent flow} \end{cases} \tag{2.18}$$

where for the gas-wall friction factor, the Reynolds number for the gas phase is defined as:

$$Re_G = \frac{D_G \rho_G u_G}{\mu_G} \tag{2.19}$$

where D_G is the gas hydraulic diameter, defined as:

$$D_G = \frac{4A\alpha_G}{S_i + S_G} \tag{2.20}$$

and the Reynolds number for the interface friction factor:

$$Re_i = \frac{D_G \rho_G (u_G - u_L)}{\mu_G} \tag{2.21}$$

2.2.2 Three-phase flow

In reality, most of the flows encountered within the oil and gas transport pipelines are more than just two-phase. Often, it is more complicated with the presence of

water and sand. Water can be present naturally in pipelines or sometimes it can be injected into reservoirs to stimulate production (Barbeau, 2008).

The modelling of transient one-dimensional three-phase slug flow with aeration has been successfully developed by Barbeau (2008). The model is capable of estimating the gas aeration rate at the slug front, as well as predicting the phase inversion phenomenon. Phase inversion is the process when the continuous phase, in a liquid-liquid dispersion, becomes the dispersed phase or vice versa. Following a method by Hibiki and Ishii (2003a) and Bonizzi and Issa (2003b), the motion of the two liquids (oil and water) can be coupled together by means of a drift flux approach. Hence, instead of three momentum equations, only two are needed for the solution and therefore this model reduces the amount of computational demand.

2.2.2.1 Three-phase model equations

For gas/oil/water stratified flow within an isothermal system, the governing conservation equations for three-phase slug flow with aeration model is as follow:

- The gas continuity equation:

$$\frac{\partial}{\partial t}(\alpha_G \rho_G) + \frac{\partial}{\partial x}(\alpha_G \rho_G u_G) = -\dot{M}_B \tag{2.22}$$

- The liquid mixture continuity equation:

$$\frac{\partial}{\partial t}(\alpha_M \rho_M) + \frac{\partial}{\partial x}(\alpha_M \rho_M u_M) = \dot{M}_B \tag{2.23}$$

- The water phase continuity equation:

$$\frac{\partial}{\partial t}(c_W \alpha_M \rho_W) + \frac{\partial}{\partial x}(c_W \alpha_M \rho_W u_W) = 0 \tag{2.24}$$

- The conservation of mass of the gas bubble entrained:

$$\frac{\partial}{\partial t}(c_B \alpha_M \rho_G) + \frac{\partial}{\partial x}(c_B \alpha_M \rho_G u_B) = \dot{M}_B \tag{2.25}$$

- The gas momentum equation:

$$\frac{\partial}{\partial t}(\alpha_G \rho_G u_G) + \frac{\partial}{\partial x}(\alpha_G \rho_G u_G^2) = -\alpha_G \frac{\partial P}{\partial x} - \alpha_G \rho_G g \sin\beta - F_G - F_i \tag{2.26}$$

- The liquid mixture momentum equation:

$$\begin{aligned} &\frac{\partial}{\partial t}(\alpha_M \rho_M u_M) + \frac{\partial}{\partial x}(\alpha_M \rho_M u_M^2) \\ &\qquad = -\alpha_M \frac{\partial P}{\partial x} - \alpha_M \rho_M g \left(\cos\beta \frac{\partial h}{\partial x} + \sin\beta\right) - F_M + F_i + \Psi + \Omega \end{aligned} \tag{2.27}$$

where subscript W , B and M refer to water, gas bubbles and liquid mixture phase respectively. α_M is the liquid mixture phase fraction accounts for the oil (subscript O), water and dispersed gas bubble phases, coupled together through drift flux approach (Hibiki and Ishii, 2003b; Ishii and Hibiki, 2006):

$$\alpha_M = \alpha_O + \alpha_W + \alpha_B \tag{2.28}$$

in which α_M is related to the gas voidage, α_G through the fundamental relation:

$$\alpha_M + \alpha_G = 1 \tag{2.29}$$

c_W and c_B are the water cut (water fraction within the liquid mixture) and bubble concentration respectively and they are defined as:

$$c_W = \frac{\alpha_W}{\alpha_M} \tag{2.30}$$

$$c_B = \frac{\alpha_B}{\alpha_M} \tag{2.31}$$

from which, the oil cut, c_O can be calculated:

$$c_O = \frac{\alpha_O}{\alpha_M} = \frac{\alpha_M - \alpha_W - \alpha_B}{\alpha_M} = 1 - c_W - c_B \tag{2.32}$$

ρ_M is the total liquid mixture density and is calculated as follow:

$$\rho_M = \frac{\alpha_0\rho_O + \alpha_W\rho_W + \alpha_B\rho_B}{\alpha_M} = (1 - c_B - c_W)\rho_O + c_W\rho_W + c_B\rho_B \tag{2.33}$$

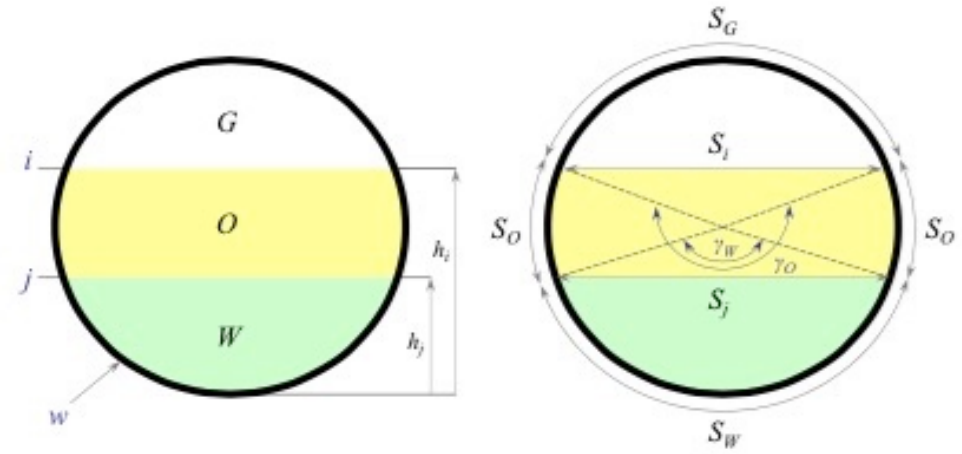


Figure 2.2: Geometrical parameters in gas/liquid/liquid stratified flow (Barbeau, 2008).

u_M is the liquid mixture centre of mass velocity:

$$u_M = \frac{\alpha_0 \rho_O u_O + \alpha_W \rho_W u_W + \alpha_B \rho_B u_B}{\alpha_M \rho_M} = \frac{(1 - c_B - c_W)\rho_O u_O + c_W \rho_W u_W + c_B \rho_B u_B}{\rho_M} \tag{2.34}$$

from which, the water and the oil velocities can be calculated from:

$$u_W = u_M - \frac{(1 - c_B - c_W)\rho_O u_S + c_B \rho_B u_{SB}}{\rho_M} \tag{2.35}$$

$$u_O = u_M + \frac{c_W \rho_W u_S + c_B \rho_B u_{SB}}{\rho_M} \tag{2.36}$$

where u_S is the oil-water slip velocity:

$$u_S = u_O - u_W \tag{2.37}$$

and u_{SB} is the slip velocity between the gas bubbles and the continuous liquid phase.

$$u_{SB} = u_M - u_B \tag{2.38}$$

The slip velocity is determined based on Ishii (1978) calculation, by assuming local steady state conditions for the oil and water momentum equations:

$$u_s = \sqrt{\frac{2A}{f_j \rho_O S_j} \left| \frac{(1 - c_W)\tau_{wW} S_W}{A} - \frac{c_W \tau_{wO} S_O}{A} + \frac{c_W \tau_i S_i}{A} + c_W \alpha_O (\rho_W - \rho_O) g \sin\beta \right|} \tag{2.39}$$

where, $\frac{\tau_{wW}S_W}{A}$, $\frac{\tau_{wO}S_O}{A}$ and $\frac{\tau_i S_i}{A}$ are the frictional forces for the wall-water, wall-oil, and gas-liquid respectively, and S_W, S_O, S_j and S_i are the weted parameters as depicted by Figure 2.2. In case of fully-dispersed liquids, the oil-water mixture is assumed to flow homogeneously (u_s=0). u_B can be approximated from a local balance between pressure and drag forces acting on the bubbles (Kempf and Issa, 2000):

$$u_B = u_M - \sqrt{\frac{-4d_B\left(dP/_{dx}\right)}{3C_D\rho_M}} \tag{2.40}$$

where d_B is the bubble diameter, assumed to be $1mm$ (Andreussi et al., 1993), $dP/_{dx}$ is the pressure gradient, C_D is the drag coefficient and can be evaluated from (Tomiyama et al., 1995):

$$C_D = \frac{C_{D_T}}{\alpha_{M_{ls}}} \text{ ; and}$$
$$C_{D_T} = \max\left[\frac{24}{Re_B}(1 + 0.15Re_B^{0.687}), \frac{8}{3}\frac{E_o}{E_o + 4}\right] \tag{2.41}$$

in which Re_B is the bubble Reynolds number and E_o is the bubble Eötvös number. They are given as:

$$Re_B = \frac{\rho_M d_B|u_M - u_B|}{\mu_M} \text{ ; and}$$
$$E_o = \frac{g{d_B}^2|\rho_M - \rho_G|}{\sigma} \tag{2.42}$$

Ψ and Ω in the mixture momentum equation (Equation 2.27) is defined as:

$$\Psi = \alpha_W(\rho_W - \rho_O)g\cos\beta\frac{\partial(h - h_j)}{\partial x} \tag{2.43}$$

$$\Omega = \frac{\partial}{\partial x}\left(-\alpha_M u_S^2 \frac{c_W\rho_W(1 - c_B - c_W)\rho_O}{\rho_M}\right) \tag{2.44}$$

F_M in Equation (2.27) represents the liquid mixture-wall drag force, and depends on the liquid flow pattern:

$$F_M = \begin{cases} -\frac{\tau_{wW}S_W}{A} - \frac{\tau_{wO}S_O}{A}, & \text{for stratified flow} \\ -\frac{\tau_{wM}S_M}{A}, & \text{for dispersed flow} \end{cases} \tag{2.45}$$

in which τ_{wW}, τ_{wO} and τ_{wM} represent the water-wall, oil-wall and liquid mixture-wall shear stresses respectively:

$$\tau_{wW} = \frac{1}{2}\rho_W f_W u_W^2 \tag{2.46}$$

$$\tau_{wO} = \frac{1}{2}\rho_O f_O u_O^2 \tag{2.47}$$

$$\tau_{wM} = \frac{1}{2}\rho_M f_M u_M^2 \tag{2.48}$$

where f_W, f_O and f_M are the friction factors which are determined empirically.

$\dot{M}_B$ in Equation (2.22), Equation (2.23), and Equation (2.25) is the rate of mass exchange of gas, between the total liquid phase and the gas phase (the rate of gas entrainment). The formulation of this closure relation depends on the flow regime and is defined in Section 2.2.2.2.2.

2.2.2.1.1 Emulsion viscosity

The dynamic viscosities of the pure phases (gas, oil or water) are set as initial values. In the case of liquid dispersions (water-in-oil or oil-in water), the apparent viscosity of the emulsion (including gas bubbles in the liquid mixture) is calculated from Brinkman (1952) model:

$$\mu_{emulsion} = \frac{\mu_c}{(1 - c_B - c_d)^{5/2}} \tag{2.49}$$

where μ_c is the viscosity of the continuous liquid phase (either oil viscosity, μ_O or water viscosity, μ_W) and c_d is the volume concentration of the dispersed phase (either water cut, c_W or oil cut, c_O)

2.2.2.2 Three-phase closure equations

The closure relations for the three-phase flow model include the friction factors for the wall and interface shear stresses for all the phases, the gas entrainment rate, the transitional condition of liquid-liquid stratified to liquid-liquid dispersion (and vice versa), and the phase inversion point for determining which liquid phase is continuous in case of liquid-liquid dispersion.

2.2.2.2.1 Friction factors

Like the two-phase flow, the two-fluid model for the three-phase flow requires empirical models to evaluate the friction factors for all the phases. The friction factors chosen for the three-phase model are based on the recommendation by Bonizzi (2003).

For the liquid-wall friction factors, the correlation of Hand (1991) is used:

$$f_{wk} = \begin{cases} \dfrac{24}{Re_k}\ , & Re_k \leq 2100 \\ 0.0262(\alpha_k Re_k)^{-0.139}\ , & Re_k > 2100 \end{cases} \tag{2.50}$$

where the subscript k can be either the water or the oil phase. The Reynolds number, Re_k is expressed by:

$$Re_k = \frac{D_k \rho_k u_k}{\mu_k} \tag{2.51}$$

where D_k is the liquid hydraulic diameter, defined as:

$$D_k = \frac{4A\alpha_k}{S_k} \tag{2.52}$$

The correlation from Taitel and Dukler (1976) is also applied to the three-phase flow for the gas-wall friction factor and the gas-oil interfacial friction factor (with the assumption that the oil phase is lighter than the water phase):

$$f = \begin{cases} 16Re^{-1}\ , & Re_k \leq 2100 \\ 0.046(Re)^{-0.2}\ , & Re_k > 2100 \end{cases} \tag{2.53}$$

where the Reynolds number for the gas phase is defined as:

$$Re_G = \frac{D_G \rho_G u_G}{\mu_G} \tag{2.54}$$

where D_G is the gas hydraulic diameter, defined as:

$$D_G = \frac{4A\alpha_G}{S_i + S_G} \tag{2.55}$$

the Reynolds number for the gas-oil interface can be calculated from:

$$Re_i = \frac{D_G \rho_G (u_G - u_O)}{\mu_G} \tag{2.56}$$

The oil-water interfacial factor, f_j is taken as a constant, recommended by Taitel et al. (1995), Barnea and Taitel (1996) and Khor et al. (1997):

$$f_j = 0.014 \tag{2.57}$$

2.2.2.2.2 Gas Entrainment

The rate of gas entrainment for two-phase flow (Issa et al., 2006) and three-phase flow (Barbeau, 2008) is based on the model of Brauner and Ullmann (2004). The formula is formulated from the energy balance between the surface energy production due to the disintegration of the Taylor bubble tail into gas bubbles, and the flux of turbulent energy supplied by the penetrating liquid film 'jet'. For three-phase flow, the formulation of gas entrainment depends on the liquid flow patterns, either stratification of both oil and water or liquid dispersions:

$$\dot{M}_B = \begin{cases} \dot{m}_{B,O} + \dot{m}_{B,W} \ , & \text{liquid stratification} \\ \dot{m}_{B,c} \ , & \text{liquid dispersion} \end{cases} \tag{2.58}$$

in which:

$$\dot{m}_{B,O} = (1 - c_W) \frac{1}{400 C_{j,O}} \tilde{d}_{critG_O} (We_O - We_{crit_O})(u_t - u_{lf}) \alpha_{lf} \tag{2.59}$$

$$\dot{m}_{B,W} = (c_W) \frac{1}{400 C_{j,W}} \tilde{d}_{critG_W} (We_W - We_{crit_W})(u_t - u_{lf}) \alpha_{lf} \tag{2.60}$$

$$\dot{m}_{B,c} = \frac{1}{400 C_{j,c}} \tilde{d}_{critG_c} \left(We_c - We_{crit_c}\right)\left(u_t - u_{lf}\right)\alpha_{lf} \tag{2.61}$$

where u_t and u_{lf} represent the slug translational velocity and liquid film velocity respectively, and α_{lf} is the liquid film hold-up. In the following three equations, the subscript k can be either oil (O), water (W), or the continuous liquid (c), hence the Weber number (We_k), the crictical Weber number (We_{crit_k}), and the gas bubbles droplet critical diameter in the liquid slug ($\tilde{d}_{critG_k}$), for generic phase k can be evaluated from:

$$We_k = \frac{\rho_M D \left(u_{Ms} - u_{lf}\right)^2}{\sigma_{G-k}} \tag{2.62}$$

$$We_{crit_k} = \frac{100 C'}{\tilde{d}_{critG_k}} \tag{2.63}$$

$$\tilde{d}_{critG_k} = \sqrt{\frac{0.4\sigma_{G-k}}{|\rho_M - \rho_G| g D^2 \cos\beta}} \tag{2.64}$$

where σ_{G-k} is the surface tension between the gas phase and generic phase k and coefficients $C_{j,k}$ and C' are taken as 1 and (2/3) respectively. The model has shown good agreement (in Issa et al. (2006)) with the experimental data from Gregory et al. (1978) and Felizola and Shoham (1995) and an improvement compared to the hydraulic jump correlation previously implemented by Bonizzi and Issa (2003a).

2.2.2.2.3 Flow pattern transition

The transition from liquid-liquid stratified to liquid-liquid dispersion is modelled based on the correlation from Decarre and Fabre (1997). The correlation has been

tested by Bonizzi (2003) and it compares well with the experimental data from Odozi (2000). The transition from stratified to fully-dispersed liquid phase is determined from a criterion:

$$d_{max} \leq d_{crit_L} \tag{2.65}$$

where d_{max} is the maximum droplet diameter that can be generated under specific flow conditions:

$$d_{max} = \begin{cases} \frac{0.145}{2} D \frac{\sigma}{\mu_C U_M} \left(\frac{\mu_d}{\mu_C}\right)^{1/6} & Re_C \leq 2100 \\ \frac{1.15}{2^{2/5}} D \left(\frac{\rho_C D U_M^2}{\sigma}\right)^{-0.6} \left(\frac{f_C}{1-c_d}\right)^{-0.4} & Re_C > 2100 \end{cases} \tag{2.66}$$

and d_{crit_L} is the liquid droplet critical diameter, in which above this value, liquid-liquid dispersion cannot exist:

$$d_{crit_L} = \begin{cases} \sqrt{\left(\frac{6\sigma}{|\rho_W - \rho_O| g \cos\beta}\right)} & Re_C \leq 2100 \\ \min\left(\sqrt{\left(\frac{6\sigma}{|\rho_W - \rho_O| g \cos\beta}\right)}, \frac{3}{8} \frac{\rho_C}{|\rho_W - \rho_O|} \frac{f_C U_M^2}{g \cos\beta}\right) & Re_C > 2100 \end{cases} \tag{2.67}$$

where subscript C and d represent the continuous and dispersed phases respectively. σ is the liquid-liquid surface tension, U is the superficial velocity, f_C is the friction factor for the continuous phase and c_d is the dispersed phase concentration.

2.2.2.2.4 Phase inversion

The phase inversion is a phenomenon when the dispersed and continuous phases reverse roles in a liquid-liquid dispersion. The phase inversion generally causes a spike in the pressure gradient (Figure 2.3).

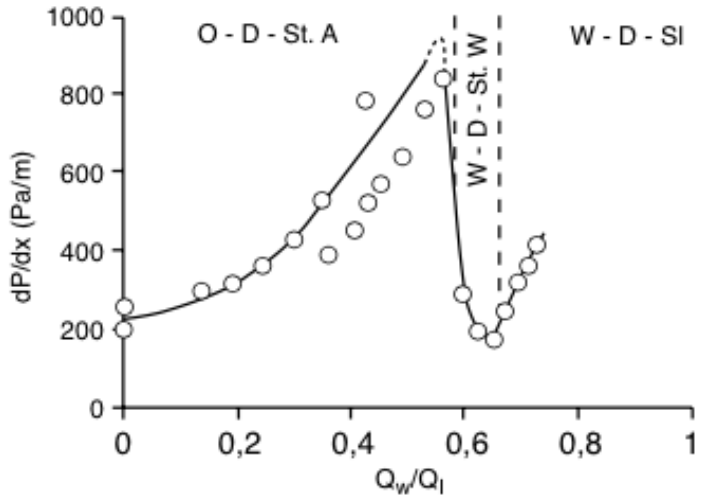


Figure 2.3: The influence of phase inversion on the pressure gradient (Pan, 1996)

This phenomenon is predicted through a critical phase fraction at which the inversion occurs. For example, for water-in-oil dispersion, the condition when the water phase will become continuous is:

$$\lambda_W \leq \lambda_W^{inv} \tag{2.68}$$

where λ_W is the water fraction within the oil phase and λ_W^{inv} is the critical water fraction above which, the inversion will occur.

λ_W is calculated by assuming both the water and oil locally flow in an equivalent pipe:

$$\lambda_W = \frac{\alpha_W}{\alpha_W + \alpha_O} = \frac{U_W}{U_W + U_O} \tag{2.69}$$

and λ_W^{inv} is calculated based on the formulation from Decarre and Fabre (1997), and depends on the flow regime when phase inversion occurs:

$$\lambda_W^{inv} = \begin{cases} 1 - \left[1 + \left(\frac{\mu_W}{\mu_O}\right)^{2/3}\right]^{-1}, & \text{flow remaining laminar} \\ 1 - \left[1 + \left(\frac{\mu_W}{\mu_O}\right)^{1/14}\left(\frac{\rho_W}{\rho_O}\right)^{5/14}\right]^{-1}, & \text{flow remaining turbulent} \end{cases} \tag{2.70}$$

and for a transition from laminar to turbulent (when oil is the continuous phase) or turbulent to laminar (when water is the continuous phase), a non-linear equation is obtained:

$$\frac{\lambda_W^{inv\,7/5}}{1 - \lambda_W^{inv}} = \frac{0.145}{1.15 \times 2^{3/5}} (\sigma_{O-W} f_{wW})^{2/5} (D\rho_W)^{3/5} \frac{|U_M|^{0.2}}{\mu_O^{5/6} \mu_W^{1/6}} \tag{2.71}$$

2.3 Review of Gas Hydrate Formation

2.3.1 Driving forces for hydrate nucleation

The driving force for hydrate nucleation is also sometimes called supersaturation in the literature, has been expressed in different forms by different researchers. For example, supersaturation can be expressed by the difference in the system pressure and the hydrate equilibrium pressure (Turner et al., 2009), the difference in the

gas fugacity and the hydrate equilibrium fugacity (Englezos et al., 1987a; Englezos et al., 1987b), and the difference in gas mole fraction (Skovborg and Rasmussen, 1994) or gas concentration (Herri et al., 1999) at the gas-liquid interface and in the liquid bulk phase. Vysniauskas and Bishnoi (1983); Vysniauskas and Bishnoi (1985) and Turner et al. (2005) used the difference between the system temperature and the hydrate equilibrium temperature, which is also defined as subcooling (or supercooling).

2.3.2 Hydrate growth rate experiments and modelling

Vysniauskas and Bishnoi (1983) were among the firsts in studying the kinetic of hydrate formation comprehensively. They measured the rate of hydrate formation, in terms of gas consumption rate, in a semi-batch stirred tank reactor between methane gas and water (hydrate structure I). The kinetic data were obtained by contacting methane gas with water, at different stirring rate, maintained at isobaric and isothermal conditions. They found that the formation rate depends on the impeller speed (the interfacial area between the gas and the liquid phase increases with stirring rate), the system pressure and temperature, and the degree of subcooling. They observed that the gas consumption rate decreases with an increase in temperature. Vysniauskas and Bishnoi (1985) further verified that the observed effects also occur with ethane gas. Following their experiments, Vysniauskas and Bishnoi (1983) proposed one of the first mathematical models to describe the rate of hydrate formation. In their semi-empirical model, the rate of

gas consumption is correlated against the total gas-liquid interfacial area, pressure, temperature and subcooling and came up with:

$$\frac{\partial n}{\partial t} = \mathcal{E}_1 A_s exp\left(-\frac{E_a}{RT}\right) exp\left(-\frac{\mathcal{E}_2}{\Delta T^{\mathcal{E}_3}}\right) P^{\mathcal{E}_4} \tag{2.72}$$

where n, R, T, P are respectively the mole of gas consumed, gas constant, temperature and pressure. The constants $\mathcal{E}_1$, $\mathcal{E}_2$, $\mathcal{E}_3$, $\mathcal{E}_4$ and the activation energy, E_a are empirical parameters fitted to the measured experimental data. The gas-liquid surface area, A_s was calculated by measuring the contour of the vortex induced by the impeller for different stirring rates at atmospheric pressure.

Englezos et al. (1987b) measured the hydrate formation rate from three gaseous mixtures of methane and ethane. They observed that the mechanism of hydrate formation is similar to that of pure gas (Englezos et al., 1987a) and not limited to the interface, but also occurs in the liquid bulk. They also found that the gas consumption rate strongly depends on the mixture composition as it will change the fugacity of the dissolved gas and the equilibrium hydrate, and subsequently alters the magnitude of the driving force. Englezos et al. (1987a) proposed a model for the hydrate growth as a two step process: first, the diffusion of dissolved gas molecules from bulk of the solution to the crystal-water surface, and then, the adsorption process, where gas molecules are incorporated into the structured water framework. For a single hydrate crystal, they suggested:

$$\left(\frac{\partial n}{\partial t}\right)_P = K^* A_P \left(f' - f'_{eq}\right) \tag{2.73}$$

where n, A_P, and $\left(f' - f'_{eq}\right)$ stand for moles of gas consumed, hydrate crystal surface area and the driving force in terms of the fugacity difference (between the gas and the hydrate equilibrium) respectively. K^* is the combined rate parameter of the reaction rate constant, k_r and the mass transfer coefficient around the particle, k_d:

$$\frac{1}{K^*} = \frac{1}{k_r} + \frac{1}{k_d} \tag{2.74}$$

The value of K^* is fitted to the experimental data for each stirring rate. The global reaction rate accounted for all the particles of any size, $R(t)$ is obtained by integrating the rate per particle for all particles:

$$R(t) = \int_0^\infty \left(\frac{\partial n}{\partial t}\right)_P \mathcal{P}(r,t)dr = 4\pi K^* \mu_2 \left(f - f_{eq}\right) \tag{2.75}$$

where r is the particles radius, $\mathcal{P}(r,t)$ is the particles distribution and μ_2 is the second moment of the particle size distribution:

$$\mu_2 = \int_0^\infty r^2 \, \mathcal{P}(r,t)dr \tag{2.76}$$

The aforementioned experiments and modelling are the fundamental experiments and restricted only to the gas and water phase. Gaillard et al. (1999) performed experiments in flow loop with oil, water and dissolved gas to mimic the behaviour of hydrate formation in pipelines. They found that the transport of dissolved gas in the bulk oil to the water phase is the rate-determining step in the

overall hydrate formation rate. The gas consumption rate increases as the liquid flow rate increases due to turbulence.

Turner et al. (2009) investigated the hydrate formation mechanism in water-in-oil dispersions using an autoclave reactor. They suggested that hydrate formation in water-in-oil dispersion system occurs in two steps. The first step is gas dissolution from the gas phase into the bulk oil, and the second step is the mass transfer of dissolved gas across the hydrate shell. They found that the initial hydrate formation rate greatly depends on the shear rate. An increase in the shear rate results in a higher formation rate due to the smaller water droplets, which subsequently increases the total surface area for hydrate formation. Moreover, with high shear rate, an increase in the gas-oil interfacial area and a decrease in the gas-oil diffusive layer were observed, allowing gas to dissolve in the oil phase easily. A similar observation was found for a series of flow loop experiments performed by Turner (2006) and this confirmed the observation of turbulence effect from Gaillard et al. (1999). Following this observation, Turner et al. (2009) modelled the rate of gas dissolution by:

$$\frac{dn_{G,O}}{dt} = k_{G-O} A_{G-O} \left(C_{G,O}^{eq,G} - C_{G,O} \right) \tag{2.77}$$

where $n_{G,O}$ is the number of moles of gas transferred into the oil, k_{G-O} is the adsorption mass transfer coefficient, A_{G-O} is the gas-oil interfacial area, $C_{G,O}$ is the gas concentration in the oil phase and $C_{G,O}^{eq,O}$ is the equilibrium gas concentration in the oil phase. For the hydrate growth in water-in-oil dispersions system, Turner et al. (2009) proposed an inward-growing shell (also known as shrinking-core) model:

$$-\frac{dr_c}{dt} = \frac{D_{G-H}C_{G,O}}{\rho_H \theta_{G-H}} \left(\frac{1}{r_W - \frac{r_W^2}{r_p}} \right) \tag{2.78}$$

where r_W is the water core radius, $D_{G,H}$ is the diffusivity of dissolved gas across hydrate shell, ρ_H is the hydrate density, θ_{G-H} is the number of moles of gas per mole of hydrate (based on stoichiometric relation) and r_p is the droplet (or the particle) radius. They concluded that hydrate growth is limited by the mass transfer of dissolved gas across the hydrate shell since the mass transfer of gas into the oil phase is so rapid and the dissolved gas consumed by hydrate formation is quickly replenished.

The team at the Centre of Hydrate Research, Colorado School of Mines developed a hydrate kinetics model, CSMHyK to predict hydrate formation in oil-dominated pipelines (Turner et al., 2005; Boxall et al., 2009). To validate their hydrate kinetics model, Turner (2006) and Boxall (2009) performed a series of flow loop experiments. They modelled the hydrate formation from a first-order expression of the reaction rate, based on intrinsic kinetics equation (Vysniauskas and Bishnoi, 1983) with an adjustable rate constant:

$$-\frac{dm_H}{dt} = u' k_1 e^{\left(\frac{k_2}{T_{sys}}\right)} A_s (\Delta T_{sub}) \tag{2.79}$$

where k_1 and k_2 are the intrinsic rate constants regressed from the Vysniauskas and Bishnoi (1983) laboratory data, A_s is the surface area between water and oil phase and ΔT_{sub} is the thermal driving force defined as the difference between

equilibrium hydrate temperature and the temperature of the system. u' is a fitted rate constant used to modify the reaction rate constant, k_1 and k_2. This modification is necessary due to the differences in the systems studied:

1. Vysniauskas and Bishnoi (1983) examined hydrate formation in an autoclave cell between water and gas while Turner et al. (2005) examined hydrate formation in a flow loop of water dispersed in oil system.

2. Hydrates expected to form at the water-gas interface in Vysniauskas and Bishnoi (1983) experiment and at oil-water interface in the Turner et al. (2005) experiment where oil may provide additional resistance for hydrate formation.

The main assumption with this model is that during formation, water droplets convert into full-size solid hydrate particles with a uniform diameter, hence, gas consumption only results in increased hydrate particle numbers. This model has been successfully applied to the subsea tieback (Davies et al., 2008; Zerpa et al., 2011), however, it is restricted to a flow where the free gas phase is continuously available as this model uses the free gas phase as the source of the hydrate former. In case of a slug flow for example, where no free gas is available in the slug body region, this model would fail to predict hydrate formation. This model is improved in this thesis to cater to this restriction and is further discussed in Chapter 3.

Lo (2011) extended the modelling approach of Turner et al. (2005) to a three-dimensional analysis with the assumption that oil is the continuous fluid carrying water droplets and gas bubbles. Following Turner et al. (2009), he also

proposed a two-step hydrate formation mechanism: the first step is gas dissolution into the oil phase and the second step is the consumption of the dissolved gas to form hydrates. The mass transfer of gas from the gas bubbles into the oil phase (gas dissolution), $\dot{m}_{DG}$ is calculated as:

$$\dot{m}_{DG} = k_{DG} A_{S,B} \rho_O \left(Y_{DG}^{eq} - Y_{DG}^{O}\right) \tag{2.80}$$

where, k_{dis} is the mass transfer coefficient, $A_{S,B}$ is the surface area density of gas bubbles, Y_{DG}^{O} is the mass fraction of dissolved gas in oil, Y_{DG}^{eq} is the equilibrium mass fraction of dissolved gas in oil defined as:

$$Y_{DG}^{eq} = \frac{X_{DG}^{eq} W_G}{W_O} \tag{2.81}$$

$$X_{DG}^{eq} = \frac{P}{H_G} \tag{2.82}$$

where, W_G is the molecular weight for gas and W_O is for oil. X_{DG}^{eq} is the equilibrium mole fraction of dissolved gas in oil, P is the system pressure and H_G is Henry's constant of dissolved gas in oil. The dissolved gas in oil is therefore available for hydrate formation at the surface of the water droplets when the flow conditions are right, and this consumption rate is modelled as the mass transfer from the oil to the water phase:

$$\dot{m}_H = k_{hyd} a_W \Delta T f_Y (1 - f_H) \tag{2.83}$$

where k_{hyd} is the mass transfer coefficient for hydrate formation, a_W is the surface area density of the water droplets/hydrates, ΔT is the driving force in terms of

subcooling, f_Y is the dissolved gas factor so that when the dissolved gas is depleted the mass transfer stops:

$$f_Y = \frac{Y_{DG}^{O}}{Y_{DG}^{eq}} \tag{2.84}$$

f_H is the hydrate fraction, where $f_H = 1$ denotes pure hydrate particles while $f_H = 0$ denotes pure water droplet.

2.3.3 Agglomeration and hydrate slurry viscosity

In general, hydrate particles cause an increase in the viscosity of the carrying fluid. As the hydrate particles agglomerate with each other, the slurry viscosity increases drastically and eventually forms a plug in the pipeline.

In their experiment, Andersson and Gudmundsson (2000) showed that the apparent viscosity for the hydrate-in-water slurries increases as the hydrate volume fraction increases. The same observation was found in the experiment conducted by Camargo et al. (2000) for hydrate formation in water-in-oil dispersions system. They observed that the water-in-oil emulsion viscosity increased as the water converted into hydrates, and the increase in the water content, caused an increase to the viscosity of the emulsion and hydrate suspension. Camargo et al. (2000) also showed that the emulsion and the hydrates suspension generally behaves like a Newtonian fluid, however, at higher volume fraction, shear-thinning behaviour was observed.

Sinquin et al. (2004) showed in their experiment that hydrate formation modifies the flow properties of the flowing fluid, and causes an increase in the

pressure drop of the system. In laminar flow, the pressure drop (due to the presence of hydrates) is controlled by the apparent viscosity while in turbulent flow, it is controlled by the friction factor. They modelled the relative viscosity (the ratio between the apparent viscosity of the suspension and the viscosity of the carrying fluid) using a proposed equation from Mills (1985), which is adapted to hard spheres of uniform diameter and accounted only for hydrodynamic interactions:

$$\mu_r = \frac{1 - \emptyset}{\left(1 - \frac{\emptyset}{\emptyset_{max}}\right)^2} \tag{2.85}$$

in which, $\emptyset$ is the volume fraction of hydrate particles in the carrying fluid and $\emptyset_{max}$ is the maximum volume fraction to which particles of same diameter can pack. However, when an agglomeration of the hydrate particles is taken into consideration, an effective volume fraction, $\emptyset_{eff}$ must be used instead, accounted for the porosity and the fractal nature of hydrate aggregates. Hence, the relative viscosity can be calculated from:

$$\mu_r = \frac{1 - \emptyset_{eff}}{\left(1 - \frac{\emptyset_{eff}}{\emptyset_{max}}\right)^2} \tag{2.86}$$

Basic mechanisms involved in hydrate agglomeration are not yet definitively established (Colombel et al., 2009). In the literature, there are two main mechanisms for agglomeration of hydrate particles: the shear-limited agglomeration and the contact-induced agglomeration. The shear-limited mechanism is where the size of hydrate aggregates are determined by the balance

between the hydrodynamic force exerted on the aggregates and the inter-particle adhesion force inside the aggregates.

Sinquin et al. (2004) showed that the size of the hydrate aggregate can be calculated by solving a steady-state balance equation between the inter-particle adhesion force and the shear forces:

$$\left(\frac{d_A}{d_P}\right)^{4-fr} - \frac{F_a\left[1-\frac{\emptyset}{\emptyset_{max}}\left(\frac{d_A}{d_P}\right)^{3-fr}\right]^2}{d_P^2\mu_0\dot{\gamma}\left[1-\emptyset\left(\frac{d_A}{d_P}\right)^{3-fr}\right]} = 0 \tag{2.87}$$

where d_A is the aggregate diameter, d_P is the hydrate particles diameter, fr is the fractal dimension that accounts for the porosity of the aggregate, F_a is the normalized inter-particle adhesion force, μ_0 is the carrying fluid viscosity and $\dot{\gamma}$ is the shear rate. The effective volume fraction of the aggregate is then calculated from:

$$\emptyset_{eff} = \emptyset\left(\frac{d_A}{d_P}\right)^{3-fr} \tag{2.88}$$

This approach has been shown to give good agreement with experimental data (Pauchard et al., 2007), and is widely used by researchers.

The less used mechanism is the contact induced mechanism, which is the result of the contact between a hydrate particle and a water droplet (due to the hydrophilic nature of the hydrate particle). The contact is immediately followed by the crystallization of the water droplet and the formation of a solid crystal bridge (Gainville and Sinquin, 2011). This mechanism encourages aggregate growth and is

considered irreversible compared to shear-limited mechanism. However, as shown by Palermo et al. (2005), this approach failed to predict the final hydrate slurry viscosity for a wide range of water cuts and flow rates.

3 MODEL FORMULATION

3.1 Preamble

The present chapter describes the current model of the TRIOMPH code with the implementation of the hydrate kinetics routine. Since the hydrate formation in a typical flowline involves a mass transfer between three phases (gas, oil and water phases), the hydrate kinetics routine will be implemented in the existing framework developed by Barbeau (2008). In addition, in offshore deepwater systems, from the well to the export flowline, the temperature and pressure within the flow can vary drastically and these variations have a major impact on the flow regime and the fluid properties. Furthermore, the hydrate formation is a non-isothermal process, therefore, the ability for the model to predict the thermodynamic behaviour of a system is crucial. Without appropriate remediation, hydrate particles may agglomerate with each other, forming bigger aggregates with a potential to plug up the pipe. Hence, it is important to be able to estimate where and when this incident will occur.

Section 3.2 describes the current model with all the transport equations implemented, and is divided into three subsections; the continuity equations, the momentum equations, and the energy equation. Sections 3.3 through 3.5 describe the hydrate kinetics routine that is integrated in the current model. Section 3.3 describes the mass transfer of gas dissolving into oil (or gas dissolution rate) while section 3.4 describes the mass transfer of dissolved gas into water (hydrate formation rate). Section 3.5 concentrates on the closure relations for the agglomeration of the hydrate globules. Finally, the numerical implementation of the model together with the appropriate boundary conditions and the integration of the hydrate kinetics routine is explained in Section 3.6.

3.2 Transport Equations

In general, the transport equations solved in the Eulerian multiphase flow model can be written as follows:

Continuity Equation

The conservation of mass for phase k is:

$$\frac{\partial}{\partial t}(\alpha_k \rho_k) + \frac{\partial}{\partial x}(\alpha_k \rho_k u_k) = 0 \tag{3.1}$$

where α_k is the phase fraction for phase k and the summation of α_k is equal to unity.

$$\sum \alpha_k = 1 \tag{3.2}$$

Momentum Equation

The conservation of momentum for phase k is:

$$\frac{\partial}{\partial t}(\alpha_k \rho_k u_k) + \frac{\partial}{\partial x}\left(\alpha_k \rho_k u_k^2\right) = -\alpha_k \frac{\partial P}{\partial x} - \alpha_k \rho_k g \sin\beta + \sum F_k \tag{3.3}$$

where $\sum F_k$ is the summation of the interfacial and wall forces.

Energy Equation

The conservation of energy of the system is:

$$\begin{aligned}\left(\sum \alpha_k \rho_k C_{p_k}\right)\frac{\partial T}{\partial t} + \left(\sum \alpha_k \rho_k C_{p_k} u_k\right)\frac{\partial T}{\partial x} \\ = -\left(\sum \alpha_k \left(\frac{\partial \ln \rho}{\partial \ln T}\right)_P \frac{DP}{Dt}\right) - \left(\sum \tau_{wk} u_k\right) + \sum Q_k\end{aligned} \tag{3.4}$$

where C_{p_k} is the specific heat capacity for phase k, τ_{wk} is the wall shear stress acting on phase k, Q_k is the heat transfer term for phase k and T is the temperature of the system. A single non-conservative form of the energy equation, which assumes equal temperatures in all phases, has been chosen to reduce the computational effort and is explained in section 3.2.3.

3.2.1 Continuity equations

Since the hydrate formation process involves mass transfer between the three fluid phases (gas, water and oil), we model the flow by adapting the three phase Eulerian one-dimensional modelling framework developed by Bonizzi and Issa (2003b) and Barbeau (2008). The continuity equations implemented in the current model for all the phases are written out in full as follows:

The gas continuity equation:

$$\frac{\partial}{\partial t}(\alpha_G \rho_G) + \frac{\partial}{\partial x}(\alpha_G \rho_G u_G) = -\dot{M}_B - \dot{m}_{DG} \tag{3.5}$$

The liquid mixture (oil, water, gas bubbles) continuity equation:

$$\frac{\partial}{\partial t}(\alpha_M \rho_M) + \frac{\partial}{\partial x}(\alpha_M \rho_M u_M) = +\dot{M}_B + \dot{m}_{DG} - \dot{m}_H \tag{3.6}$$

The water phase continuity equation:

$$\frac{\partial}{\partial t}(c_W \alpha_M \rho_W) + \frac{\partial}{\partial x}(c_W \alpha_M \rho_W u_W) = \dot{m}_H \tag{3.7}$$

The conservation of mass of the gas bubble entrained:

$$\frac{\partial}{\partial t}(c_B \alpha_M \rho_G) + \frac{\partial}{\partial x}(c_B \alpha_M \rho_G u_B) = \dot{M}_B \tag{3.8}$$

The dissolved gas in oil continuity equation:

$$\frac{\partial}{\partial t}(f_{DG} \alpha_O \rho_O) + \frac{\partial}{\partial x}(f_{DG} \alpha_O \rho_O u_O) = \dot{m}_{DG} - \dot{m}_H \tag{3.9}$$

and the hydrate phase continuity equation (or water conversion) following the same approach by Lo (2011) is:

$$\frac{\partial}{\partial t}(f_H \alpha_W \rho_W) + \frac{\partial}{\partial x}(f_H \alpha_W \rho_W u_W) = +\dot{m}_H \left(\frac{W_H(n_W + 1)}{W_G n_G}\right) \tag{3.10}$$

where the subscript G, W, O, DG, H and M refers to gas, water, oil, dissolved gas, hydrate and liquid mixture respectively.

The gas and the liquid mixture fraction are linked through the basic relation:

$$\alpha_M + \alpha_G = 1$$

and α_M is the liquid mixture fraction resulting from coupling the water phase and the oil phase by means of a drift flux approach (Bonizzi, 2003),

$$\alpha_M = \alpha_W + \alpha_O + \alpha_B \tag{3.11}$$

c_W is the water cut defined as:

$$c_W = \frac{\alpha_W}{\alpha_M}\ ; \qquad c_B = \frac{\alpha_B}{\alpha_M} \tag{3.12}$$

from which the 'oil cut', c_O can be obtained from the relation:

$$c_O = \frac{\alpha_O}{\alpha_M} = 1 - c_W - c_B \tag{3.13}$$

and with gas is dissolving into oil, c_O hereafter defined as 'live oil cut' and equal to

$$c_O = c_{DO} + c_{DG} \tag{3.14}$$

where c_{DO} is the 'dead oil cut' and c_{DG} is the 'dissolved gas cut'. f_{DG} is the volume fraction of dissolved gas in oil and defined as:

$$f_{DG} = \frac{c_{DG}}{c_O} = \frac{c_{DG}}{1 - c_W - c_B} \tag{3.15}$$

When the conditions are met, some of the water converts into hydrates, hence c_W is equal to

$$c_W = c_H + c_{PW} \tag{3.16}$$

where c_H and c_{PW} refers to 'hydrate cut' and 'unconverted water cut' respectively. f_H is the hydrate volume fraction (or water conversion) and defined as

$$f_H = \frac{c_H}{c_W} \tag{3.17}$$

Therefore as an alternative to Equation (3.10), the conservation of mass for the unconverted water can be used:

$$\frac{\partial}{\partial t}(f_{PW}\alpha_W\rho_w) + \frac{\partial}{\partial x}(f_{PW}\alpha_W\rho_w u_w) = -\dot{m}_H\left(\frac{W_W n_W}{W_G n_G}\right) \tag{3.18}$$

where f_{PW} is the unconverted water fraction and linked together with f_H through the relation:

$$f_H + f_{PW} = 1 \tag{3.19}$$

Figure 3.1 illustrates the model variables and their relations implemented in the current model. One major advantage of coupling some of the phases together is, no further modifications are required for a number of model variables (for instance the densities and the velocities) within the framework of Barbeau (2008). Hence, the liquid mixture density, ρ_M is defined as:

$$\rho_M = \frac{\alpha_W\rho_W + \alpha_O\rho_O + \alpha_B\rho_G}{\alpha_M} = (1 - c_W - c_B)\rho_O + c_W\rho_W + c_B\rho_G \tag{3.20}$$

the gas density is calculated based on ideal gas law:

$$\rho_G = \frac{P}{zR_G T} \tag{3.21}$$

where z and R_G refers to the gas compressibility factor the gas constant respectively. The liquid mixture velocity, u_M, following Barbeau (2008):

$$u_M = \frac{c_W \rho_W u_W + (1 - c_W - c_B)\rho_O u_O + c_B \rho_G u_B}{\rho_M} \tag{3.22}$$

from which the velocity for the water phase and the oil phase can be defined as:

$$\begin{aligned} u_W &= u_M - \frac{(1 - c_W - c_B)\rho_O u_s + c_B \rho_G u_{s_B}}{(1 - c_W - c_B)\rho_O + c_W \rho_W} \ ; \\ u_O &= u_M + \frac{c_W \rho_W u_s - c_B \rho_G u_{s_B}}{(1 - c_W - c_B)\rho_O + c_W \rho_W} \end{aligned} \tag{3.23}$$

where u_s and u_{s_B} are the slip velocities and defined as:

$$u_s = u_O - u_W \ ; \quad u_{s_B} = u_B - u_M \tag{3.24}$$

The slip velocity is determined based on the formulation explained in Section 2.2.2.1. $\dot{m}_{DG}$ is the rate of gas dissolving into the oil phase and $\dot{m}_H$ is the rate of hydrate formation, and is defined in Section 3.3 and 3.4 respectively. The term $\left(\frac{W_H(n_W+1)}{W_G n_G}\right)$ in (3.10) is the mass of hydrates formed per 1kg of gas consumed while the term $\left(\frac{W_W n_W}{W_G n_G}\right)$ in Equation (3.18) is the mass of water consumed per 1kg of gas consumed. W is the molecular weight and n is the mole number. The value of n is chosen based on stoichiometric equation for hydrate formation, and n_W is also known as the hydration number; water molecules per guest molecule (Sloan and

Koh, 2007). For example, for methane hydrates (hydrate structure I), when all water cavities have been filled by guest (methane) molecule, the hydration number, n_W is equal to 5.75 (Sloan and Koh, 2007; Carroll, 2008).

3.2.2 Momentum equations

Since the motion of the liquid mixture can be coupled together by means of drift flux approach, only two momentum equations are needed. The two momentum equations are listed below:

The gas momentum equation:

$$\frac{\partial}{\partial t}(\alpha_G \rho_G u_G) + \frac{\partial}{\partial x}(\alpha_G \rho_G u_G^2) = -\alpha_G \frac{\partial P}{\partial x} - \alpha_G \rho_G g \sin\beta - F_{wG} - F_i \tag{3.25}$$

The liquid mixture momentum equation:

$$\begin{aligned} &\frac{\partial}{\partial t}(\alpha_M \rho_M u_M) + \frac{\partial}{\partial x}(\alpha_M \rho_M u_M^2) \\ &\qquad = -\alpha_M \frac{\partial P}{\partial x} - \alpha_M \rho_M g \left(\cos\beta \frac{\partial h}{\partial x} + \sin\beta\right) - F_{wM} + F_i + \Psi + \Omega \end{aligned} \tag{3.26}$$

where Ψ is defined as

$$\Psi = \alpha_W (\rho_W - \rho_O) g \cos\beta \frac{\partial(h - h_j)}{\partial x} \tag{3.27}$$

and Ω is defined as

$$\Omega = \frac{\partial}{\partial x}\left(-\alpha_M u_S^2 \frac{c_W \rho_W (1 - c_W - c_B)\rho_O}{\rho_M}\right) \tag{3.28}$$

The derivation of the liquid mixture momentum equation is given in Appendix A.

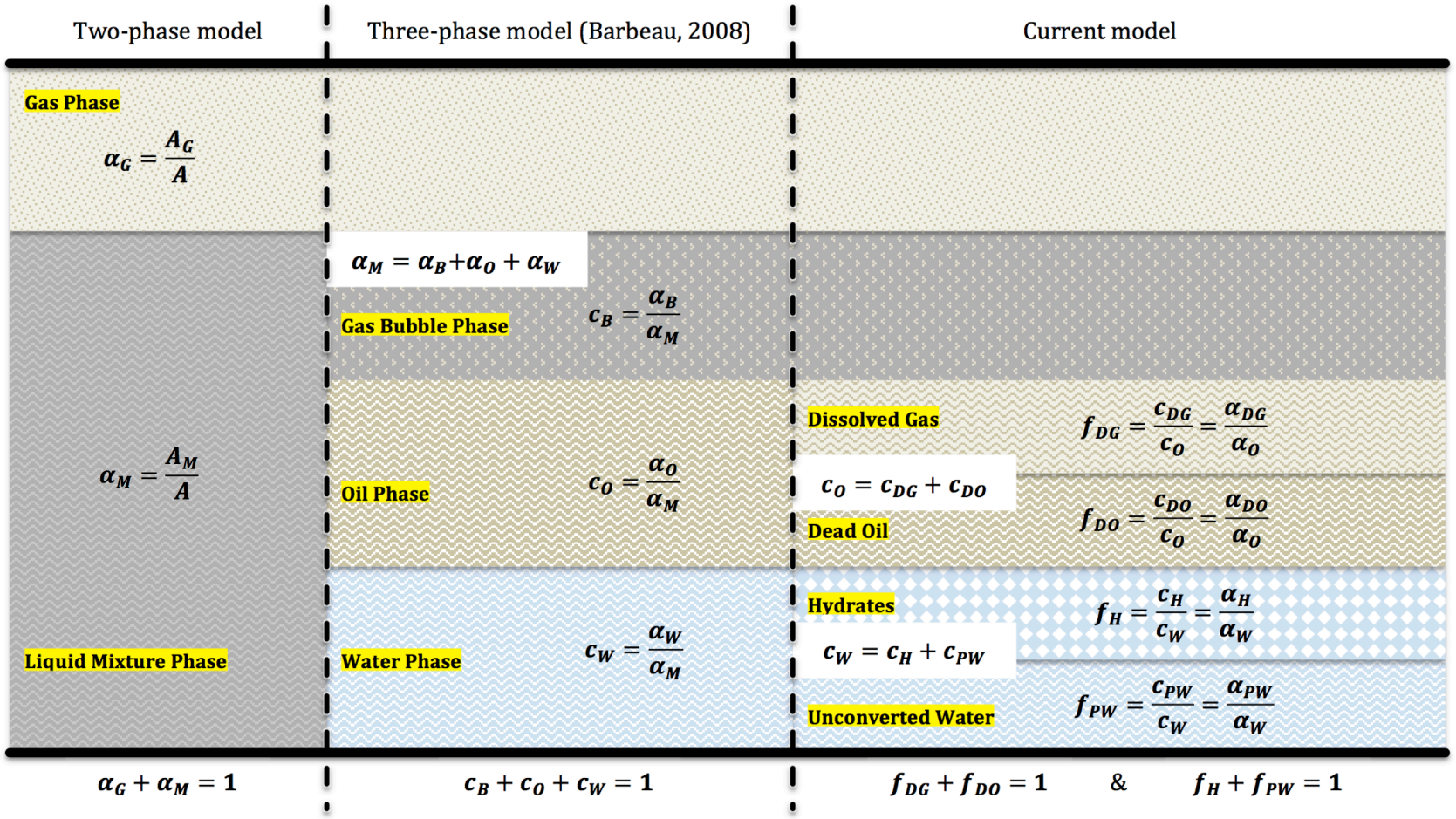


Figure 3.1: Model variables and their relations

3.2.3 Energy equation

3.2.3.1 The derivation of energy equation

Since hydrate formation is a non-isothermal process, the modelling of the thermodynamic behaviour of the phases within the flow is essential. The objective is to apply an energy equation in the framework of the existing three-phase TRIOMPH code (Bonizzi, 2003). From Byron Bird et al. (2002), the energy equation adopted is:

$$\frac{D}{Dt}(\rho C_p T) = -\left(\frac{\partial \ln \rho}{\partial \ln T}\right)_P \frac{DP}{Dt} + \rho T \frac{DC_p}{Dt} - (\tau : \nabla u) + Q \tag{3.29}$$

where C_p is the specific heat capacity, T is the temperature, Q is the heat transfer term. $(\tau : \nabla u)$ is the rate of heat generation due to the viscous forces and for one-dimensional flow it reduces to $(\tau_w u)$, where τ_w is the shear stress acting on the wall. Frictional heating due to the interfacial viscous forces is generally very small and can be considered negligible. The temperature variation within the fluid is small and can also be considered negligible, hence local thermodynamic equilibrium is assumed, and the temperature is equal for all phases. Therefore, the energy equation for an individual phase k, becomes:

$$\begin{aligned} &\frac{\partial}{\partial t}(\alpha_k \rho_k C_{p_k} T) + \frac{\partial}{\partial x}(\alpha_k \rho_k C_{p_k} T u_k) \\ &\qquad = -\alpha_k \left(\frac{\partial \ln \rho}{\partial \ln T}\right)_P \frac{DP}{Dt} + \alpha_k \rho_k T \frac{DC_{p_k}}{Dt} - (\tau_{wk} u_k) + Q_k \end{aligned} \tag{3.30}$$

Equation (3.30) is the conservative form of the energy equation, the non-conservative form of the equation is:

$$\left(\alpha_k \rho_k C_{p_k}\right)\frac{\partial T}{\partial t} + \left(\alpha_k \rho_k C_{p_k} u_k\right)\frac{\partial T}{\partial x} = -\alpha_k \left(\frac{\partial \ln \rho}{\partial \ln T}\right)_P \frac{DP}{Dt} - \left(\tau_{wk} u_k\right) + Q_k \tag{3.31}$$

note that the term $\alpha_k \rho_k T \frac{DC_p}{Dt}$ has been eliminated from the equation. As a result, the computational effort can be significantly reduced. The full derivation from the conservative form (Equation 3.30) to non-conservative form (Equation 3.31) is given in Appendix B.

For a typical flowline, heat transfer is generally due to convection and conduction. Heat transfer from radiation is relatively insignificant and can be omitted (Bai and Bai, 2005). Hence, the term Q_k is defined as:

$$Q_k = U_k(T - T_\infty) \tag{3.32}$$

$$U_k = \frac{1}{\frac{1}{h_k} + \frac{\lambda_{pipe}}{\chi_{pipe}} + \frac{1}{h_\infty}} \tag{3.33}$$

where the first term of the denominator in Equation (3.33) is from internal convection, the second term is from conduction and the third term is from external convection. λ_{pipe} is the thermal conductivity coefficient of the pipe, χ_{pipe} is the thickness of the pipe and h_∞ is the external convective heat transfer coefficient. For natural convection in water, h_∞ can be taken as $200\, W/m^2K$ (Bai and Bai, 2005). h_k is the internal heat transfer coefficient and depends on the Nusselt number, Nu:

$$Nu = \frac{h_k D_k}{\lambda_k}$$

$$Nu = \begin{cases} 2 + 0.6Re^{1/2}Pr^{1/3} & \text{for laminar flow; } Re < 2100 \\ 0.023Re^{0.8}Pr^{0.33} & \text{for turbulent flow; } Re > 2100 \end{cases} \quad (3.34)$$

which D_k denotes the hydraulic diameter and λ_k denotes the thermal conductivity of the flowing fluid.

The term $\left(\frac{\partial \ln \rho}{\partial \ln T}\right)$ in Equation (3.31) is -1 for ideal gas and 0 for incompressible fluid (Byron Bird et al., 2002), thus the individual energy equation for water (subscript W), oil (subscript O) and gas (subscript G) are:

$$\left(\alpha_W \rho_W C_{p_W}\right)\frac{\partial T}{\partial t} + \left(\alpha_W \rho_W C_{p_W} u_W\right)\frac{\partial T}{\partial x} = -(\tau_{wW} u_W) + Q_W \quad (3.35)$$

$$\left(\alpha_O \rho_O C_{p_O}\right)\frac{\partial T}{\partial t} + \left(\alpha_O \rho_O C_{p_O} u_O\right)\frac{\partial T}{\partial x} = -(\tau_{wO} u_O) + Q_O \quad (3.36)$$

$$\left(\alpha_G \rho_G C_{p_G}\right)\frac{\partial T}{\partial t} + \left(\alpha_G \rho_G C_{p_G} u_G\right)\frac{\partial T}{\partial x} = \alpha_G \frac{\partial P}{\partial t} + \alpha_G u_G \frac{\partial P}{\partial x} - (\tau_{wG} u_G) + Q_G \quad (3.37)$$

and since the temperature of all the phases assumed to be uniform, the final energy equation implemented in the current model is:

$$\begin{aligned} &\left(\alpha_W \rho_W C_{p_W} + \alpha_O \rho_O C_{p_O} + \alpha_G \rho_G C_{p_G}\right)\frac{\partial T}{\partial t} \\ &\quad + \left(\alpha_W \rho_W C_{p_W} u_W + \alpha_O \rho_O C_{p_O} u_O + \alpha_G \rho_G C_{p_G} u_G\right)\frac{\partial T}{\partial x} \\ &\quad = \alpha_G \frac{\partial P}{\partial t} + \alpha_G u_G \frac{\partial P}{\partial x} - (\tau_{wW} u_W + \tau_{wO} u_O + \tau_{wG} u_G) \\ &\quad + (Q_W + Q_O + Q_G) \end{aligned} \quad (3.38)$$

3.3 Gas Dissolution Rate

Following the approach of Lo (2011) which is based on Fick's law for diffusion, the mass transfer from the gas to the oil phase can be modelled as:

$$\dot{m}_{DG} = k_{\mathrm{DG}} A_{G-O} \rho_O \left(f_{DG}^{eq} - f_{DG}\right) \tag{3.39}$$

where k_{DG} is the mass transfer coefficient, which can be found from the experiment done by Turner (2006) (Figure 3.2).

A_{G-O} is the contact surface area between the gas phase and the oil phase, f_{DG}^{eq} is the equilibrium (or saturation) mass fraction of dissolved gas in oil which can be obtained as follows:

$$f_{DG}^{eq} = \frac{X_{DG}^{eq} W_G}{W_O} \tag{3.40}$$

$$X_{DG}^{eq} = \frac{P_{sys}}{H_G} \tag{3.41}$$

where, W_G is the molecular weight for the gas and W_O is for the oil. X_{DG}^{eq} is the equilibrium mole fraction of dissolved gas in oil, P_{sys} is the system pressure and H_G is Henry's constant of the dissolved gas which is usually found experimentally.

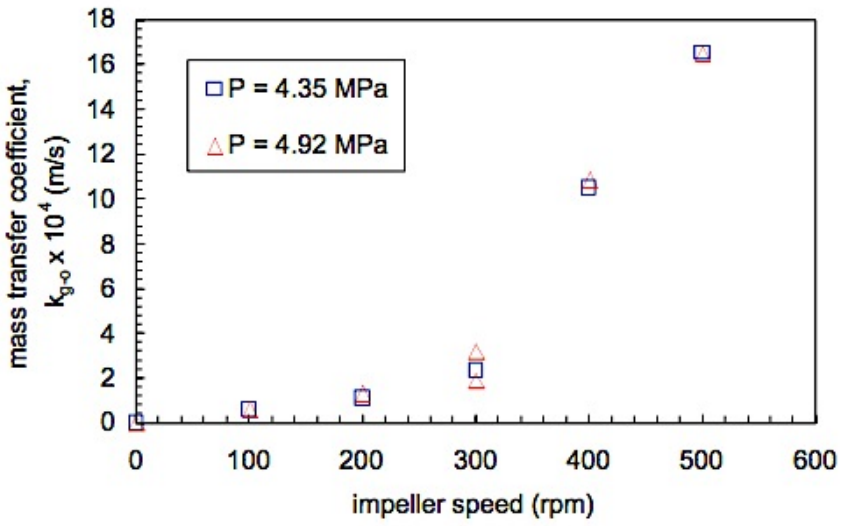


Figure 3.2: Mass transfer coefficient, k_{DG} from Turner's autoclave experiment (Turner, 2006)

3.4 Hydrate Formation Rate

Based on Lo (2011) and Turner et al. (2005), the dissolved gas consumption rate (hydrate formation rate) can be modelled as:

$$\dot{m}_H = u' k_{\mathrm{B}} A_{W-O} (\Delta T) f_Y$$
$$k_{\mathrm{B}} = k_1 e^{\left(\frac{k_2}{T}\right)} \tag{3.42}$$

where k_{B} is the adjustable intrinsic rate constants regressed from Vysniauskas and Bishnoi (1983) laboratory experimental data. For hydrate structure I, in the case of hydrate formation (positive sub-cooling, ΔT), $\ln k_1 = 41.1393$ and $k_2 = -13600K$, and for the case of hydrate dissociation (negative sub-cooling, ΔT), $\ln k_1 = 57.9898$

and k_2 = -16696K. A_{W-O} is the total contact surface area between the water phase and the oil phase, ΔT is sub-cooling (driving force) and defined as:

$$\Delta T = T_H^{eq} - T \tag{3.43}$$

where T_H^{eq} is the hydrate equilibrium temperature and T is the system temperature. Sub-cooling is the temperature difference between the hydrate equilibrium temperature and the temperature when hydrate first nucleates (Figure 3.3). According to Matthews et al. (2000), hydrates nucleate on average 3.61K below the hydrate equilibrium temperature (minimum sub-cooling before hydrates nucleate). f_Y is the dissolved gas factor so that when the dissolved gas is depleted the mass transfer ceases:

$$f_Y = \frac{f_{DG}}{f_{DG}^{eq}} \tag{3.44}$$

u' in Equation (3.42) is a fitted rate constant, which an adjustment to the reaction rate constants to account for the mass and heat transfer resistance for hydrate formation.

The main assumptions with this approach are that during hydrate formation, water droplets in the oil phase convert immediately to full size hydrate particles, and these particles form and exist only in the oil phase. From Equation (3.42), it can be seen that the formation rate depends on the total contact surface area (A_{W-O}), the system temperature (T), and the concentration of the dissolved gas in oil (f_{DG}). Therefore, the formation rate is expected to increase as the water phase disperses in the oil phase leading to an increase in the total contact surface

area. The formation rate is also expected to increases as the system temperature deviates further below the hydrate equilibrium temperature, as this increases the degree of subcooling. ΔT. Finally an increase of the formation rate is expected with the rise of the concentration of dissolved gas in oil.

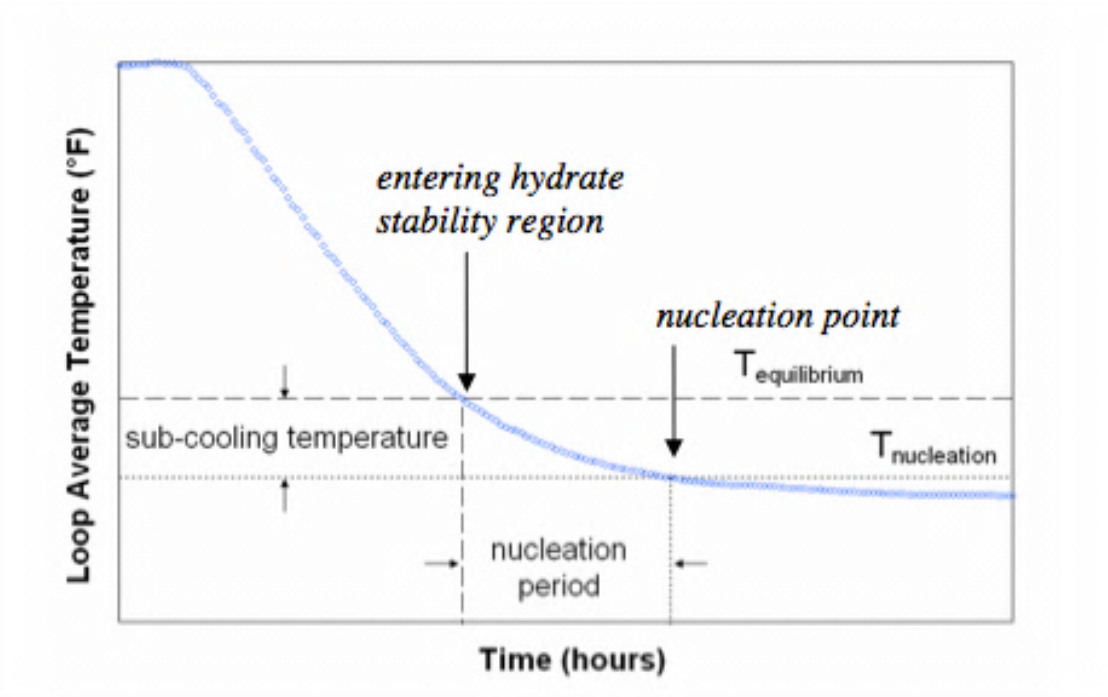


Figure 3.3: Subcooling temperature (Boxall, 2009).

3.5 Agglomeration of Hydrate Globules

The size of the aggregate can be calculated following the same method as CSMHyk (Turner et al., 2005; Boxall, 2009; Davies et al., 2009a) which is based on a steady-state balance between the inter-particle adhesion force and the fluid flow shear stress (Camargo et al., 2000):

$$\left(\frac{d_A}{d_P}\right)^{4-fr} - \frac{F_a\left[1-\frac{c_H}{c_{H_{max}}}\left(\frac{d_A}{d_P}\right)^{3-fr}\right]^2}{d_P^2\mu_0\dot{\gamma}\left[1-c_H\left(\frac{d_A}{d_P}\right)^{3-fr}\right]} = 0 \tag{3.45}$$

where d_A is the aggregate diameter, d_P is the hydrate particles diameter assumed to be $80\mu m$ based on experimental data by Turner (2006), c_H is the hydrate particles volume fraction in the liquid mixture (or 'hydrate cut'), $c_{H_{max}}$ is the maximum packing fraction assumed to be equal to 4/7 (the packing concentration of randomly packed spheres with the same diameter), fr is the fractal dimension that accounts for the porosity of the aggregate taken as 2.5, F_a is the normalized inter-particle adhesion force, a value that corresponds to capillary attraction between hydrate particles by a liquid bridge, μ_0 is the oil viscosity and $\dot{\gamma}$ is the shear rate.

One major assumption with this method is the hydrate particles agglomerate to a single aggregate with diameter d_A. Because of the strong non-linearity form of the equation, a root-finding algorithm is needed in finding the solution. The Newton-Raphson method is used for its speed to convergence. Due to the fractal nature of the aggregate, the effective volume fraction of the agglomerated hydrate globules can be calculated as:

$$c_{H_{eff}} = c_H\left(\frac{d_A}{d_P}\right)^{3-fr} \tag{3.46}$$

Finally, the relative viscosity of the hydrate slurry can be calculated from the modified Mills' equation (Mills as cited by Turner et al. (2005)):

$$\mu_{slurry} = \frac{1 - c_{H_{eff}}}{\left(1 - \frac{c_{H_{eff}}}{c_{H_{max}}}\right)^2} \tag{3.47}$$

The agglomeration of hydrate globules was used to calculate the effective viscosity of the hydrate liquid carrier, which in turn affects the friction factors, and consequently affects the momentum conservation equations. Plugging can be identified by a large viscosity increase accompanied by a large pressure drop in the system, which prohibits flow.

3.6 Numerical Implementation

The finite volume methodology is applied in the current model to generate the approximate numerical solutions to the governing equations. The system is divided into a finite number of adjacent control volumes where the governing equations are discretised and solved. To avoid the decoupling issues between pressure and velocity, a staggered mesh (Figure 3.4) is used. In scalar control volume, pressure values as well as the bulk properties of the phase, such as densities and phase fractions, are defined at the main nodes, while the velocities are stored at the volume boundary (midway between the scalar nodes) as can be seen from Figure 3.4(b).

A first-order fully-implicit scheme is used for the temporal integration due to its robustness and numerical stability, while a first-order upwind differencing scheme is used for the spatial derivatives as it provides boundedness of the

numerical solution. Despite being a first-order, the advantages of these schemes rationalise their choice.

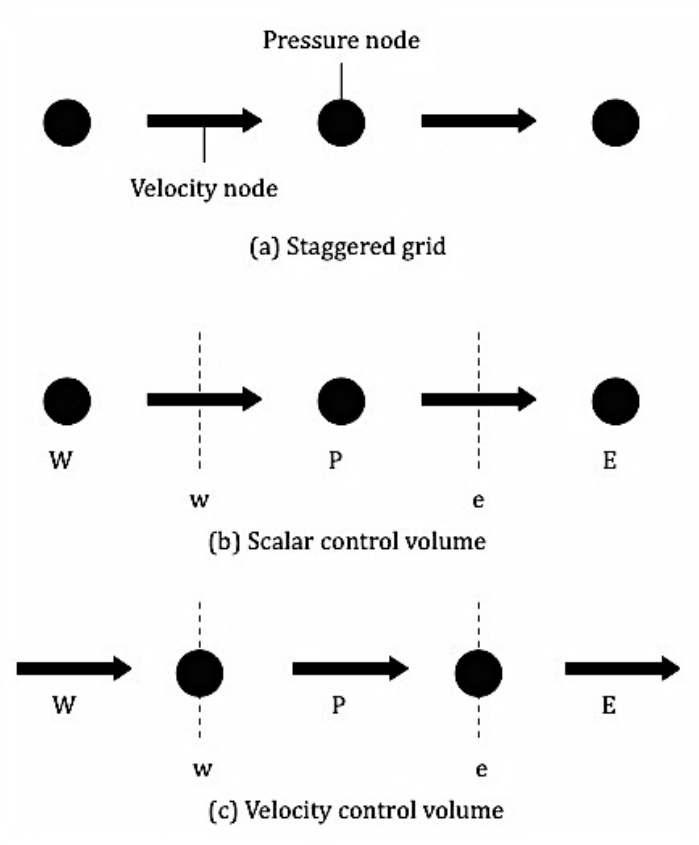


Figure 3.4: Staggered grid arrangement (Issa and Abrishami, 1986)

The current model solves for the liquid mixture and gas momentum equations (Equation 3.26 and Equation 3.25), the continuity equations for the gas (Equation 3.5), the water (Equation 3.7), the dissolved gas (Equation 3.9) and the hydrate fraction (Equation 3.10), as well as the pressure equation. The pressure equation is obtained by combining the solution of the momentum equations and the following overall, density weighted continuity equation:

$$\frac{1}{\rho_M^{ref}}\left(\frac{\partial}{\partial t}(\alpha_M\rho_M)+\frac{\partial}{\partial x}(\alpha_M\rho_M u_M)\right)+\frac{1}{\rho_G^{ref}}\left(\frac{\partial}{\partial t}(\alpha_G\rho_G)+\frac{\partial}{\partial x}(\alpha_G\rho_G u_G)\right) = \dot{m}_{DG}\left(\frac{1}{\rho_M^{ref}}-\frac{1}{\rho_G^{ref}}\right) \tag{3.48}$$

PISO (Pressure-Implicit with Splitting of Operators) algorithm (Issa and Abrishami, 1986) is implemented into the current model. This algorithm has been shown to be fast and efficient (Issa and Abrishami, 1986; Issa and Kempf, 2003). The steps of the solution algorithm are as follows:

1. The momentum equation for the gas and the mixture are solved implicitly to obtain u_G and u_M leading to the predicted values:

$$u_G^* = f(p)$$
$$u_M^* = f(p) \tag{3.49}$$

2. The predicted values, u_G^* and u_M^* are then used in Equation (3.48) to satisfy the overall continuity equation. The solution of this pressure equation is the corrected pressure, p^*.

3. The new pressure field, p^* can now be introduced in the momentum equations to correct the gas and the mixture velocities.

$$u_G^{**} = f(p^*, u_G^*, u_M^*)$$
$$u_M^{**} = f(p^*, u_G^*, u_M^*) \tag{3.50}$$

4. The newly predicted values, u_G^{**} and u_M^{**} are then introduced in the overall continuity equation (Equation 3.48). The solution to the second corrected pressure equation is the corrected pressure p^{**}.

5. The latest pressure field, p^{**} can now be introduced in the momentum equations to correct the gas and the mixture velocities for the last time with:

$$u_G^{***} = f(p^{**}, u_G^{**}, u_M^{**})$$
$$u_M^{***} = f(p^{**}, u_G^{**}, u_M^{**}) \tag{3.51}$$

This process is repeated in an iterative loop until convergence is achieved. The detailed solution algorithm can be found in Issa and Abrishami (1986) and Versteeg and Malalasekera (1995).

3.6.1 Boundary conditions

Properties such as total liquid hold-up and phasic velocities for each phases are prescribed at inlet of the pipe to match experimental conditions in the actual modelling. These values will be kept constant throughout the simulation. It is also possible to keep the mass flow rates for each phase constant at the inlet.

A zero gradient is assumed at the outlet for the phase fraction and the liquid mixture velocity (provided it is a positive). In case of a negative liquid mixture velocity, the velocity is changed to zero since liquid cannot re-enter at the outlet. Pressure is fixed at the outlet, generally set to atmosphere pressure or to

match the experimental value. From the pressure, the gas density is obtained and subsequently, the gas velocity by continuity consideration in the last cell.

3.6.1.1 Flow-loop boundary condition

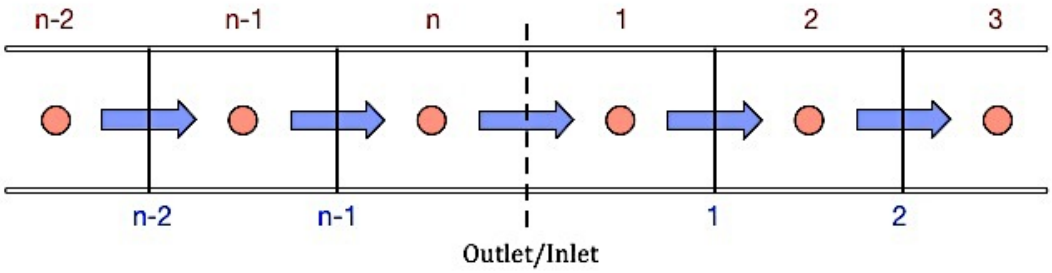


Figure 3.5: Periodic boundary condition to imitate the displacement pump in flow loops.

Most experiments on hydrates are performed in flow-loops to imitate the flowing conditions of offshore transport lines. In flow-loops, a multiphase pump circulates the fluids, and to mathematically simulate this, a periodic boundary condition is applied to the current model. This can be achieved by equating the value of each variable at the nodes just upstream and downstream of the inlet plane to the nodal values just upstream and downstream of the outlet plane (Versteeg and Malalasekera, 1995) as depicted by Figure 3.5. This method therefore, imitates the displacements of a pump in flow-loops.

3.6.2 Integration of the hydrate kinetics routine into TRIOMPH

All the governing equations, once discretised over the whole domain are solved in a sequential iterative manner. At each time step, the set of equations are solved

iteratively until a converged solution is obtained to a reasonable tolerance. Figure 3.7 gives a flow-chart of the sequence. The hydrate kinetics routine is divided into two main modules: dissolved gas and hydrate formation (Figure 3.6). The dissolved gas module will determine if the gas is permitted to dissolve in the oil phase and evaluate the 'dissolved gas fraction' in the oil phase based on its saturation value. This information is then passed to the hydrate formation module, which will then use it to obtain the amount of hydrates formed if the conditions are met (in this case, positive subcooling). If hydrates are formed, the hydrate module will also calculate the effective volume fraction of the agglomerated hydrate globules and subsequently the relative viscosity of the hydrate slurry. The hydrate kinetics routine will then feed the properties of the dissolved gas and hydrate back into TRIOMPH for the evaluation of the next time step.

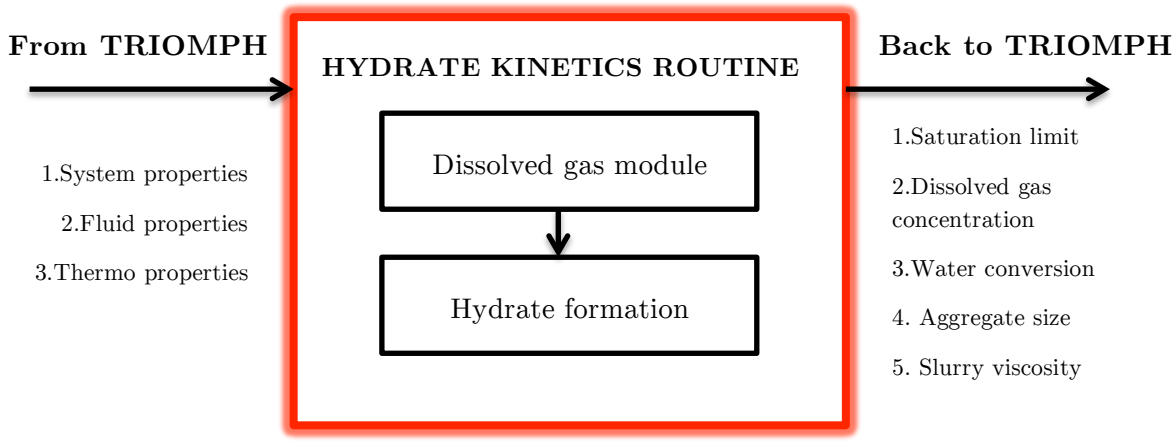


Figure 3.6: Integration of the hydrate kinetics routine into TRIOMPH.

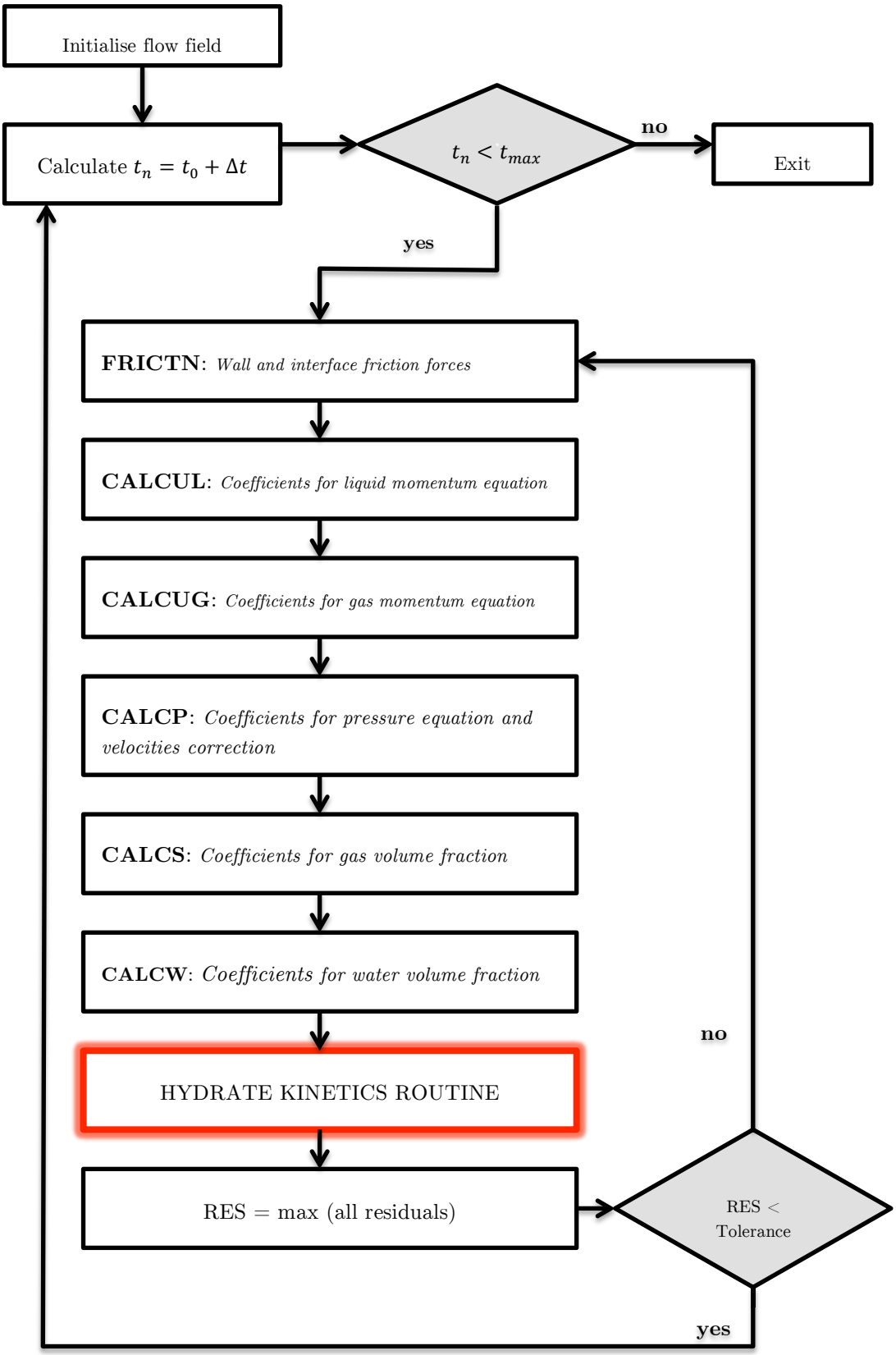


Figure 3.7: Flow chart of the solution algorithm in TRIOMPH

4 MODEL VALIDATION

4.1 Preamble

The present chapter validates the hydrate kinetics routine that was implemented into the TRIOMPH code. The first two sections give the results on the parametric tests and analyses to verify the correctness of the model implementation. Section 4.2 focuses on the implementation of the energy equation while section 4.3 analyses the integration of the hydrate formation routine. The results are compared with the general theory.

Section 4.4 focuses on the validation of the current model against two available flow loop experiments performed by the team at the Centre of Hydrate Research, Colorado School of Mines. Section 4.4.1 concentrates on the ExxonMobil flow loop, in which the description of the flow loop and the experimental procedure are found in section 4.4.1.1. The necessary flow loop modelling setup before the simulations are performed is described in Section 4.4.1.2. The simulation results are compared with the experimental data and the CSMHyK program, and discussed in section 4.4.1.3.

The second flow loop used for the model validation is the University of Tulsa flow loop. The description and the modelling approach of the flow loop are given in section 4.4.2.1 and section 4.4.2.2 respectively. The simulation results, with a comparison against the experimental data and CSMHyK are given in section 4.4.2.3.

Finally, section 4.5 focuses on the main contribution of the current model, which is its capability to predict hydrate formation in the slug body region. To verify this, two identical hypothetical pipes are used, one of the pipes is simulated by the current model while the other is simulated by the CSMHyK model (this is not the actual CSMHyK program, but rather the method used in CSMHyK that was also implemented into TRIOMPH). The results from the two models are compared and discussed.

4.2 Parametric Analyses for the Energy Equation

Once the energy equation has been implemented into TRIOMPH, the code has to be validated and analysed with simple parametric tests. For the $36m$-pipe three-phase flow test, the parameters that are fixed for the analyses are listed below in Table 4.1:

Table 4.1: Input parameters used in the Energy equation analyses.

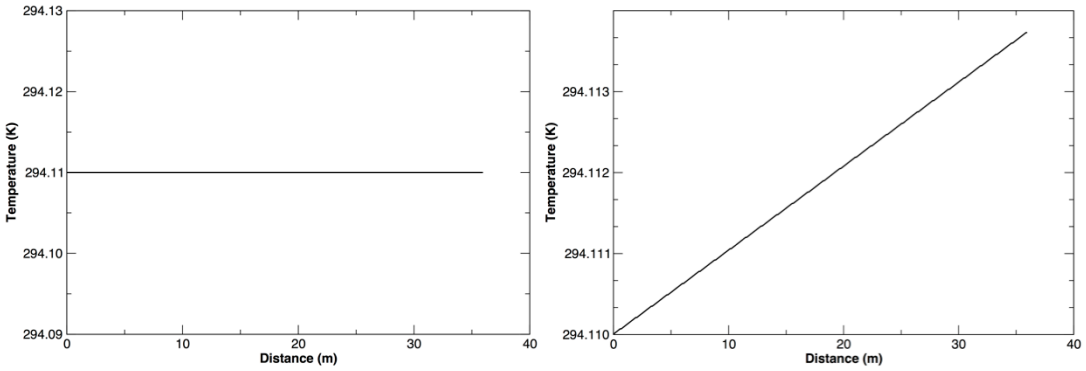
Input parameters	Water	Oil	Gas
Superficial velocity	0.24	0.24	1.20
Inlet hold-up	0.2	0.2	0.6
Density (kg/m^3)	999.130	860.000	1.293
Viscosity ($Pa.s$)	1.114×10^{-3}	10.000×10^{-3}	1.000×10^{-5}
Specific heat capacity ($J/kg.K$)	4181.3	2140.0	2892.0

Analysis 1: horizontal pipe, frictionless-adiabatic process

The analysis involved the omission of certain parameters. The analysis assumed there is no friction between the liquid phase and the wall, the gas phase and the wall and at the liquid-gas interface, hence the terms F_{wG}, F_{wM} and F_i in the right hand side of Equation (3.25) and Equation (3.26), as well as the term $(\tau_{wW}u_W + \tau_{wO}u_O + \tau_{wG}u_G)$ in Equation (3.38) are set to zero. Furthermore, since the pipe is in a horizontal configuration, the term $\alpha_G\rho_G g \sin\beta$ and $\alpha_M\rho_M g \sin\beta$ in the momentum equations will vanish. A further assumption is that there will be no heat transfer between the fluid within the pipe and the environment, so the term $(Q_W + Q_O + Q_G)$ in the Equation (3.38) is also zero. Therefore, based on conservation laws, the pressure and the temperature of the system should remain constant along the pipe. The result of Analysis 1 is shown below in Figure 4.1(a) and it can be observed that the temperature is constant for the whole pipe length, which is in agreement with the theory.

Analysis 2: horizontal pipe, isobaric with frictional heating process

This analysis is similar to Analysis 1, with the additional introduction of the frictional heating. The term $(\tau_{wW}u_W + \tau_{wO}u_O + \tau_{wG}u_G)$ in Equation (3.38) is no longer zero. Therefore there is a small increase in the temperature of the system due to the heat generated by the frictional forces. From Figure 4.1(b), it can be observed that the temperature increases by a small amount (0.0037 K).



(a) (b)

Figure 4.1: The temperature profile for (a) Analysis 1 (b) Analysis 2.

Analysis 3: horizontal pipe, non-isobaric process

Following Analysis 2, the pressure is now allowed to vary. Because of the shear stresses, the pressure will drop as it goes along the pipe and according to ideal gas law, pressure obeys a linear relationship with the temperature. From the Figure 4.2, it can be seen that both the pressure and the temperature decreases.

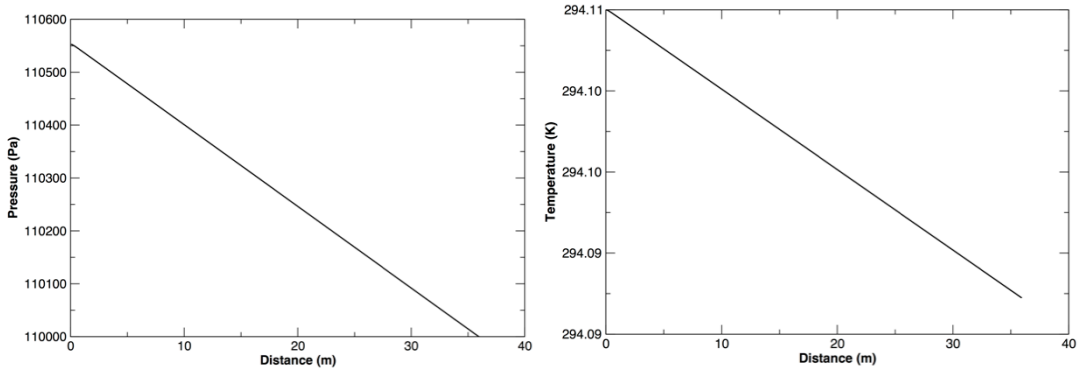


Figure 4.2: The pressure and temperature profile for Analysis 3.

Analysis 4: horizontal pipe, frictionless-non adiabatic process

The heat transfer term $(Q_W + Q_O + Q_G)$ in Equation (3.38) is now introduced into the system. However, the environment (surroundings) temperature, T_∞ is set equal to the system's temperature, T. Since heat transfer only occurs when there is a temperature difference (heat flows from high to the low temperature), the term $(Q_W + Q_O + Q_G)$ is equal to zero. This system is then reduced to an adiabatic process, therefore the pressure and temperature within the system should remain constant throughout the pipe's length. The result of this analysis, in Figure 4.3, shows an agreement with the theory.

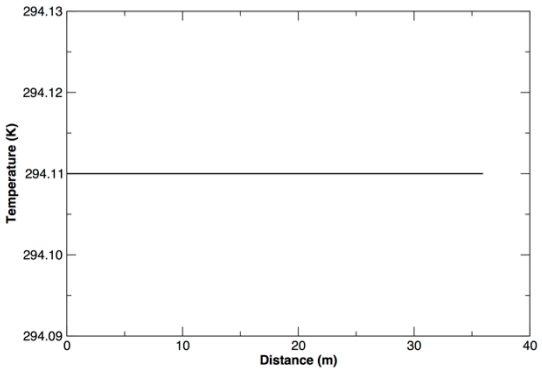


Figure 4.3: The temperature profile for analysis 4.

Analysis 5: vertical pipe, steady-state single-phase system, adiabatic

For a steady-state, single-phase flow in a vertical pipe, with no frictional heating and heat transfer, the Equation (3.38) reduces to the following:

$$\rho C_p \Delta T = \Delta P$$

hence, the temperature difference,

$$\Delta T = \frac{\Delta P}{\rho C_p}$$

where for a vertical pipe, $\Delta P = \rho g Z$, where Z denotes the height of the pipe, therefore the temperature difference between the inlet and the outlet is:

$$\Delta T = \frac{gZ}{C_p} \tag{4.1}$$

Consequently, an analytical solution can be obtained from Equation (4.1) and a comparison can be made between the numerical and analytical solutions. For a $36m$ vertical pipe with water as the flowing fluid, the numerical and analytical

solutions are given in the subsequent Table 4.2 and Figure 4.4 below. As expected, the temperature decreases as it leaves the pipe due to the pressure drop. The numerical solutions show a good agreement with the analytical solutions with less than 2% discrepancies.

Table 4.2: The analytical versus numerical solutions for test 5.

	Pressure drop, *Pa*	**Temperature difference, *K***
Analytical solutions	352 852.75	0.084461
Numerical solutions	351 612.50	0.083333
% error	0.35%	1.34%

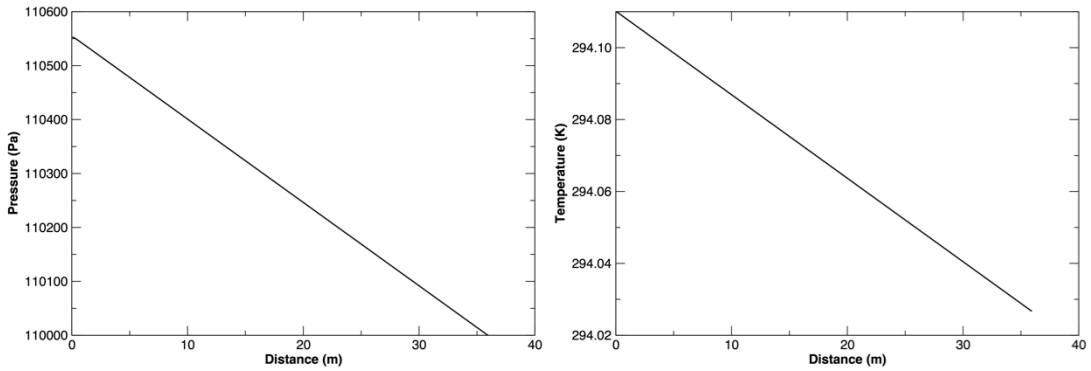


Figure 4.4: The pressure and temperature profile for Analysis 5.

4.3 Parametric Analyses for the Hydrate Kinetics Routine

Simple analyses were set up to test and verify the correctness of the hydrate kinetics model implementation. The three fluids chosen in the two analyses are water, light crude oil, and methane gas. In both cases, Henry's constant of

methane gas in oil, H_G is set to 1×10^9 Pa, the mass transfer coefficient for the dissolved gas, k_{DG} is 0.0011 m/s, the inlet liquid mixture holdup, $\alpha_{M\,@\mathrm{inlet}}$ is 0.548 and the outlet pressure is set to $5MPa$. The domain is a horizontal $100m$ long pipe, with a diameter of $0.1m$. Other constant parameters set in all the analyses are listed below in Table 4.3:

Table 4.3: Input parameters for hydrate kinetics rountine analyses.

Input parameters	Water	Oil	Gas
Superficial velocity	0.1117	0.2055	0.2617
Inlet hold-up	0.193	0.355	0.452
Density (kg/m^3)	999.23	837.99	1.30
Viscosity ($Pa.s$)	1.114×10^{-3}	5.000×10^{-3}	1.100×10^{-5}
Molecular weight (kg/mol)	18.02×10^{-3}	143.58×10^{-3}	16.04×10^{-3}

Analysis 1: The dissolved gas module

In most hydrate experimental work, the pipe is normally pressurized to its equilibrium condition before any tests are made. The present analysis involves mimicking that pressurized condition. The system temperature was set to be above the hydrate equilibrium temperature to avoid any hydrate formation. In theory, gas dissolves in the liquid until it reaches its saturation value/equilibrium condition in that particular liquid.

As can be observed from Figure 4.5, the gas dissolves in oil until it reaches its saturation value at about $30m$ from the inlet, and the mass transfer of gas into the oil stops when it reaches the equilibrium value. The result agrees with the theory.

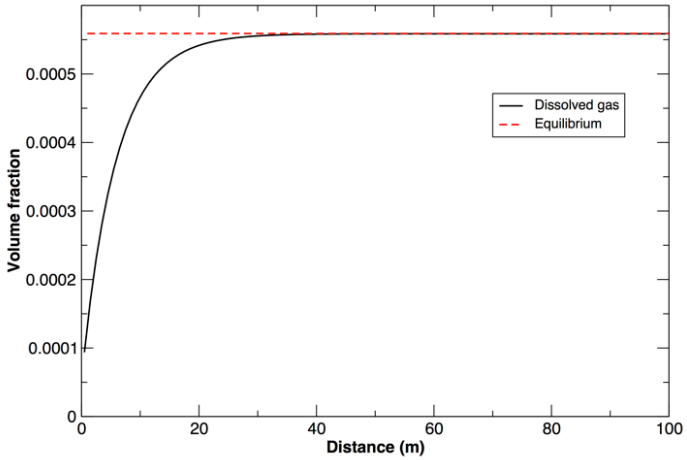


Figure 4.5: The dissolved gas module analysis.

Analysis 2: The hydrate formation module

Using the results from Analysis 1 as a starting condition, this analysis involves turning the dissolved gas module off and the hydrate module on. The temperature difference (subcooling) was set to be positive ($\Delta T = 2.44K$) to allow hydrate formation. In theory, the dissolved gas in oil is depleted during the hydrate formation process and since the dissolved gas module is turned off, $\dot{m}_{DG}$ is zero, Equation (3.9) now becomes:

$$\frac{\partial}{\partial t}(f_{DG}\alpha_O\rho_O) + \frac{\partial}{\partial x}(f_{DG}\alpha_O\rho_O u_O) = -\dot{m}_H$$

From this equation, we can say that the initial value (equilibrium value obtained from Analysis 1) of the dissolved gas will be diminished as the hydrates form, which will eventually deplete to zero, and the hydrate formation will stop due to the depletion of the dissolved gas. Figure 4.6 shows agreement with the theory.

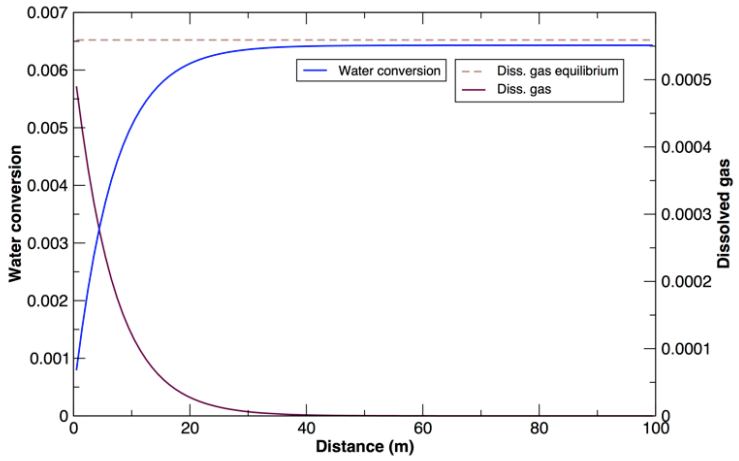


Figure 4.6: The hydrate module analysis.

4.4 Validation Against Experimental Data

4.4.1 ExxonMobil Flow loop

4.4.1.1 ExxonMobil flow loop experimental setup.

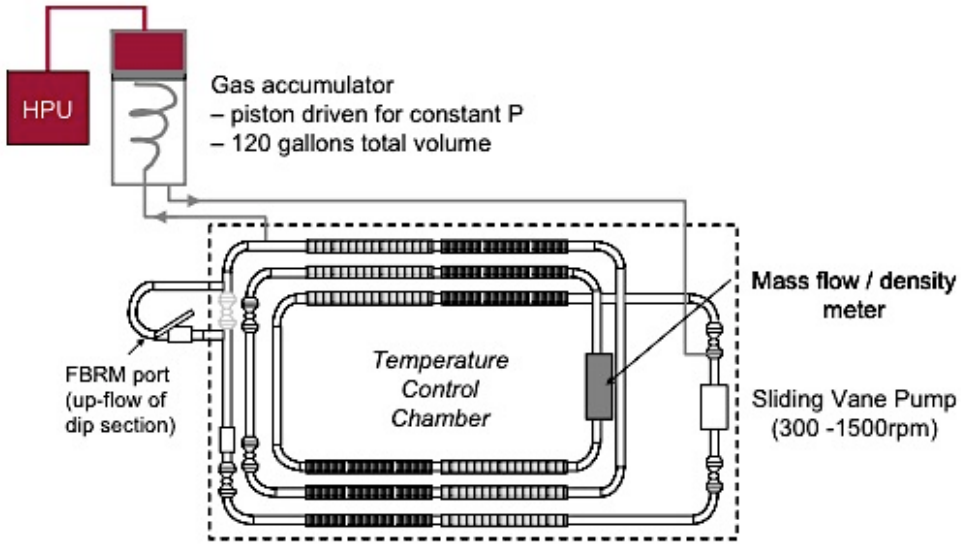


Figure 4.7: Schematic diagram of the ExxonMobil flow loop (Boxall, 2009)

The ExxonMobil flow loop is located in the ExxonMobil Friendswood facility in Texas. The flow loop is a triple pass loop with a total length of $95m$ (including the outside dip section) and $9.72cm$ of internal diameter (Figure 4.7). The loop total volume without the gas accumulator is approximately $705.8l$. The entire loop is contained in an indoor controlled environmental chamber except for the insulated dip section where a sight glass and a particle size analyser is installed. The fluids are circulated using a sliding vane pump so as to reduce the destructive impact on the hydrate particles. The pump is capable of operating at a range of $300RPM$ up to $1500RPM$.

The experiments were performed by charging the loop with liquid according to the predetermined phase fractions, and then pressurized with gas at experimental pressure. Once the fluids are in equilibrium, the loop is then cooled down, at cooling rates of approximately 2.22 K/h, to the experimental temperature (around $277.59K$). All the experiments were conducted at a constant pressure, therefore the gas consumed during hydrate formation was supplied back into the loop by the gas accumulator. The experiments were stopped when the hydrate formation was no longer significant (indicated by the unchanging gas accumulator volume).

A series of glycerol/water experiments were performed by Boxall (2009) to calibrate the pump. The pressure drop due to loop fittings were investigated and he came up with the flow equation for the ExxonMobil flow loop:

$$Q\left(\frac{Gal(US)}{min}\right) = 0.34085 \times \text{motor speed}(RPM) - 35.971 \tag{4.2}$$

or in the conventional form:

$$Q\left(\frac{m^3}{s}\right) = [(2.15\times10^{-5}) \times \text{motor speed}(RPM)] - 0.00227 \tag{4.3}$$

All the experiments in the ExxonMobil flow loop were performed using two oils, Conroe oil and a blend of Conroe and Brightstock oil. Conroe oil with a specific gravity of 0.84 has a low asphaltene content ($0.31\,Wt\,\%$), while Brightstock oil (specific gravity 0.90) has no asphaltene content. Conroe oil was used as the low viscosity ($0.005 Pa.s$) oil while the blend of Conroe and Brightstock, of 50:50 volume mixture, was used as the high viscosity oil ($0.1 Pa.s$). The composition of the two oils are listed in the Appendix C. The gas used in the the experiments were pure methane (structure I hydrate former) and a mixture of methane and ethane (structure II hydrate former).

In total, 22 experiments with a combination of six experimental variables, (namely the water cut, gas phase fraction, pump speed, pressure, oil viscosity and composition of the hydrate former) were investigated by Turner (2006) and Boxall (2009). However, there are only five publicly available data to compare with the current model. The data are listed below in Table 4.4. The gas used in all the experiments listed below was pure methane.

Table 4.4: ExxonMobil flow loop experiments used for comparison with the current model.

	Pump speed (RPM)	**Water cut, c_W**	**Void fraction, α_G**	**Pressure, P (MPa)**	**Oil viscosity, μ_O ($Pa.s$)**
Run 1(a)	300 ($0.579 m/s$)	0.35	0.46	5.068	0.005
Run 11	300 ($0.579 m/s$)	0.35	0.46	6.550	0.005
Run 12	550 ($1.311 m/s$)	0.35	0.46	6.550	0.005
Run 15	300 ($0.579 m/s$)	0.35	0.46	5.068	0.100
Run 16	550 ($1.311 m/s$)	0.35	0.46	5.068	0.100

4.4.1.2 ExxonMobil flow loop modelling setup

Prior to all simulations, the ExxonMobil flow loop geometries (diameter and length) and the fluid properties (densities, viscosities etc.) were defined in the input file. The initial conditions for each experiment, such as the operating pressure and temperature, velocities and phase fraction were also required. Some parameters that are dependent on the pressure and temperature were required to be generated before the simulation: (1) the hydrate equilibrium temperature for a given operating pressure obtained based on the composition of the gas phase (2) a look-up table for the gas compressibility factor, z, for a range of temperature of interest (for a given operating pressure).

In simulating the ExxonMobil flow loop experiments, the time when hydrates first nucleate (nucleation time as depicted in Figure 4.8) was fixed to coincide with the experimental data. CSMHyK used the temperature profile obtained in the experiments as the input parameter in their simulation. Unfortunately, the present author had no access to these results, therefore the temperature profile for each experiment were estimated based on the Newton's law

of cooling. The three known parameters (for each experiments) were the two temperatures, the hydrate equilibrium temperature (*T2*) and the final operating temperature (*T3*) (in equilibrium with the ambient temperature), and the time at which hydrates first nucleate (*t-nucleation*) as depicted in Figure 4.9. The initial temperature (*T1*) was assumed to be at room temperature ($294.11K$). From *T2*, the hydrate nucleation temperature (*T2'*) can be obtained from the general assumptions that hydrates nucleate on average $3.61K$ below the hydrate equilibrium temperature (Matthews et al., 2000). In the experiments however, the subcooling temperature varies as reported by Boxall (2009). From Newton law of cooling:

$$\frac{dT}{dt} = k_c(T3 - T1) \tag{4.4}$$

with $T(0) = T1$ and $T(t, nucleation) = T2'$, one can deduce:

$$T(t) = T3 + (T1 - T3)exp^{-k_c t} \tag{4.5}$$

and k_c was found by minimising the difference between the observed (T2') and the calculated (Equation 4.5) using an Excel solver.

Figure 4.9 shows the result of the temperature prediction against the experimental data (only one temperature profile obtained from the appendices in Boxall (2009)) for Run 1(a). As shown, this method agrees well with the experiment.

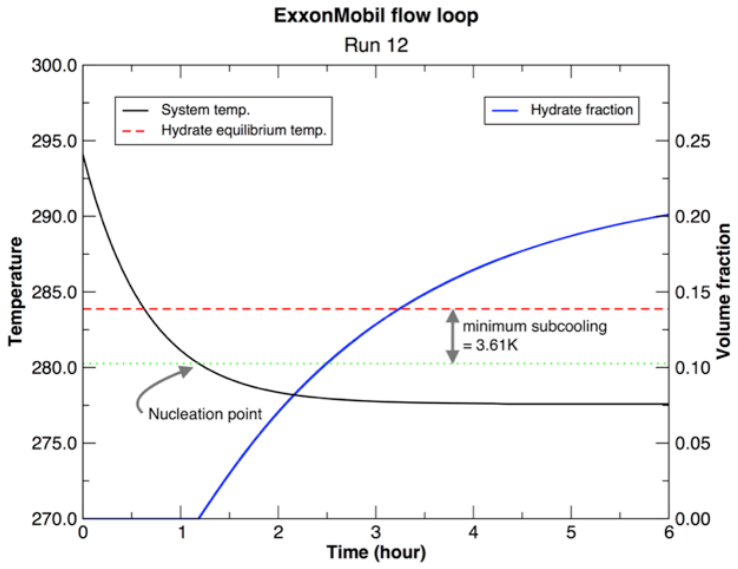


Figure 4.8: Nucleation point of hydrate formation.

The flow loop boundary condition as explained in Section 3.6.1.1 was applied to the current model. The constant pressure was achieved by keeping the superficial gas velocity and the void fraction at the inlet (to the initial value) constant. The simulation was performed in two stages: first, the loop was simulated at the operating pressure and at room temperature, allowing the oil to be saturated with gas. Next, using the restart file from the previous run as the input file, the loop was simulated, this time with the estimated temperature profile, allowing hydrate formation. Figure 4.10 shows the mesh sensitivity analysis on one of the test cases. Both coarse mesh (Δx_{coarse} =1.0m) and fine mesh (Δx_{fine} =0.0392m) gave the same converged solution (grid independence is achieved) therefore evidently, the hydrate formation prediction in the ExxonMobil

flow loop simulation did not require having a fine mesh. Therefore a coarse mesh was used in the simulation to reduce computational demand.

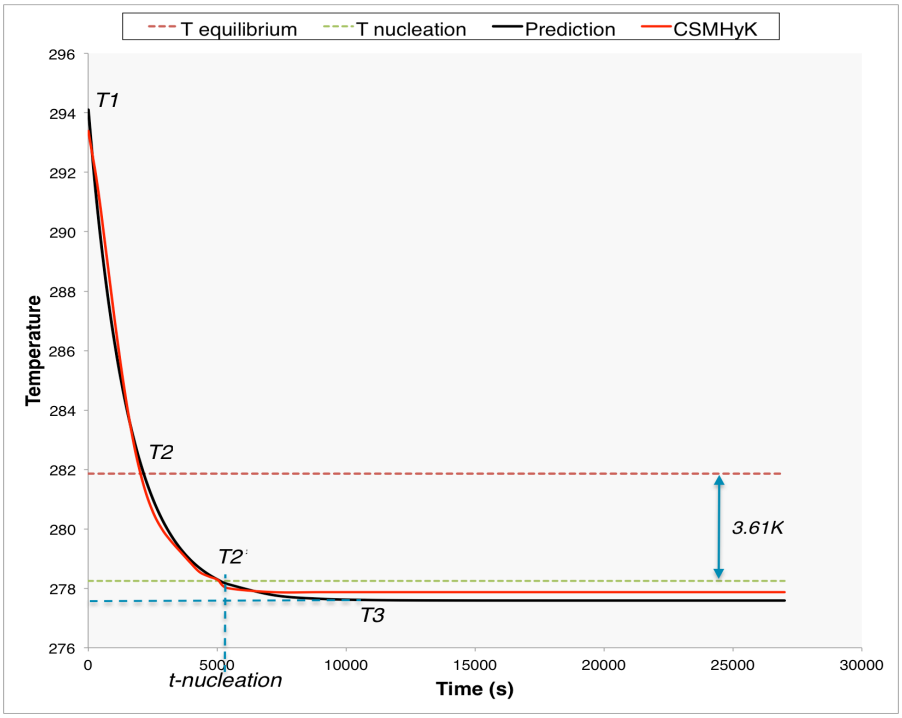


Figure 4.9: Example of temperature prediction to match the experimental nucleation period.

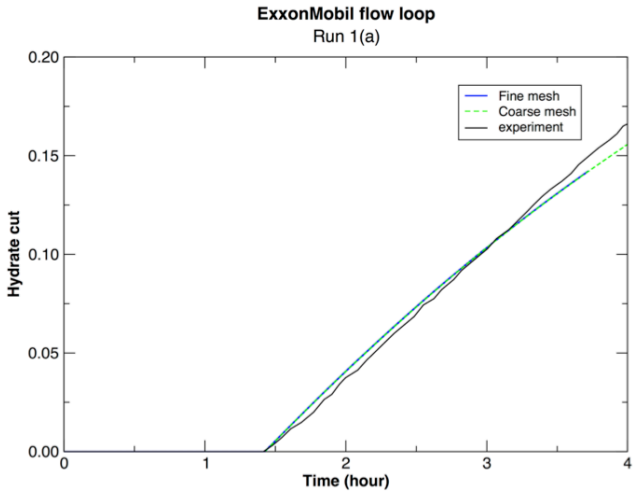


Figure 4.10: Mesh sensitivity analysis on Run 1(a) of the ExxonMobil experiments ($94m$ long, $9.72cm$ in diameter), coarse mesh (Δx_{coarse})=$1.0m$, fine mesh (Δx_{fine})=$0.0392m$.

4.4.1.3 Results and discussion

As previously mentioned in sections 2.3 and 3.4, the intrinsic formation rate constants require a modification to account for the mass and heat transfer resistance during hydrate formation. The fitted rate constant, u' in Equation (3.42) was obtained by fitting the simulated results to the experiments during the first hour after nucleation. Figure 4.11 shows the effect of the fitted rate constant, and clearly, without the fitted rate constant, the current model over predicted the hydrate formation rate in the ExxonMobil flow loop.

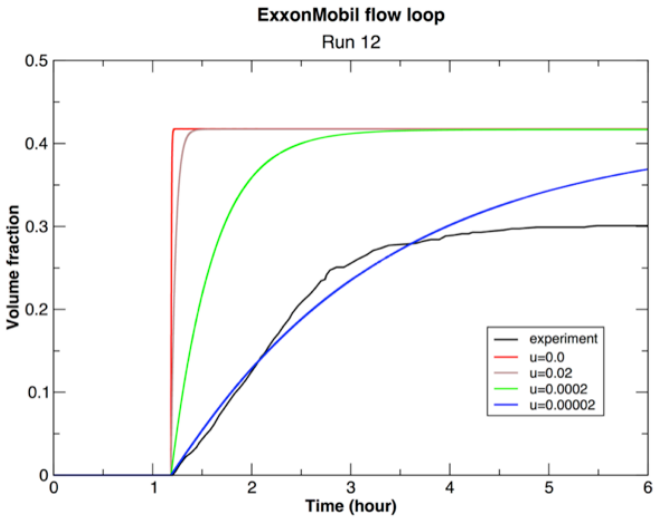


Figure 4.11: The effect of fitted rate constant, u' on hydrate formation

In his CSMHyK-OLGA® simulation, Boxall (2009) showed that the large variation (varied in two orders of magnitude) in the fitted rate constant u' was due to the inaccuracy in calculating the surface area for hydrate formation, A_{W-O}. Direct use of the surface area calculated in OLGA® produced big variations in the fitted rate constant. This is because OLGA® ignored the formation of the

dispersions due to the pump mixing and the bends and elbows in the loop. This variation was reduced by assuming that the water was fully dispersed in the oil, with a log-normal distributions (mean droplet 40 μm).

In a similar manner, TRIOMPH predicted stratified flow for the flow conditions listed in Table 4.4, due to the lack of the capability to predict dispersions caused by the mixing of the multiphase pump. Therefore, the total surface area calculated in CSMHyK, were used as an input to the simulations of the present model. The same surface area in CSMHyK was obtained by the current model with an assumption that the water is fully dispersed in the oil with uniform water droplets diameter of 80μm. The following figures show the results of the simulation of the ExxonMobil flow loop.

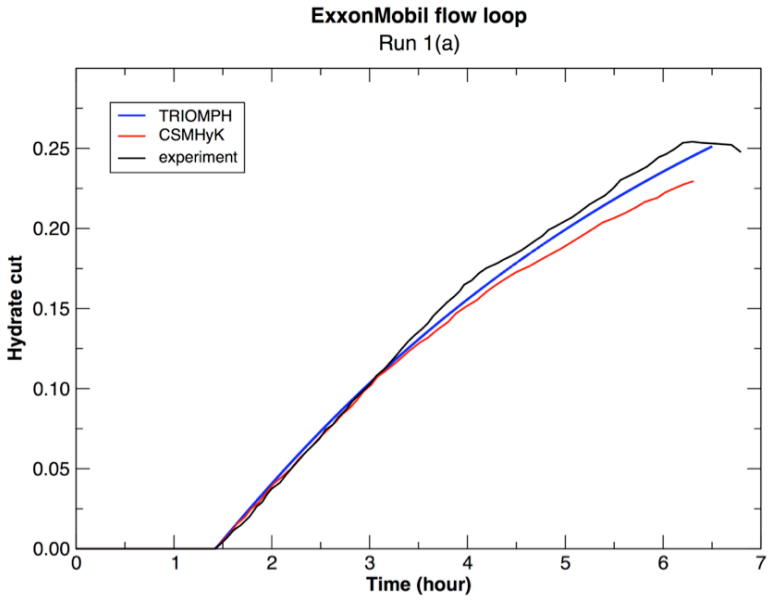
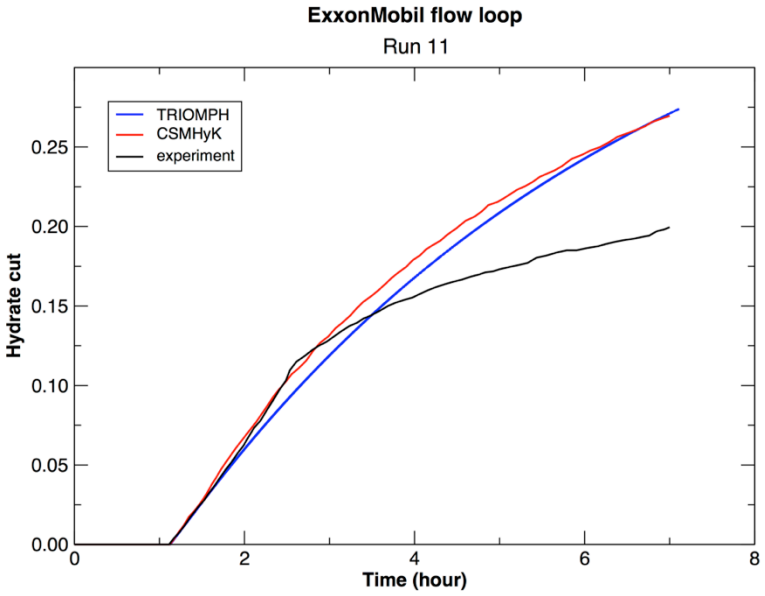
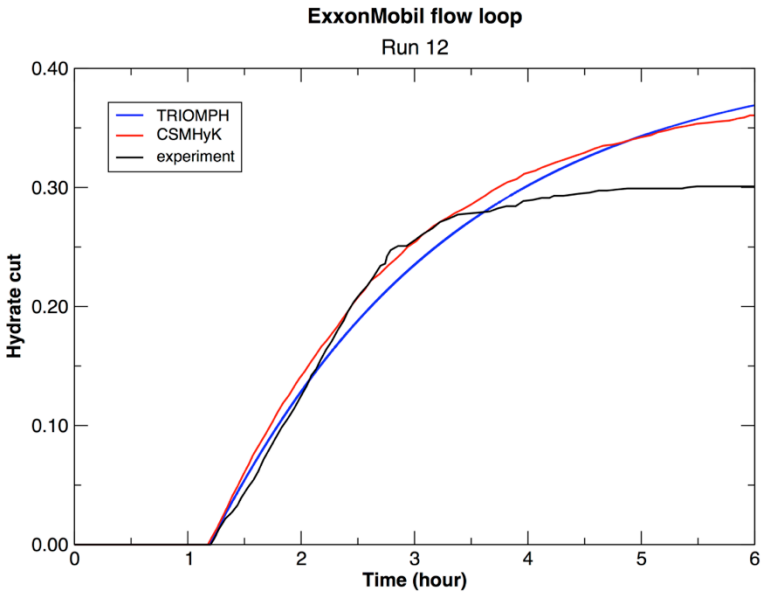


Figure 4.12: The experiment where hydrate formation is well predicted. u'=0.0000216, Pump speed: 300RPM, pressure: 5.068MPa, oil viscosity: 0.0005 $Pa.s$

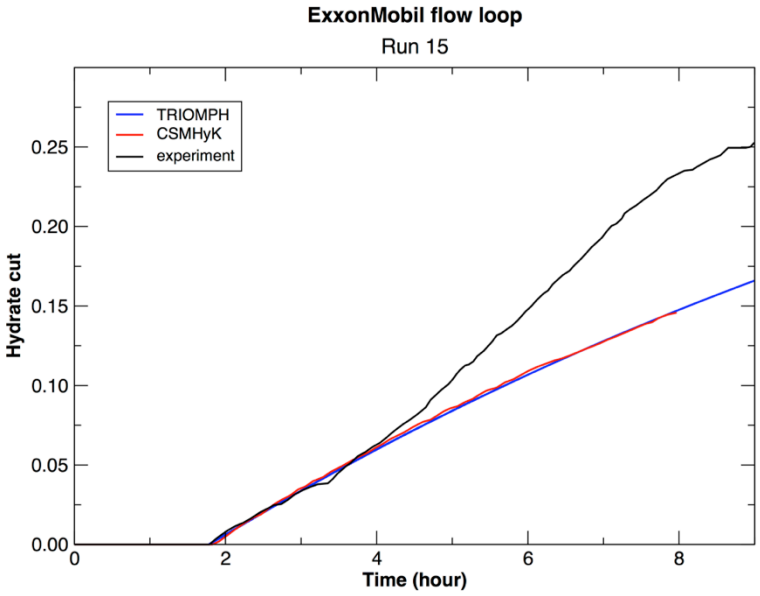


(a)

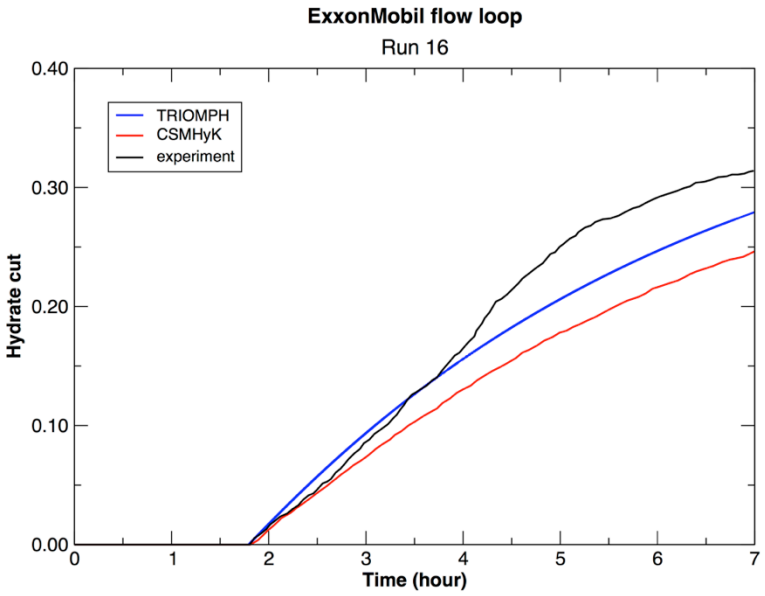


(b)

Figure 4.13: Experiments where hydrate formation are over predicted. (a) u'=0.0000171, Pump speed: 300RPM, pressure: 6.55MPa, oil viscosity: 0.0005 $Pa.s$ (b) u'=0.0000387, Pump speed: 550RPM, pressure: 6.55MPa, oil viscosity: 0.0005 $Pa.s$



(a)



(b)

Figure 4.14: Experiments where hydrate formation are over predicted (a) u'=0.0000091, Pump speed: 300RPM, pressure: 5.068MPa, oil viscosity: 0.1 $Pa.s$ (b) u'=0.0000236, Pump speed: 550RPM, pressure: 5.068MPa, oil viscosity: 0.1 $Pa.s$

On average, the intrinsic formation rate constants regressed from the Vysniauskas and Bishnoi (1983) experimental data were required to be reduced by a factor of 0.00002; this is thought to be what is required to account for the heat and mass transfer resistance during hydrate formation. Run 1(a) agrees well with the experiment, while the other four simulations either over predicted (Run 11 and Run 12) or under predicted (Run 15 and Run 16) the final formation rate. However, all experiments showed a similar pattern to the results obtained by CSMHyK. This showed that the current model is comparable with the method used by CSMHyK.

Both simulations with the high pressure over predicted the final formation rate. In the current model, the concentration of dissolved gas in oil increases with pressure, hence a rise in the concentration will increase the mass transfer of the dissolved gas into the water, producing more hydrates. Additionally, in the experiment, the cooling rate of the flow loop was not uniform and it was reported that the pressure has an effect on the cooling rate (Boxall, 2009), subsequently has an effect on the degree of subcooling. In the simulation, the subcooling was set to be a constant value of $3.61K$. Furthermore, the discrepancies in the final formation rate is probably also due to the calculation of the surface area in the current model, which assumes a constant water droplet size.

Both simulations with the high viscosity ($0.1Pa.s$) under predicted the final formation rate possibly again due to the incorrect surface area prediction. Turner (2006) and Boxall (2009) showed that an increase in oil viscosity resulted in the

smaller water droplet diameter, which in turn, produced higher surface area for hydrate formation. In the current model, a uniform water droplet diameter was assumed. This could explain the discrepancies in the prediction of the final formation rate.

The results of the simulation for the ExxonMobil flow loop shown above suggest that a more physical behaviour during the hydrate formation, such as the heat and mass transfer limitations, should be incorporated into the current model. Moreover, improved prediction of the water droplets size distribution in oil is essential in predicting the hydrate formation rate. In this manner, the need to reduce the formation rate constant can be avoided.

4.4.2 University of Tulsa Flow loop

4.4.2.1 Description of the University of Tulsa flow loop

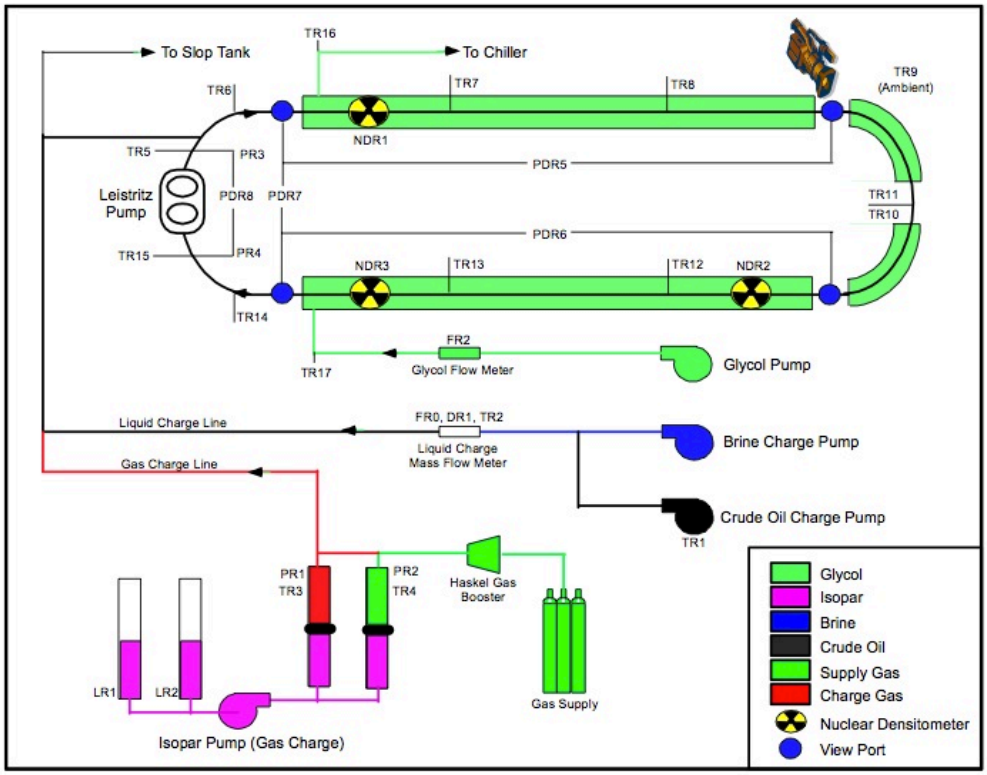


Figure 4.15: Schemetic diagram of the University of Tulsa flow loop [Dellecase et al. (2008) as cited by Boxall (2009)].

The University of Tulsa flow loop (located in Oklahoma) has an internal diameter of $7.37cm$ and a total axial length of $50m$ (Figure 4.15). A cooling jacket over the loop, with glycol as the coolant fluid, controls the temperature of the fluids inside the loop. A Leistritz twin-screw multiphase pump circulates the fluids and is 8capable of operating up to $2000RPM$. The loop is equipped with four viewports, at the end of each section. The experiments in the university of Tulsa flow loop can be performed in either constant volume or constant pressure mode. In constant

volume experiments, hydrate formation results in the decrease of the loop pressure due to the changes in the gas volume (gas consumed during hydrate formation), while in the constant pressure experiments, pressure is maintained by adding the gas into the loop during the hydrate formation. However, only experiments conducted at constant pressure are considered in this thesis.

The experimental procedure for hydrate formation (in constant pressure mode) in the University of Tulsa flow loop is similar to the ExxonMobil flow loop. The liquids (water and oil) are charged into the loop with a predetermined phase fraction, and subsequently pressurized with gas at room temperature. Once the liquids are saturated with gas, the temperature of the loop is decreased to the experimental temperature (between $278K$ and $279K$). The mass of gas addition (to maintain a constant pressure) during hydrate formation is calculated using equations of state and the gas composition. The flow equation for the University of Tulsa flow loop is (Boxall, 2009):

$$Q\left(\frac{Gal(US)}{min}\right) = 0.135 \times \text{motor speed}(RPM) - 6.40 \tag{4.6}$$

or in the conventional form:

$$Q\left(\frac{m^3}{s}\right) = [(8.52\times10^{-6}) \times \text{motor speed}(RPM)] - (4.04\times10^{-4}) \tag{4.7}$$

All experiments in the University of Tulsa flow loop were performed using the city gas, and the oils used in the constant pressure experiments were crude oils (Caratinga and Buttermilk) and model oils (Citgo 19 and Citgo 20). Details on the properties and chemical composition of the oils and city gas can be found in the Appendix C. Table 4.5 lists the experiments used for comparison with the current model. All experiments were performed at a constant pressure of $13.79 MPa$.

Table 4.5: University of Tulsa flow loop experiments used for comparison with the current model.

	Pump speed (RPM)	**Water cut, c_W**	**Void fraction, α_G**	**Cooling rate (K/hr)**	**Crude oil**
CA-750-25	750 ($1.404 m/s$)	0.250	0.5	2.778	Caratinga
BU-750-25	750 ($1.404 m/s$)	0.250	0.5	2.778	Buttermilk
CI19-750-25-50	750 ($1.404 m/s$)	0.250	0.5	2.778	Citgo19
CI19-750-12.5-50	750 ($1.404 m/s$)	0.125	0.5	2.778	Citgo19
CI19-1250-12.5-50	1250 ($2.404 m/s$)	0.125	0.5	2.778	Citgo19
CI19-750-25-80	750 ($1.404 m/s$)	0.250	0.2	2.778	Citgo19

For more details on the University of Tulsa flow loop, please refer to Dellecase et al. (2008).

4.4.2.2 University of Tulsa flow loop simulation setup

The modelling setup for the University of Tulsa flow loop followed the same approach as the ExxonMobil flow loop, with a few differences. Again, the volume flow rate (superficial velocity) of the gas phase was kept constant to the initial value at the inlet plane. The mass of gas addition to the flow loop, was then calculated from the difference in the mass flow rate between the inlet and the outlet, at every time step, Δt:

$$\sum m_{G,added} = \sum \rfloor (\alpha_G \rho_G u_G A)_{@inlet} - (\alpha_G \rho_G u_G A)_{@outlet} \rfloor \Delta t \quad (4.8)$$

The hydrate nucleation time was fixed to coincide with the experiments. The method used in predicting the temperature profile in the ExxonMobil flow loop was also implemented. The average value of the fitted rate constant, u' (0.00002) attained from the ExxonMobil flow loop simulation was used in the simulation, with the assumptions of full dispersion of water-in-oil with 80 μm water droplets diameter.

4.4.2.3 Results and discussion

The following figures show the prediction of the current model of the total gas addition into the University of Tulsa flow loop. The gas addition during the first few hours is due to contraction of the gas phase during cooling of the loop, therefore gas was added to maintain a constant pressure. During this period, no hydrates were formed. Hydrate formation starts when there is a sudden discontinuity in the slope of the gas addition curve, where the rate of gas addition increases due to the gas consumption.

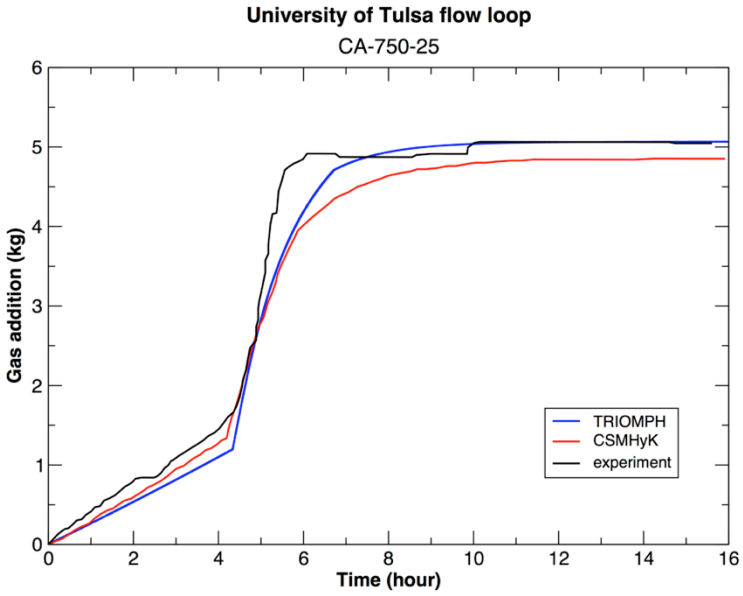


Figure 4.16: Plot of gas addition. Caratinga oil, pump speed=750RPM, liquid loading=0.5, water cut=0.25.

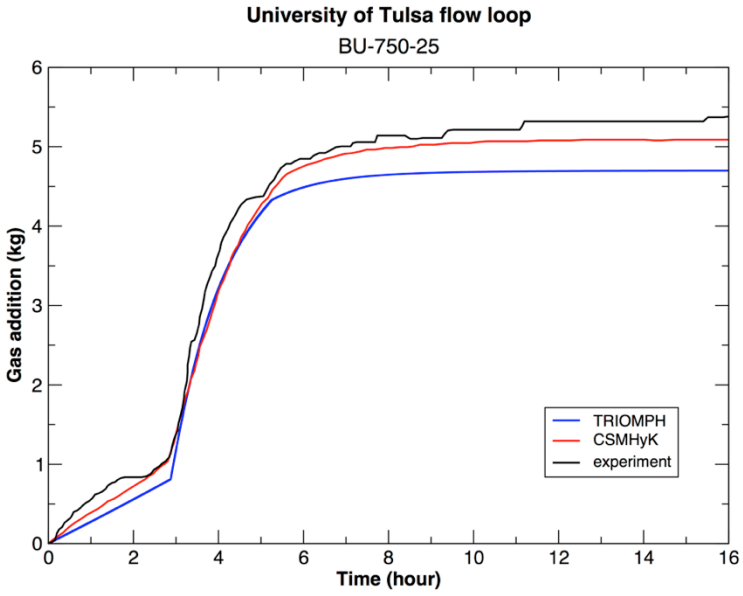


Figure 4.17: Plot of gas addition. Buttermilk oil, pump speed=750RPM, liquid loading=0.5, water cut=0.25.

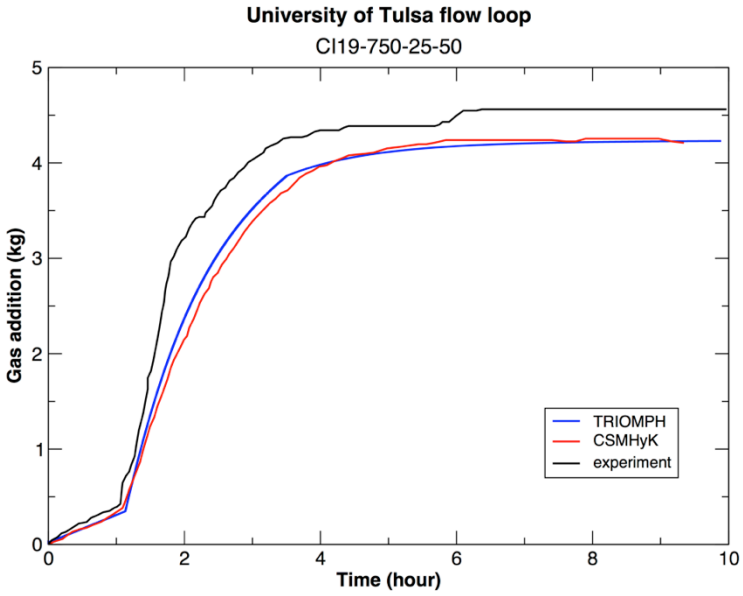


Figure 4.18: Plot of gas addition. Citgo19 oil, pump speed=750RPM, liquid loading=0.5, water cut=0.25.

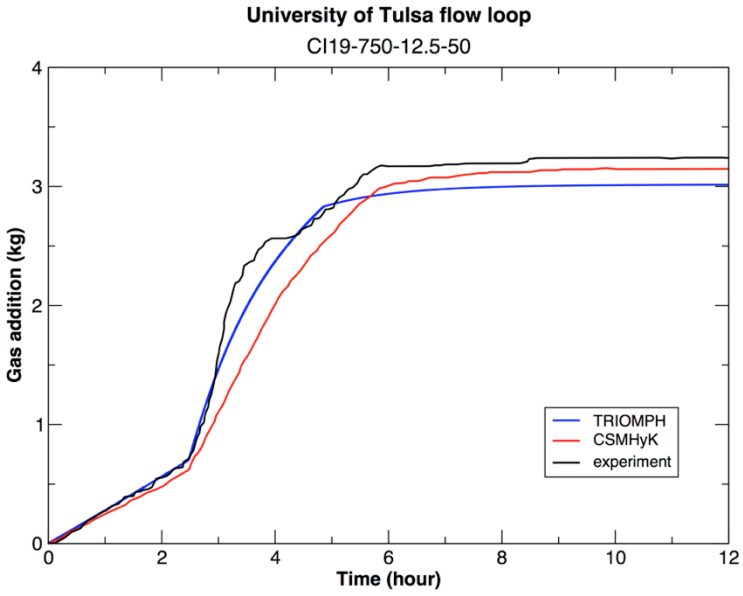


Figure 4.19: Plot of gas addition. Citgo19 oil, pump speed=750RPM, liquid loading=0.5, water cut=0.125.

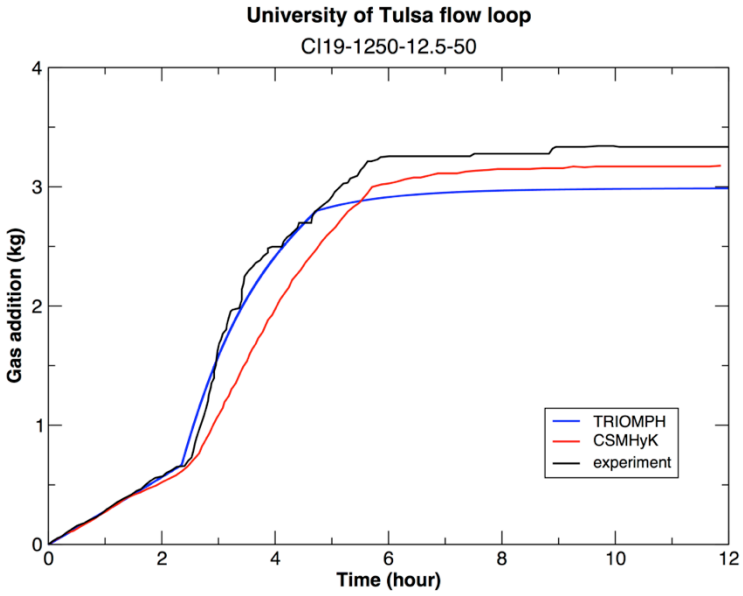


Figure 4.20: Plot of gas addition. Citgo19 oil, pump speed=1250RPM, liquid loading=0.5, water cut=0.125.

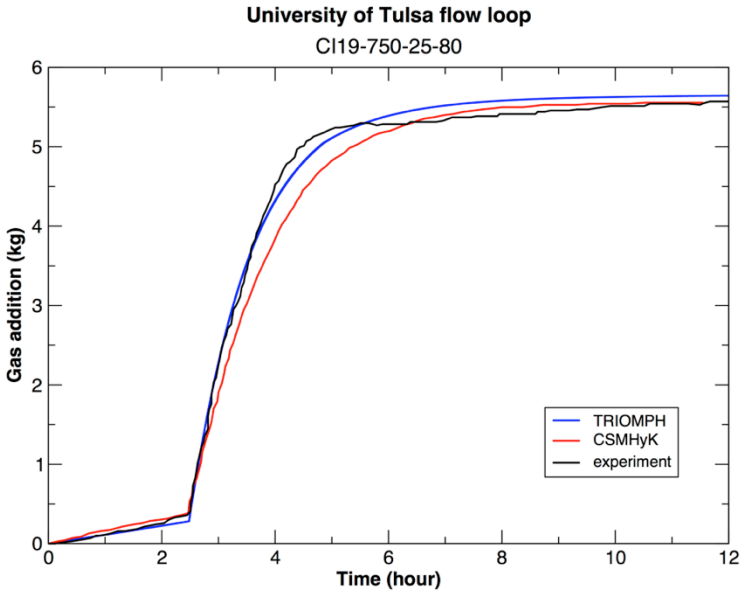


Figure 4.21: Plot of gas addition. Citgo19 oil, pump speed=750RPM, liquid loading=0.8, water cut=0.25.

As shown in the figures, the current model generally compares well with the experiments conducted in the University of Tulsa flow loop. The average value of the fitted rate constant, u' (0.00002) found in the ExxonMobil flow loop managed to predict the gas addition during the hydrate formation, for three different oils. In all experiments, all the water was fully converted into hydrates, represented by the unchanging value of the gas addition. The simulated plot of various phase fractions for one of the experiments is shown below in Figure 4.22.

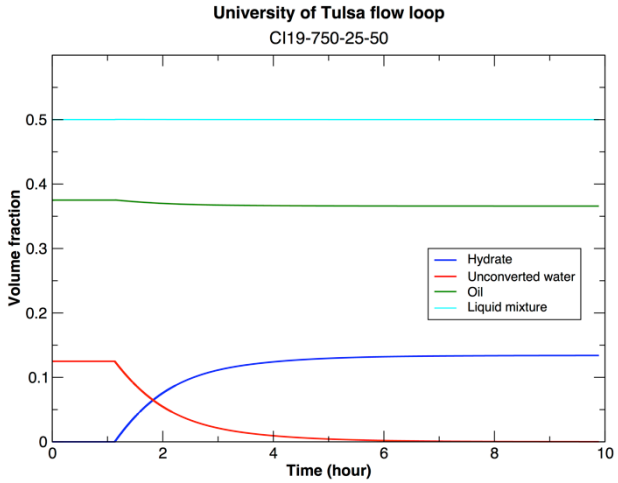


Figure 4.22: The plot of various phase fractions for one of the University of Tulsa flow loop experiments.

As with the ExxonMobil flow loop, some experiments compare better than the others. The inconsistencies in the gas addition during the cooling period may be due to the experimental uncertainty in the reported liquid loading (Boxall, 2009). For example, if the liquid loading in the simulation were slightly higher than the experiments, the smaller gas volume in the loop required less gas addition

to maintain a constant pressure during cooling. Another reason was possibly that the oil in the University of Tulsa flow loop was not properly saturated before the experiments hence required more gas addition into the loop to reach equilibrium. This is shown in Figure 4.16, Figure 4.17 and Figure 4.18, where the gas addition prior to hydrate formation was under predicted compared to the experiments.

The small discrepancies in the simulated results against the experiments, were due to a number of reasons; for instance, the manner in which the total surface area of water droplets was calculated. A full dispersion of water-in-oil was assumed in the current model for all experiments, with uniform water droplets diameter of $80\,\mu m$. In the experiments however, the size of the water droplets may vary considerably, depending on various parameters (the pump speed, the oil viscosity and the water-oil surface tension). For example, in a higher pump rate, the high shear rate may produce smaller water droplets, which in turn increases the total surface area for hydrate formation and subsequently the formation rate.

Moreover, the differences between the simulated results and the experiments could be due to the dynamic behaviour of the hydrate equilibrium temperature, by the changing in the composition of the city gas. Hydrates preferentially encapsulate heavier molecules such as propane (Sloan and Koh, 2007). Hence, as the heavier guest molecules deplete during hydrate formation, the composition of the city gas changes (with higher concentration of methane gas). This change in the composition results in the different hydrate equilibrium temperature, and consequently the formation rate.

4.5 Hypothetical Pipe

Turner et al. (2009) performed a study on hydrate formation in an autoclave reactor between Conroe oil, methane gas, and water. They found that the concentration of dissolved methane in Conroe oil was essentially constant (Figure 4.23). The dissolved gas consumed to form hydrates was replenished rapidly from the free gas phase. This suggests that the mass transfer across the diffusive gas-oil interface is not important and the diffusive hydrate shell on water droplets limits the hydrate growth. Possibly based on this observation, CSMHyK uses the free gas phase as an instantaneous source for the hydrate former, hence simplifying their formation model. This is a justifiable assumption for a system with the free gas continuously available. However, for a system that is heavily slugged, this method may be invalid. The present method does account for the finite-time dissolution of gas and the case considered here is chosen to demonstrate the need for such model.

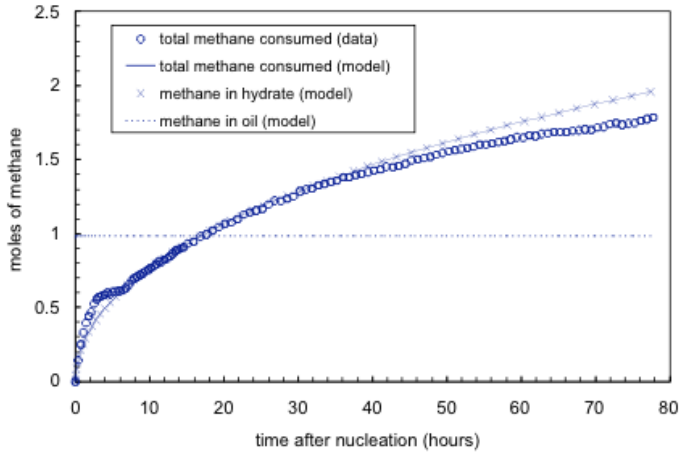


Figure 4.23: A result from an autoclave experiments performed by Turner (2006).

To verify this, two identical hypothetical pipes of $1km$ long, with an internal diameter of $9.72cm$ were used. The fluids used in the investigation were Conroe oil, methane gas, and water. The input parameters used in the test are listed in Table 4.6. The current model simulated one of the pipes, where the other was simulated by the CSMHyK method for comparison. Unfortunately, the present author had no access to the actual CSMHyK program; hence, the CSMHyK method was implemented into TRIOMPH.

Table 4.6: Input parameters for the test case.

Input parameters	**Value**	**Unit**
Void fraction	0.11	-
Gas superficial velocity	0.1442	-
Oil superficial velocity	0.7584	-
Water superficial velocity	0.4084	-
Pressure	5.17	MPa
Temperature	294.11	K
Oil density	837.99	kg/m^3
Oil viscosity	0.005	$Pa{\cdot}s$

In order to implement the method used in the CSMHyK into the TRIOMPH code, some modifications to the gas and liquid mixture continuity equations in Section 3.2 were needed. The continuity equations for the gas and the liquid mixture phase in Equation (3.5) and Equation (3.6) respectively becomes:

- The gas continuity equation:

$$\frac{\partial}{\partial t}(\alpha_G \rho_G) + \frac{\partial}{\partial x}(\alpha_G \rho_G u_G) = -\dot{m}_H \tag{4.9}$$

- The liquid mixture (oil, water, hydrate) continuity equation:

$$\frac{\partial}{\partial t}(\alpha_M \rho_M) + \frac{\partial}{\partial x}(\alpha_M \rho_M u_M) = \dot{m}_H \tag{4.10}$$

The other governing equations remain the same, with the exception of the dissolved gas continuity equation (Equation 3.9), which is now omitted. Figure 4.24 shows the slug profile generated by the test case. As can be seen, it is a heavily slugged case, with a slug body length ranging from 1 to 10 m long. In order to get as much hydrate formation within the slug region, the heat released from the pipe to the environment was set to be rapid, so the system temperature reached the hydrate equilibrium temperature as early as possible (Figure 4.25). This is done by setting a high value to the total heat transfer coefficient, U_k in Equation (3.32) for all phases.

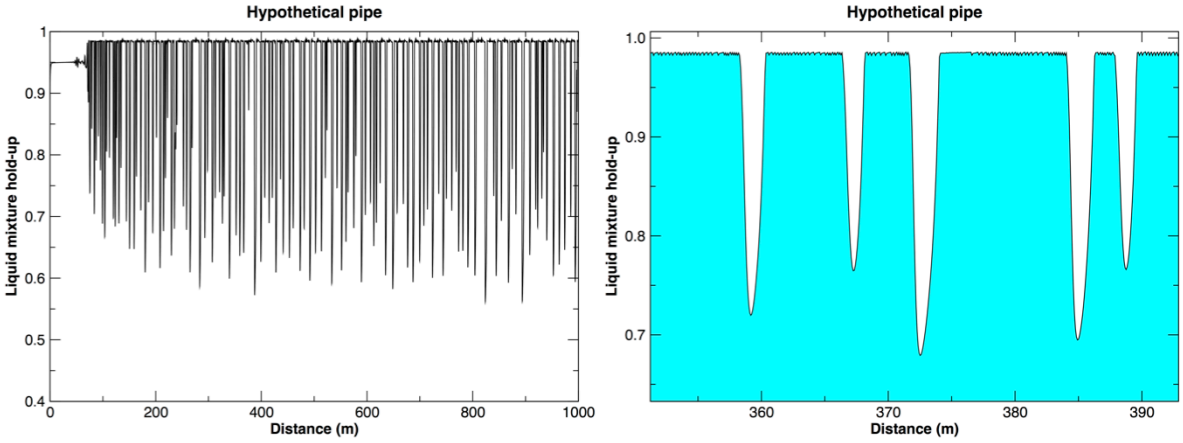


Figure 4.24: Slug profile generated by the current model for the test case.

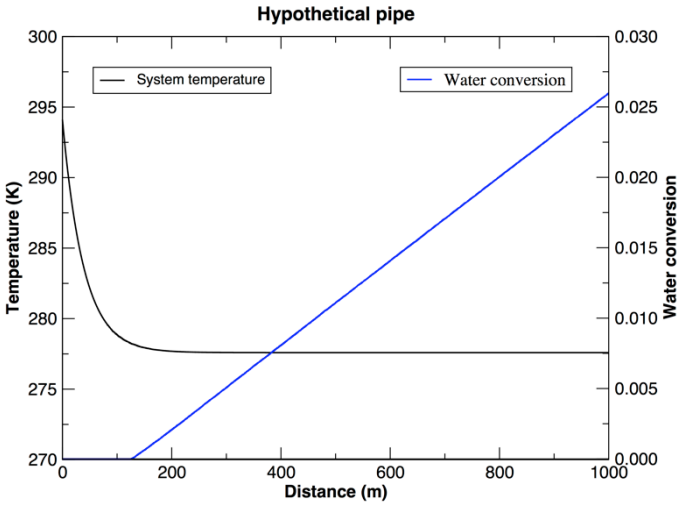
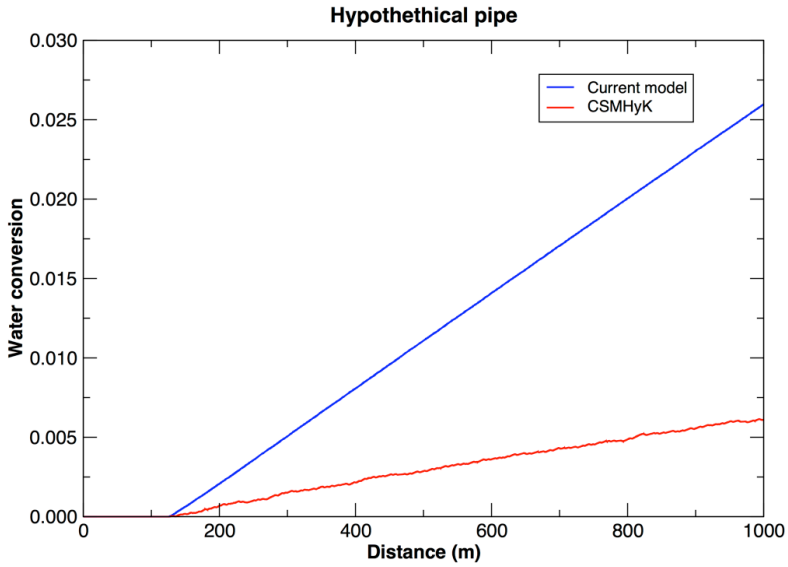


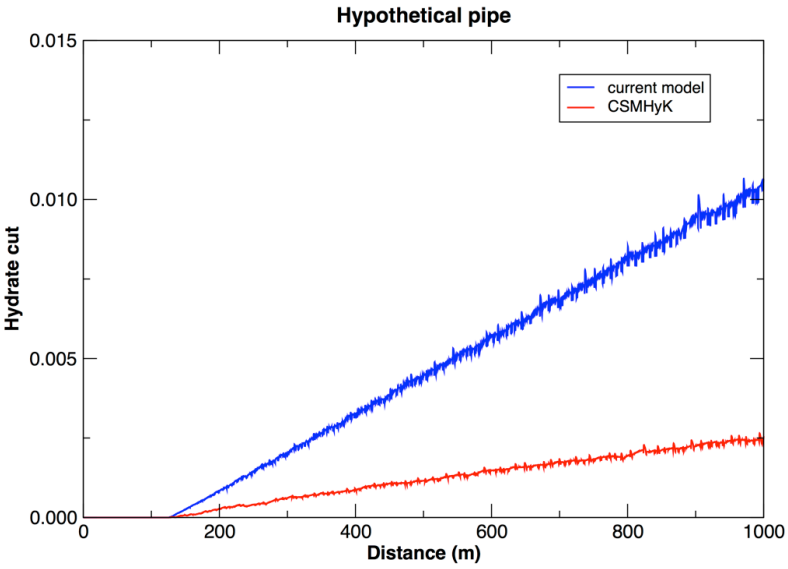
Figure 4.25: The temperature profile and the water conversion of the hypothetical pipe.

Figure 4.26 shows the results of the hydrate formation prediction by the current model and CSMHyK model. At this time the author likes to stress again that the CSMHyK results are obtained through implementing the CSMHyK method into the TRIOMPH code rather than through the actual CSMHyK program.

As shown, the current model predicted five times as much water conversion, and four times as much hydrate cut, c_H within the slug flow regime, compared to CSMHyK model. This is because, in the slug body region, no free gas is present, hence from Equation (4.9), $\dot{m}_H$ becomes zero. However, in the current model, guest molecules exist in the oil phase in the form of dissolved gas. In the slug body region, the rate of gas dissolution $\dot{m}_{DG}$ (Equation 3.5) is zero, but not the rate of hydrate formation $\dot{m}_H$, hence hydrate formation continue be predicted in this region.



(a)



(b)

Figure 4.26: Hydrate formation in slug flow regime between the current model and the method used in CSMHyK (a) water conversion over the pipe length (b) hydrate cut over the pipe length.

If the trends in Figure 4.26 were to be extrapolated to 20km long pipe, the current model would predict more than 50% water conversion compared to about 10% through the CSMHyK model. This will affect the prediction on the location of a hydrate plug. Plugging occurs when the hydrate slurry viscosity (Equation 3.47) increases drastically causing a large pressure drop in the pipe. From Equation (3.47), we know that the viscosity of hydrate slurry strongly depends on the hydrate cut. Therefore, based on this observation, CSMHyK would over predict (too far downstream) the location of a (possible) hydrate plug in slug flow cases.

5 CONCLUSIONS AND RECOMMENDATIONS

5.1 Conclusions

A one-dimensional two-fluid model that is able to simulate hydrate formation in pipelines has been presented. A single energy equation, and two additional continuity equations for the dissolved gas and the hydrate phase, along with the appropriate closure relations to account for the agglomeration of hydrate globules has been formulated. The new flow equations were implemented into the existing three-phase TRIOMPH code developed by Bonizzi and Issa (2003b) and Barbeau (2008). The conclusions drawn from the present thesis are discussed below.

The hydrate kinetics routine, which comprises of two modules; the dissolved gas module and the hydrate formation module, has been presented. The dissolved gas module solves the dissolved gas continuity equation, while the hydrate formation module solves the hydrate continuity equation, and estimates the agglomeration of hydrate particles and the subsequent slurry viscosity. The agglomeration of hydrate globules was used to calculate the effective viscosity of the hydrate liquid carrier,

which in turn affects the friction factors, and consequently affects the momentum conservation equations.

To attest the correctness of the implementation of both the energy equation and the hydrate kinetics routine into TRIOMPH, simple parametric analyses were performed. The analyses have shown to agree with the theory, hence the correct implementation of both energy equation and the hydrate kinetics routine was verified. To validate the new model, the TRIOMPH code with the implementation of both the energy equation and the hydrate kinetics routine was applied to two available flow loop experiments, the ExxonMobil flow loop and the University of Tulsa flow loop.

On the simulation of the ExxonMobil flow loop, the formation rate constants regressed from Vysniauskas and Bishnoi (1983) were required to be reduced to account for the added heat and mass resistance during hydrate formation. The simulation results were fitted to the experimental data to obtain the best-fitted rate constant for each experiment. It was found that the fitted rate constant varied depending on how the water-oil interfacial surface area was calculated. This variation was reduced by assuming full water-in-oil dispersions, with a uniform $80\,\mu m$ droplet diameter, to represent the experiment's flow condition. This is because, the current model was not able to predict the increased dispersions from mixing caused by the pump and elbows in the loop that are not modelled. Based on this assumption, on average, the best-fitted rate constant in the ExxonMobil flow loop simulation was found to be 0.00002. To conclude, a better droplet size

estimation may result in only one fitted rate constant, that applies to various flow conditions, to account for the heat and mass transfer resistance. On the other hand, a better modelling of the physics of the hydrate formation that accounts for the heat and mass transfer resistance may eliminate the need for the fitted rate constant altogether.

All the simulations of the University of Tulsa flow loop were performed using the same assumptions used in the previous ExxonMobil flow loop. The average fitted rate constant found in the ExxonMobil flow loop was used, together with the assumption of full dispersion water-in-oil. It was found that the simulations compare relatively well with the experiments for three different oils. This suggests that the average fitted rate constant found in the ExxonMobil flow loop is transferable from one system to another.

The capability of the current model to predict hydrate formation in a dynamically changing transient flow such as the slug flow regime has been presented. It was shown that the current model predicted five times as much hydrate formation, compared to the method used in CSMHyK for a heavily slugged flow. This is because, in the current model, hydrate formation mechanism occurs in two steps: first, the mass transfer of gas from the free gas phase to the oil (solved by the dissolved gas module), and second, the mass transfer of the dissolved gas (as the hydrate former) to the water (solved by the hydrate formation module). In this manner, hydrates can form in the slug body region, uninterrupted by the absence of

the free gas phase. This proved that the current model is more versatile, capable to predict hydrate formation in both slug and non-slug cases.

5.2 Recommendations for Future Works

One of the benefits from the present research is that it sets the foundation towards a better hydrate plugging model. Some recommendations for future work are discussed in the following sections:

5.2.1 Surface area for hydrate formation

More accurate predictions of the surface area for hydrate formation can be implemented in the current model. The mean water droplet size can be found through the correlations developed by Boxall (2009). He identified two separate regions (the inertial and viscous sub-ranges) in the turbulent flow that affect the mean water droplet size in oil (Figure 5.1). The correlations were developed based on autoclaves and flow loops experimental data, involving different crude oils (Figure 5.2). The mean droplet diameter for each sub-range can be calculated from:

$$\bar{d} = \begin{cases} 0.063 D We^{-3/5} & \text{for inertial sub} - \text{range} \\ 0.016 D Re^{1/2} We^{-1} & \text{for viscous sub} - \text{range} \end{cases} \tag{5.1}$$

in which the transition from inertial to viscous sub-range can be modelled by:

$$We < 0.0674 Re^{5/4} \tag{5.2}$$

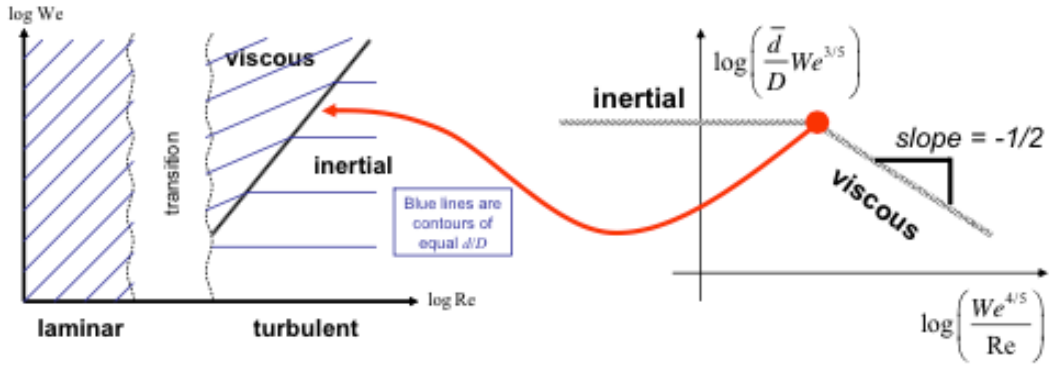


Figure 5.1: Phase diagram of different flow regimes shown as two intersecting lines that represent the planes of the inertial and viscous sub-ranges Boxall (2009).

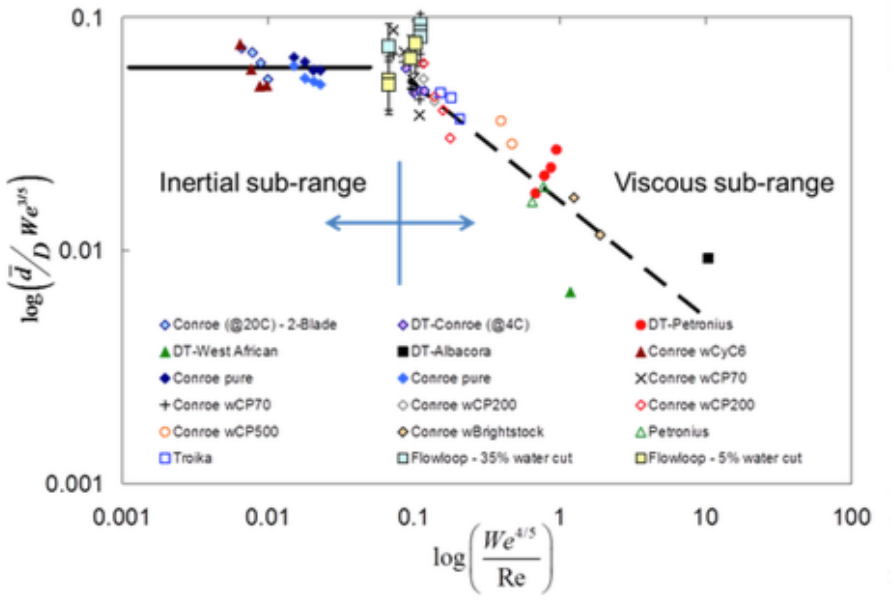


Figure 5.2: Universal curve to estimate the mean droplet size in water-in-oil dispersions system (Boxall, 2009)

5.2.2 Hydrate transport model

A better hydrate formation model with more physical representation of the hydrate formation can be implemented in the new modelling framework. The heat and mass transfer resistance during hydrate formation can be added into the present hydrate kinetics routine. In this manner, the fitted rate constant used in the present thesis can be eliminated.

The heat transfer resistance during hydrate formation is important in a larger diameter system. This is because, the exothermic heat released during hydrate formation is often higher than the rate of heat dissipation from the system to the environment, which results in a rise in the temperature of the system. In such case, the heat transfer resistance must be included in the model. Davies (2009) found that the mass transfer of guest molecules across the hydrate shell is the most limiting factor during hydrate growth. Hence, the hydrate growth (based on the shrinking core model) can be modelled as the mass transport of hydrate former across the hydrate shell (hydrate transport model) (Zerpa, 2013):

$$\dot{m}_{G-H} = \frac{D_{G-H} A_s}{\delta \left(\frac{r_w}{r_p}\right)} \left(C_{bulk} - C_{eq}\right) \tag{5.3}$$

where D_{G-H} is the diffusivity of gas through the hydrate shell, assumed to be $1\times10^{-16}\ m^2/s$ (Kuhs et al., 2006), A_s is the surface of hydrate particle, δ is the thickness of the hydrate shell, r_w is the water core radius, r_p is the particle radius, C_{bulk} is the concentration of gas in the liquid bulk and C_{eq} is the gas concentration in the water phase in the presence of hydrate.

References

ANDERSSON, V. & GUDMUNDSSON, J. S. 2000. Flow properties of hydrate-in-water slurries. *Gas Hydrates: Challenges for the Future,* 912**,** 322-329.

ANDREUSSI, P., BENDIKSEN, K. H. & NYDAL, O. J. 1993. Void Distribution in Slug Flow. *International Journal of Multiphase Flow,* 19**,** 817-828.

BAI, Y. & BAI, Q. 2005. *Subsea Pipelines and Risers* Elsevier Ltd.

BAKER, O. 1954. Simultaneous flow of oil and gas. *Oil and Gas Journal,* 53**,** 185-195.

BARBEAU, S. 2008. *Improved models for transient one-dimensional simulations of multiphase slug flows.* Ph.D, Imperial College London.

BARNEA, D. & TAITEL, Y. 1996. Stratified three phase flow in pipes - Stability and transition. *Chemical Engineering Communications,* 141**,** 443-460.

BONIZZI, M. 2003. *Transient One-Dimensional Modelling of Multiphase Slug Flows.* Ph.D, Imperial College London.

BONIZZI, M. & ISSA, R. I. 2003a. A model for simulating gas bubble entrainment in two-phase horizontal slug flow. *International Journal of Multiphase Flow,* 29**,** 1685-1717.

BONIZZI, M. & ISSA, R. I. 2003b. On the simulation of three-phase slug flow in nearly horizontal pipes using the multi-fluid model. *International Journal of Multiphase Flow,* 29**,** 1719-1747.

BOXALL, J., DAVIES, S. R., KOH, C. & SLOAN, E. D. 2009. Predicting When and Where Hydrate Plugs Form in Oil-Dominated Flowlines. *SPE Production & Operations*.

BOXALL, J. A. 2009. *Hydrate Plug Formation from <50% Water Content Water-in-Oil Emulsions.* Ph.D, Colorado School of Mines.

BRAUNER, N. & ULLMANN, A. 2004. Modelling of gas entrainment from Taylor bubbles. Part A: Slug flow. *International Journal of Multiphase Flow,* 30**,** 239-272.

BRINKMAN, H. C. 1952. The Viscosity of Concentrated Suspensions and Solutions. *The Journal of Chemical Physics,* 20**,** 571-571.

BYRON BIRD, R., STEWART, W. E. & LIGHTFOOT, E. N. 2002. *Transport Phenomena*, John Wiley and Sons, Inc.

CAMARGO, R., PALERMO, T., SINQUIN, A. & GLENAT, P. 2000. Rheological characterization of hydrate suspensions in oil dominated systems. *Gas Hydrates: Challenges for the Future,* 912**,** 906-916.

CARROLL, J. J. 2008. *Natural Gas Hydrates. A Guide for Engineerss*, Gulf Professional Publishing

COLOMBEL, E., GATEAU, P., BARRÉ, L., GRUY, F. & PALERMO, T. 2009. Discussion sur les mécanismes d'agglomération entre particules d'hydrate dans les émulsions eau dans huile. *Oil & Gas Science and Technology - Rev. IFP,* 64**,** 629-636.

DAVIES, S., BOXALL, J., KOH, C., SLOAN, E., HEMMINGSEN, P., KINNARI, K. & XU, Z. 2009a. Predicting Hydrate-Plug Formation in a Subsea Tieback. *Spe Production & Operations,* 24**,** 573-578.

DAVIES, S. R. 2009. *The Role of Transport Resistances in the Formation and Remediation of Hydrate Plugs.* Ph.D, Colorado School of Mines.

DAVIES, S. R., BOXALL, J., DIEKER, L. E., SUM, A., KOH, C. & SLOAN, E. D. 2009b. Improved Predictions of Hydrate Plug Formation in Oil-Dominated Flowlines. *Offshore Technology Conference.* Houston, Texas.

DAVIES, S. R., BOXALL, J., KOH, C., SLOAN, E. D., HEMMINGSEN, P. & KINNARI, K. 2008. Predicting Hydrate-Plug Formation in a Subsea Tieback. *SPE Annual Technical Conference and Exhibition.* Denver.

DECARRE, S. & FABRE, J. 1997. Phase inversion behavior for liquid-liquid dispersions. *Revue De L Institut Francais Du Petrole,* 52**,** 415-424.

DELLECASE, E., GERACI, G., BARRIOS, L., ESTANGA, D., DOMINGUES, R. & VOLK, M. Hydrate plugging or slurry flow: Effect of key variables. Proc. 6th Intl. Conf. on Gas Hydrates, 6-10 July 2008 2008 Vancouver, Canada.

DHARMAWARDHANA, P. B., PARRISH, W. R. & SLOAN, E. D. 1980. Experimental Thermodynamic Parameters for the Prediction of Natural-Gas Hydrate Dissociation Conditions. *Industrial & Engineering Chemistry Fundamentals,* 19**,** 410-414.

DI SALVO, F. R. 2014. *Mechanistic Models to simulate Slug Flow in Horizontal and Vertical Pipes.* PhD, Imperial College London.

EMAMZADEH, M. & ISSA, R. I. 2013a. A Model for Predicting the Transition Between Stratified and Annular Flow in Horizontal Pipes. 25**,** 79-100.

EMAMZADEH, M. & ISSA, R. I. 2013b. One-Dimensional Model for Numerical Simulation of Annular Flow in Horizontal and Vertical Pipes. 25**,** 25-56.

ENGLEZOS, P., KALOGERAKIS, N., DHOLABHAI, P. D. & BISHNOI, P. R. 1987a. Kinetics of Formation of Methane and Ethane Gas Hydrates. *Chemical Engineering Science,* 42**,** 2647-2658.

ENGLEZOS, P., KALOGERAKIS, N., DHOLABHAI, P. D. & BISHNOI, P. R. 1987b. Kinetics of Gas Hydrate Formation from Mixtures of Methane and Ethane. *Chemical Engineering Science,* 42**,** 2659-2666.

FELIZOLA, H. & SHOHAM, O. 1995. A Unified Model for Slug Flow in Upward Inclined Pipes. *Journal of Energy Resources Technology-Transactions of the Asme,* 117**,** 7-12.

GAILLARD, C., MONFORT, J. P. & PEYTAVY, J. L. 1999. Investigation of Methane Hydrate Formation in a Recirculating Flow Loop: Modeling of the Kinetics and Tests of Efficiency of Chemical Additives on Hydrate Inhibition. *Oil & Gas Science and Technology,* 54**,** 365-374.

GAINVILLE, M. & SINQUIN, A. Hydrate Slurry Characterisation for Laminar and Turbulent Flows in Pipelines. Proceedings of the 7th International Conference on Gas Hydrates (ICGH 2011), 17-21 July 2011 2011 Edinburgh, Scotland.

GREGORY, G. A., NICHOLSON, M. K. & AZIZ, K. 1978. Correlation of the liquid volume fraction in the slug for horizontal gas-liquid slug flow. *International Journal of Multiphase Flow,* 4**,** 33-39.

HAND, N. P. 1991. *Gas-Liquid co-current flow in a horizontal pipe.* PhD, Queen's University, Belfast.

HERRI, J. M., PIC, J. S., GRUY, F. & COURNIL, M. 1999. Methane hydrate crystallization mechanism from in-situ particle sizing. *Aiche Journal,* 45**,** 590-602.

HIBIKI, T. & ISHII, M. 2003a. One-dimensional drift-flux model and constitutive equations for relative motion between phases in various two-phase flow regimes. *International Journal of Heat and Mass Transfer,* 46**,** 4935-4948.

HIBIKI, T. & ISHII, M. 2003b. One-dimensional drift-flux model for two-phase flow in a large diameter pipe. *International Journal of Heat and Mass Transfer,* 46**,** 1773-1790.

HOLDER, G. D. & HAND, J. H. 1982. Multiple-Phase Equilibria in Hydrates from Methane, Ethane, Propane and Water Mixtures. *Aiche Journal,* 28**,** 440-447.

HOLDER, G. D. & JOHN, V. T. 1983. Thermodynamics of Multicomponent Hydrate Forming Mixtures. *Fluid Phase Equilibria,* 14**,** 353-361.

ISHII, M. 1978. One-dimensional drift flux model and constitute equations for relative motion between phases in various two-phase flow regimes. Argonne, Illinois: Argone National Laboratory.

ISHII, M. & HIBIKI, T. 2006. *Thermo-Fluid Dynamics of Two-Phase Flow,* New York, Springer Science.

ISSA, R. & ABRISHAMI, Y. 1986. Computer Modelling of Slugging Flow. *Technical report.* Mechanical Engineering Department: Imperial College London.

ISSA, R., BONIZZI, M. & BARBEAU, S. 2006. Improved closure models for gas entrainment and interfacial shear for slug flow modelling in horizontal pipes. *International Journal of Multiphase Flow,* 32**,** 1287-1293.

ISSA, R. I. & KEMPF, M. H. W. 2003. Simulation of slug flow in horizontal and nearly horizontal pipes with the two-fluid model. *International Journal of Multiphase Flow,* 29**,** 69-95.

ISSA, R. I. & WOODBURN, P. J. 1998. Numerical prediction of instabilities and slug formation in horizontal two-phase flows.

KEMPF, M. H. W. & ISSA, R. I. 2000. A model for gas bubble entrainment in slug flow. Mechanical Engineering Department: Imperial College London.

KHOR, S. H., MENDESTATSIS, M. A. & HEWITT, G. F. 1997. One-dimensional modelling of phase holdups in three-phase stratified flow. *International Journal of Multiphase Flow,* 23**,** 885-897.

KUHS, W. F., STAYKOVA, D. K. & SALAMATIN, A. N. 2006. Formation of methane hydrate from polydisperse ice powders. *Journal of Physical Chemistry B,* 110**,** 13283-13295.

LEE, S. Y. & HOLDER, G. D. 2001. Methane hydrates potential as a future energy source. *Fuel Processing Technology,* 71**,** 181-186.

LO, S. 2011. CFD modelling of hydrate formation in oil-dominated flows. *Offshore Technology Conference.* Houston, Texas.

MASLIN, M., OWEN, M., BETTS, R., DAY, S., DUNKLEY JONES, T. & RIDGWELL, A. 2010. Gas hydrates: past and future geohazard? *Philos Trans A Math Phys Eng Sci,* 368**,** 2369-93.

MATTHEWS, P. N., NOTZ, P. K., WIDENER, M. W. & PRUKOP, G. 2000. Flow loop experiments determine hydrate plugging tendencies in the field. *Gas Hydrates: Challenges for the Future,* 912**,** 330-338.

MILLS, P. 1985. Non-Newtonian Behavior of Flocculated Suspensions. *Journal De Physique Lettres,* 46**,** L301-L309.

ODOZI, U. A. 2000. *Three-phase gas/liquid/liquid slug flow.* Ph.D, Imperial College, London.

PALERMO, T., FIDEL-DUFOUR, A., MAUREL, P., PEYTAVY, J. L. & HURTEVENT, C. 2005. Model of Hydrates Agglomeration – Application to Hydrates Formation in an Acidic Crude Oil. *12th International Conference on Multiphase Production Technology.* Barcelona, Spain: BHR Group.

PAN, L. 1996. *High pressure three-phase (gas/liquid/liquid) flow.* Ph.D, Imperial College London.

PAUCHARD, V., DARBOURET, M., PALERMO, T. & PEYTAVY, J. L. 2007. Gas Hydrate Slurry Flow in a Black Oil. Prediction of Gas Hydrate Particles Agglomeration and Linear Pressure Drop. *13th International Conference on Multiphase Production Technology.* Edinburgh, UK: BHR Group.

RIPPINER, J. M. 1998. *Transient Slug Flow Modelling in Horizontal and Near Horizontal Pipelines.* Master, Imperial College, London.

SINQUIN, A., PALERMO, I. & PEYSSON, Y. 2004. Rheological and flow properties of gas hydrate suspensions. *Oil & Gas Science and Technology-Revue D Ifp Energies Nouvelles,* 59**,** 41-57.

SKOVBORG, P. & RASMUSSEN, P. 1994. A Mass-Transport Limited Model for the Growth of Methane and Ethane Gas Hydrates. *Chemical Engineering Science,* 49**,** 1131-1143.

SLOAN, E. D. 2003. Fundamental principles and applications of natural gas hydrates. *Nature,* 426**,** 353-359.

SLOAN, E. D. & KOH, C. A. 2007. *Clathrate Hydrates of Natural Gases*.

TAITEL, Y., BARNEA, D. & BRILL, J. P. 1995. Stratified 3-Phase Flow in Pipes. *International Journal of Multiphase Flow,* 21**,** 53-60.

TAITEL, Y. & DUKLER, A. E. 1976. Model for Predicting Flow Regime Transitions in Horizontal and near Horizontal Gas-Liquid Flow. *Aiche Journal,* 22**,** 47-55.

TOMIYAMA, A., KATAOKA, I., FUKUDA, T. & SAKAGUCHI, T. 1995. Drag coefficient of bubbles (2nd report, drag coefficient for a swarm of bubbles and its applicability to transient flow). *Transactions of the Japan Society of Mechanical Engineers.*

TURNER, D., BOXALL, J., YANG, D., KLEEHAMER, C., KOH, C., MILLER, K. & SLOAN, E. D. Development of a Hydrate Kinetic Model and its Incorporation into the OLGA2000 Transient Multi-Phase Flow Simulator. Proceedings of the Fifth International Conference on Gas Hydrates (ICGH5), 2005 Trondheim, Norway.

TURNER, D. J. 2006. *Clathrate Hydrate Formation in Water-in-Oil Dispersions.* Ph.D, Colorado School of Mines.

TURNER, D. J., MILLER, K. T. & SLOAN, E. D. 2009. Methane hydrate formation and an inward growing shell model in water-in-oil dispersions. *Chemical Engineering Science,* 64**,** 3996-4004.

VERSTEEG, H. K. & MALALASEKERA, W. 1995. *An Introduction to Computational Fluid Dynamics: The Finite Volume Method*, Longman Scientific & Technical.

VYSNIAUSKAS, A. & BISHNOI, P. R. 1983. A Kinetic-Study of Methane Hydrate Formation. *Chemical Engineering Science,* 38**,** 1061-1072.

VYSNIAUSKAS, A. & BISHNOI, P. R. 1985. Kinetics of Ethane Hydrate Formation. *Chemical Engineering Science,* 40**,** 299-303.

WANG, W., FAN, S., LIANG, D. & LI, Y. 2010. A model for estimating flow assurance of hydrate slurry in pipelines. *Journal of Natural Gas Chemistry,* 19**,** 380-384.

ZERPA, L., E. 2013. *A Practical Model to Predict Gas Hydrate Formation, Dissociation And Transportability in Oil and Gas Flowines.* Ph.D, Colorado Scholl of Mines.

ZERPA, L., E, KOH, C. A., SLOAN, E. D. & SUM, A. K. 2011. Generation of Best Practices in Flow Assurance Using a Transient Hydrate Kinetics Model. *Offshore Technology Conference.* Houston, Texas.

Appendix A: The Derivation of the Liquid Mixture Momentum Equation

The individual water, oil and gas bubble momentum equations are:

$$\frac{\partial}{\partial t}(\alpha_W \rho_W u_W) + \frac{\partial}{\partial x}(\alpha_W \rho_W u_W^2) = -\alpha_W \frac{\partial P}{\partial x} + RHS_W \tag{A.1}$$

$$\frac{\partial}{\partial t}(\alpha_O \rho_O u_O) + \frac{\partial}{\partial x}(\alpha_O \rho_O u_O^2) = -\alpha_O \frac{\partial P}{\partial x} + RHS_O \tag{A.2}$$

$$\frac{\partial}{\partial t}(\alpha_B \rho_G u_B) + \frac{\partial}{\partial x}(\alpha_B \rho_G u_B^2) = -\alpha_B \frac{\partial P}{\partial x} + RHS_B \tag{A.3}$$

Adding the LHS of Equation (A.1) to Equation (A.3) together:

$$\frac{\partial}{\partial t}(\alpha_W \rho_W u_W + \alpha_O \rho_O u_O + \alpha_B \rho_G u_B) + \frac{\partial}{\partial x}(\alpha_W \rho_W u_W^2 + \alpha_O \rho_O u_O^2 + \alpha_B \rho_G u_B^2) \tag{A.4}$$

The temporal term on Equation (A.4) can be rearranged using Equation (3.12), and Equation (3.13), and multiplying and dividing by the liquid mixture density, Equation (3.20), one can deduce:

$$\frac{\partial}{\partial t}(\alpha_W \rho_W u_W + \alpha_O \rho_O u_O + \alpha_B \rho_G u_B) = \frac{\partial}{\partial t}(\alpha_M \rho_M u_M) \tag{A.5}$$

And the spatial term on Equation (A.4), rearranged using Equation (3.12) and Equation (3.13):

$$\frac{\partial}{\partial x}(\alpha_W \rho_W u_W^2 + \alpha_O \rho_O u_O^2 + \alpha_B \rho_G u_B^2) = \frac{\partial}{\partial x}\{\alpha_M [c_W \rho_W u_W^2 + (1 - c_W - c_B)\rho_O u_O^2]\} \quad \text{(A.6)}$$

The phasic velocity can be substituted by equation (3.23):

$$\begin{aligned} &\frac{\partial}{\partial x}(\alpha_W \rho_W u_W^2 + \alpha_O \rho_O u_O^2) \\ &\qquad = \frac{\partial}{\partial x}\left\{\alpha_M \left[c_W \rho_W \left(u_M + \frac{(1 - c_W - c_B)\rho_O u_s}{\rho_M}\right)^2\right.\right. \\ &\qquad \left.\left. + (1 - c_W)\rho_O \left(u_M - \frac{c_W \rho_W u_s}{\rho_M}\right)^2\right]\right\} \end{aligned} \quad \text{(A.7)}$$

Expanding the two squares in Equation (A.7), and with simplifications:

$$\frac{\partial}{\partial x}(\alpha_W \rho_W u_W^2 + \alpha_O \rho_O u_O^2) = \frac{\partial}{\partial x}\left\{\alpha_M \left[\rho_M u_M^2 + \frac{c_W (1 - c_W - c_B)\rho_W \rho_O u_s^2}{\rho_M}\right]\right\} \quad \text{(A.8)}$$

Substituting Equation (A.5) and Equation (A.8) in the combined momentum equation, one eventually obtains the following form:

$$\begin{aligned} &\frac{\partial}{\partial t}(\alpha_M \rho_M u_M) + \frac{\partial}{\partial x}(\alpha_M \rho_M u_M^2) \\ &\qquad = -\alpha_M \frac{\partial P}{\partial x} - \frac{\partial}{\partial x}\left[\frac{\alpha_M u_s^2 c_W \rho_W (1 - c_W - c_B)\rho_O}{\rho_M}\right] + RHS_W + RHS_O \\ &\qquad + RHS_B \end{aligned} \quad \text{(A.9)}$$

Appendix B: The Derivation of Non-Conservative Energy Equation

The conservative form of the energy equation is:

$$\begin{aligned}&\frac{\partial}{\partial t}\left(\alpha_k\rho_k C_{p_k}T\right)+\frac{\partial}{\partial x}\left(\alpha_k\rho_k C_{p_k}Tu_k\right)\\&\qquad=-\alpha_k\left(\frac{\partial\ln\rho}{\partial\ln T}\right)_P\frac{DP}{Dt}+\alpha_k\rho_k T\frac{DC_{p_k}}{Dt}-\left(\tau_{wk}u_k\right)+Q_k\end{aligned}\tag{B.1}$$

The temporal term on the LHS of Equation (B.1) can be rearranged into:

$$\frac{\partial}{\partial t}\left(\alpha_k\rho_k C_{p_k}T\right)=\left(\alpha_k\rho_k C_{p_k}\right)\frac{\partial T}{\partial t}+T\frac{\partial}{\partial t}\left(\alpha_k\rho_k C_{p_k}\right)\tag{B.2}$$

and the spatial term on the LHS of Equation (B.1) can be rearranged into:

$$\frac{\partial}{\partial x}\left(\alpha_k\rho_k C_{p_k}Tu_k\right)=\left(\alpha_k\rho_k C_{p_k}u_k\right)\frac{\partial T}{\partial x}+T\frac{\partial}{\partial x}\left(\alpha_k\rho_k C_{p_k}u_k\right)\tag{B.3}$$

Therefore,

$$\begin{aligned}&\frac{\partial}{\partial t}\left(\alpha_k\rho_k C_{p_k}T\right)+\frac{\partial}{\partial x}\left(\alpha_k\rho_k C_{p_k}Tu_k\right)\\&\qquad=\left(\alpha_k\rho_k C_{p_k}\right)\frac{\partial T}{\partial t}+\left(\alpha_k\rho_k C_{p_k}u_k\right)\frac{\partial T}{\partial x}\\&\qquad+\underbrace{T\left[\frac{\partial}{\partial t}\left(\alpha_k\rho_k C_{p_k}\right)+\frac{\partial}{\partial x}\left(\alpha_k\rho_k C_{p_k}u_k\right)\right]}_{\otimes}\end{aligned}\tag{B.4}$$

Using the same method, the second term on the RHS of Equation (B.4), marked with (⊗), can be written as:

$$T\left[\frac{\partial}{\partial t}\left(\alpha_k \rho_k C_{p_k}\right) + \frac{\partial}{\partial x}\left(\alpha_k \rho_k C_{p_k} u_k\right)\right] = \underbrace{T\left[\left(\alpha_k \rho_k\right)\frac{\partial C_{p_k}}{\partial t} + \left(\alpha_k \rho_k u_k\right)\frac{\partial C_{p_k}}{\partial x}\right]}_{\dagger} + \underbrace{T\left[C_{p_k}\left(\frac{\partial \alpha_k \rho_k}{\partial t} + \frac{\partial \alpha_k \rho_k u_k}{\partial x}\right)\right]}_{*} \tag{B.5}$$

(†), can be simplified to:

$$T\left[\left(\alpha_k \rho_k\right)\frac{\partial C_{p_k}}{\partial t} + \left(\alpha_k \rho_k u_k\right)\frac{\partial C_{p_k}}{\partial x}\right] = \left(\alpha_k \rho_k T\right)\frac{DC_{p_k}}{Dt} \tag{B.6}$$

which is the same term found on the RHS on Equation (B.1), balanced each other out thus vanish from the equation. (⁎) is also zero by continuity consideration:

$$\frac{\partial \alpha_k \rho_k}{\partial t} + \frac{\partial \alpha_k \rho_k u_k}{\partial x} = 0 \tag{B.7}$$

Therefore, Equation (B.1) can be re-written and becomes:

$$\left(\alpha_k \rho_k C_{p_k}\right)\frac{\partial T}{\partial t} + \left(\alpha_k \rho_k C_{p_k} u_k\right)\frac{\partial T}{\partial x} = -\alpha_k \left(\frac{\partial \ln \rho}{\partial \ln T}\right)_P \frac{DP}{Dt} - \left(\tau_{wk} u_k\right) + Q_k \tag{B.8}$$

Appendix C: Oils Composition

The composition of the two oils used in the ExxonMobil flow loop (Boxall, 2009)

Component		Percentage of weight ($Wt\%$)	
		CONROE OIL	**CONROE OIL + BRIGHTSTOCK**
C1	Methane	0.001	0.000
C2	Ethane	0.002	0.001
C3	Propane	0.029	0.014
iC4	i-Butane	0.042	0.020
nC4	n-Butane	0.121	0.058
iC5	i-Pentane	0.254	0.123
nC5	n-Pentane	0.289	0.140
C6	Hexanes	1.013	0.491
C7	Heptanes	3.492	1.692
C8	Octanes	7.851	3.804
C9	Nonanes	6.768	3.280
C10	Decanes	6.210	3.009
C11	Undecanes	5.253	2.545
C12	Dodecanes	5.566	2.697
C13	Tridecanes	6.909	3.348
C14	Tetradecanes	6.872	3.330
C15	Pentadecanes	6.595	3.196
C16	Hexadecanes	5.526	2.678
C17	Heptadecanes	4.491	2.176
C18	Octadecanes	4.640	2.249
C19	Nonadecanes	3.579	1.743
C20+	Eicosanes plus	24.480	63.400
TOTAL		**100.000**	**100.000**

The composition of the three oils used in the University of Tulsa flow loop (Boxall, 2009)

CARATINGA		BUTTERMILK		CITGO	
Component	**Percentage of weight (Wt%)**	**Component**	**Percentage of weight (Wt%)**	**Component**	**Percentage of weight (Wt%)**
C3	0.130	N2	0.000	C14	0.000
iC4	0.230	CO2	0.009	C15	0.010
nC4	0.700	C1	0.383	C16	0.010
iC5	0.710	C2	0.162	C17	0.050
nC5	0.950	C3	0.703	C18	0.190
C6	2.110	iC4	0.457	C19	0.640
C7	5.579	nC4	1.415	C20	1.720
C8	4.790	iC5	1.365	C21	2.720
C9	5.199	nC5	2.222	C22	7.270
C10-C12	13.130	C6	4.778	C23	12.300
C13-C15	11.440	C7	7.507	C24	14.330
C16-C18	8.830	C8	8.661	C25	13.630
C19-C23	9.690	C9	7.285	C26	11.870
C24-C28	6.840	C10-C12	17.425	C27	11.360
C29-C36	29.678	C13-C15	11.562	C28	8.930
		C16-C18	7.859	C29	5.670
		C19-C23	8.621	C30	9.300
		C24-C28	5.272		
		C29-C36	5.344		
		C37-C45	3.770		
		C46-C57	2.901		
		C58-C80	2.297		
TOTAL	**100.000**	**TOTAL**	**100.000**	**TOTAL**	**100.000**

The composition of City gas used in the University of Tulsa flow loop (Boxall, 2009)

CITY GAS		
Component		**Percentage of weight (Wt%)**
N2	Nitrogen	1.05
CO2	Carbon Dioxide	1.23
C1	Methane	94.84
C2	Ethane	2.35
C3	Propane	0.38
iC4	i-Butane	0.02
nC4	n-Butane	0.06
iC5	i-Pentane	0.01
nC5	n-Pentane	0.02
C6	Hexanes	0.04
	TOTAL	**100**